Universitat Politècnica de Catalunya
Programa de Doctorat en Enginyeria Civil

Departament de Matemàtica Aplicada III

Shape dynamics and lipid hydrodynamics of bilayer membranes: modeling, simulation and experiments

by Mohammad Rahimi

Doctoral Thesis
Advisor: Marino Arroyo

Barcelona, December 2012

Abstract

Shape dynamics and lipid hydrodynamics of bilayer membranes: modeling, simulation and experiments

Mohammad Rahimi

Biological membranes are continuously brought out of equilibrium, as they shape organelles, package and transport cargo, or respond to external actions. The dynamics of lipid membranes are very complex due to the tight interplay between the bilayer architecture, the shape dynamics, the rearrangement of the lipid molecules, and their interactions with adjacent structures. The main goal of the present work is to understand the dynamical shape deformations and reorganizations of lipid bilayers, including lipid hydrodynamics, and the mechanical shaping and stabilization of highly curved membrane structures. Towards this goal, we develop theory, simulation methods, and perform experiments.

We formulate and numerically implement a continuum model of the shape dynamics and lipid hydrodynamics, which describes the bilayer by its mid-surface and by a lipid density field for each monolayer. In this model, the viscoelastic response of bilayers is determined by the stretching and curvature elasticity, and by the inter-monolayer friction and the membrane interfacial shear viscosity. In contrast with previous studies, our numerical approach incorporates the main physics, is fully nonlinear, does not assume predefined shapes, and can access a wide range of time and length scales. We apply our model to describe the dynamics of biologically relevant experimental observations, which are insufficiently understood through simpler models introducing geometrical and physical simplifications. We study the dynamical formation of membrane tubes, followed by pearling instabilities, as a consequence of a localized density asymmetry, the tubular lipid transport between cells, the dynamics of bud absorption, and the very recently observed protrusions out of planar confined bilayers. The passive formation of stable highly curved protrusions in confined bilayers suggests that mechanics plays a role in the morphogenesis and homeostasis of

complex organelles (e.g., endoplasmic reticulum, or mitochondrial cristae), in addition to the widely accepted role of proteins and the regulation of lipid composition.

We also study experimentally and theoretically the shape transformations and membrane reorganizations of model membranes upon the adsorption of cholesterol, a ubiquitous constituent of biomembranes, which regulates their structural and mechanical properties. Our observations offer new insights into the reorganizations of macrophages and the formation of foam cells as a consequence of the cholesterol elevation in vessel walls.

In this thesis, we have payed particular attention to the membrane fluidity and the influence of the membrane viscosity in the bilayer dynamics. The role of the membrane interfacial viscosity is often ignored due to its minor role in the linearize equations about planar states. We challenge this assumption, show theoretically that membrane viscosity plays an important role in the presence of high curvature, and show its effect on the membrane fluctuations of quasi-spherical vesicles and tubular membranes.

Acknowledgments

It is with immense gratitude that I acknowledge the help of my advisor, Professor Marino Arroyo, for the continuous support of my Ph.D study and research, for his patience, motivation, enthusiasm, immense knowledge, and kindness. Honestly, I could not have imagined having a better advisor and mentor for my Ph.D study.

I would like to express my deep gratitude to Professor Howard A. Stone and Dr. Margarita Staykova who hosted me at Princeton University, and supported me in any respect during the completion of this work.

I would like to thank the faculty of Departament de Matemàtica Aplicada III, and School of Civil Engeering (CAMINS). I am truly indebted and thankful for the assistance of administrative staff, in particular Imma Rius, Esther Garcia, Anna Fabregas, Maria Jose, and the technical support of David Ortin.

During this research work, I have collaborated with many colleagues for whom I have sincere regards. I am indebted to all my colleagues in the group of LaCàN at Barcelona, and Complex Fluid Group at Princeton, and all my friends, who supported me during this period. It has been an honor to share many moments with them.

I want to thank the support of the Spanish Government through grant BES-2008-003274, and support of the European Research Council under the European Community's 7th Framework Programme (FP7/2007-2013)/ERC grant agreement nr 240487.

I cannot find words to express my gratitude to my parents, for their love and unconditional support throughout my life.

Contents

List of Figures

List of Tables

Chapter 1

Introduction

Motivation and objectives

Lipid bilayers are quasi-two-dimensional systems made out of two monolayers of lipid molecules held together by the hydrophobic effect. They form most biological containers in cells, and exhibit a wide range of morphologies, from vesicles to tubes, including sheets or complex networks in the endoplasmic reticulum [Shibata et al., 2009]. Biological membranes undergo dynamical shape deformations and reorganizations, crucial for cell functions, such as vesicular or tubular trafficking [Sprong et al., 2001], cell signaling, shaping the cell organelles, or cell death. Such shape transformations are known to be driven by cytoskeleton-induced forces [Revenu et al., 2004], by tuning locally the lipid composition, through interactions with specialized proteins, or upon contraction of the underlying actin cortex [Charras and Paluch, 2008], etc.

These membrane transformations are allowed by the extreme malleability of lipid bilayers, given by their flexibility in bending and their interfacial fluidity. The interfacial fluidity itself is essential to the motion of membrane proteins [Saffman and Delbrück, 1975], the transport of lipids between cells through membrane tubes [Rustom et al., 2004], the membrane thermal fluctuations [Seifert and Langer, 1993], and lateral reorganizations such as the formation of lipid rafts and caveolae [Simons and Vaz, 2004].

The goal of this thesis is to understand the dynamical shape deformations and reorganizations of lipid bilayers, the role of lipid hydrodynamics in such transformations,

and the role of mechanics in shaping and stabilizing highly curved membrane structures. Towards this goal, we develop a continuum theory, numerical and analytical approaches, and perform experiments.

Modeling the dynamics of lipid bilayers

Although a simple elastic surface model such as that described by the Helfrich curvature energy has been able to explain a number of observations of bilayer vesicles [Julicher and Lipowsky, 1993], it has long been recognized that in many situations the mechanical behavior of lipid membranes can only be explained by acknowledging its bilayer architecture [Miao et al., 1994]. Besides curvature elasticity, a general model for the energetics of bilayers [Seifert, 1997] includes the stretching elasticity of each monolayer, which despite the generally small density deviations from equilibrium has a non-negligible effect. Physically, increasing the lipid density in one leaflet leads to a free energy penalty due to the steric interaction between the lipids, while decreasing it exposes the hydrophobic core, resulting again in a free energy cost. In equilibrium, the lipid densities become essentially uniform in each monolayer, and the bilayer continuum model can be simplified in a hierarchy of area difference elasticity models [Seifert, 1997]. However, a local density perturbation takes a finite time to relax, which gives rise to very rich and biologically relevant dynamics as shown by recent biophysical experiments, such as the shape changes due to lipid translocation under the action of flippases [Devaux, 2000], or a local pH disturbance, changing the preferred area per lipid [Khalifat et al., 2008, Fournier et al., 2009], as a few examples of interest.

The over-damped dynamics of bilayers emerge from a balance between the above-mentioned elastic forces and dissipative forces, which include those generated by the in-plane shear viscosity (interfacial viscosity) and by the inter-monolayer friction as they slip past each other. In physiological conditions, in-plane and inter-monolayer shear stresses are purely viscous, with experimentally characterized membrane shear viscosity and inter-monolayer friction coefficients [Dimova et al., 2006]. The membrane

viscosity arises from the friction between the amphiphiles of each monolayer as they shear due to interfacial flows. Putting together the curvature and density elastic forces and the dissipative forces, due to inter-monolayer friction, the interfacial and the surrounding bulk fluid shear viscosity, results in a mathematically complex bilayer dynamical model, which has only been formulated and exercised in simplified settings as reviewed next.

The thermal undulations of bilayers are generally understood in terms of a linearized version of this model, considering infinitesimal shape and density perturbations around a planar or spherical bilayer [Seifert and Langer, 1993, Evans and Yeung, 1994, Seifert, 1997, Sevšek, 2010], and has been used to interpret membrane relaxation dynamics in several studies. However, mathematical formulations of interfacial flows on general geometries show that, in the presence of curvature, the membrane viscosity produces a normal drag force, quadratic in the curvature and linear in the normal velocity [Arroyo and DeSimone, 2009], which is neglected as a consequence of the linearization about planar configuration. Therefore, there is a general tendency in the literature to neglect the membrane shear dissipation, notoriously difficult to treat mathematically, e.g. on the basis of scaling arguments involving the Saffman-Delbrück length scale (the ratio of interfacial shear viscosity to the bulk fluid shear viscosity). In this thesis, we challenge this argument, and show by theory and simulations that membrane viscosity may play an important role in bilayer shape dynamics, in the presence of high curvature or significant shape changes.

Another important application of the bilayer dynamical model, under the strong assumption of fixed shape, is in the hydrodynamics of tether extension [Evans and Yeung, 1994], where the role of inter-monolayer drag for membrane flows around sharp geometries is highlighted. The coupled lipid density and shape dynamics under finite perturbations has been analyzed in [Sens, 2004] for a predefined family of shapes and density distributions.

The complex equations for the dynamics of bilayers can be further simplified under (often too) restricted conditions. In the simplest situation, the bilayer architecture and the membrane dissipative mechanisms can be neglected for giant unilamellar

vesicles, governed by capillarity, curvature elasticity, and bulk dissipation. Around sharp geometries, or for short wavelength thermal undulations, the inter-monolayer friction dominates the dissipation, and membrane and bulk shear viscosities may be neglected. Bilayers can also be studied theoretically with molecular dynamics. However, due to the slow relaxation times of bending modes [Cooke et al., 2005], these methods are severely limited to small time and length scales [Reynwar et al., 2007, Klein and Shinoda, 2008].

In summary, lipid bilayers exhibit subtle mechanics, described by complex continuum equations, which have been judiciously simplified in some situations. In chapter 2, we formulate a dynamical quantitative model for bilayers, observing the intimately coupled lipid hydrodynamics and shape dynamics. We develop a general continuum model accounting for the bilayer nature of the system, its elasticity, and its internal (interfacial and slippage) and external dissipative mechanisms. The model allows us to deal with the membrane finite shape deformation, density deviation, and its interaction with adjacent membranes or substrates. This chapter describes the kinematics of our continuum model, which challenge traditional Lagrangian or Eulerian descriptions [Belytschko et al., 2000], the continuity equation, and the balance of linear momentum. We specialize to axisymmetric systems, allowing us to describe many of the important shapes bilayers adopt. The numerical implementation of the presented model for axisymmetric bilayers, relying on a B-Spline Galerkin method, is presented in chapter 3.

In chapter 4, we apply our model to describe the dynamics of biologically relevant experimental observations. Our model can describe complex lipid hydrodynamics mobilizing the inter-monolayer friction, such as flows around sharp geometries or as a result of localized density asymmetries. The competition between two relaxation mechanisms: flowing lipids or changing the shape, is studied here by considering vesicles with a localized density asymmetry. We also study the nucleation and well-understood extension of membrane tethers, the absorption of a bud by a planar bilayer, and the recently observed tension-driven lipid flows between vesicles and cells connected by tubes, which can be interpreted as a Marangoni effect. These examples

illustrate the diversity and complexity of bilayer dynamics, which make it difficult to provide accurate estimations based on simple arguments. Parts of chapters 2 to 4 have been published as a journal paper in *Physical Review E.* [Rahimi and Arroyo, 2012].

Shaping mechanically confined bilayers

In biomimetic systems, protrusions form out of confined membranes upon straining the membrane-supporting surface [Staykova et al., 2011], or upon incorporating lipids or peptides in supported bilayers [Thid et al., 2007, Domanov and Kinnunen, 2006, Hovis and Boxer, 2001]. Similar processes have been observed in cells, where the membrane bulges into blebs [Charras and Paluch, 2008] or micro-vesicles [Sens and Gov, 2007] upon contraction of the underlying actin cortex, or forms tubular invaginations away from the substratum in shrinking adherent cells [Morris and Homann, 179]. In chapter 5, we provide a unified view of these phenomena, and investigate the rich behavior of confined membranes with experiments, theory and simulations. We show that supported lipid bilayers in the fluid phase form out-of-plane tubular or spherical protrusions, and can be reversibly controlled by the magnitude of the applied strain and the interstitial fluid volume. To understand the experimental observations we develop a theoretical model for the confined bilayer in equilibrium, based on our experimental procedure and the shapes of the protrusions. Using numerical simulations, we check our analytical framework for equilibrium state, and show that compression rate can produce a significant bilayer asymmetry, resulting in the formation of complex morphologies such as pearled tubes. Some of results presented in this chapter have been recently published as a journal paper in *Physical Review Letters* [Staykova, Arroyo, Rahimi, and Stone, 2013].

Shape and composition dynamics by cholesterol adsorption

Cholesterol is a ubiquitous constituent of biomembranes and is crucial for the cell functionality by regulating the membrane fluidity, permeability, elastic stiffnesses (bend-

ing and stretching), etc [Kwik et al., 2003]. The elevation of the cholesterol cellular level results in many medical disorders, which are understood in part as morphological changes and reorganizations of cell membranes [Maxfield and Tabas, 2005]. In chapter 6, we study experimentally and theoretically the dynamical reorganizations, and shape transformations of model membranes upon the adsorption of cholesterol molecules in three different conditions: planar supported lipid bilayer (SLB) patches, continuous SLB, and supported unilamellar giant vesicles (GUVs). When the bilayer is confined, we observe the formation and evolution of tubular and spherical protrusions, and when the bilayer is laterally unconstrained, it spreads with different rates, upon the exposure to a solution of cholesterol of different concentrations. An extended form of our continuum model is presented in chapter 6, which accounts for a nonuniform binary (cholesterol-DOPC) mixture lipid bilayer, and for the adsorption kinetics. With this model, we explain the nonuniform distribution of cholesterol upon fast membrane spreading, mostly due to the substrate friction.

The experimental work of chapter 6 is performed by the author of this thesis during a five month stay at `Princeton University, Department of Mechanical and Aerospace Engineering, Complex Fluids Group`, and funded by Spanish Ministry of Science and Innovation awarded as `EBPI-FPI 2012`, while the experiments presented in chapter 5 were performed by our collaborators at the same center.

Thermal undulations of curved bilayers

Chapter 7 describes the relaxation dynamics and the shape fluctuations of quasi-spherical vesicles and tubular membranes, with a particular attention on the role of the membrane viscosity. We hypothesize and show that the membrane viscosity plays a significant role in the relaxation rates of highly curved membranes, e.g. vesicles, or tubes of radii below the Saffman-Delbrück length scale and suggest new experiments to measure the interfacial viscosity by flickering spectroscopy in membrane tubules. Chapter 8 collects concluding remarks and gives future directions.

Chapter 2

Continuum model

We describe the configuration of the bilayer in terms of its midsurface and two lipid density fields, one for each monolayer, thus forcing at the outset the shape coupling of the two monolayers. The rate of change of the system is given by the rate of change of the midsurface, i.e. its normal velocity, and by the tangential velocity of the lipids of each monolayer, which are in general different, producing inter-monolayer slippage and friction. The lipid densities, and the tangential and normal velocities are coupled through the continuity equation, expressing locally balance of mass. The governing equations are completed with balance of linear momentum, obtained with variational methods, where we ignore inertial forces given the low Reynolds' numbers typical in bilayer mechanics. We pay particular attention to the kinematics, which are necessarily Lagrangian (tracking material particles) in the normal direction to the bilayer, but which cannot be Lagrangian tangentially due to inter-monolayer slippage. We propose an Arbitrarily Lagrangian-Eulerian formulation, very useful in the numerical implementation, and provide detailed and accessible expressions for axisymmetric bilayers.

2.1 Kinematics

We consider the parametric description $\boldsymbol{x}(\xi^1, \xi^2, t)$ of a bilayer midsurface Γ_t. As argued above, a point (ξ^1, ξ^2) in parameter space cannot label a material particle, and

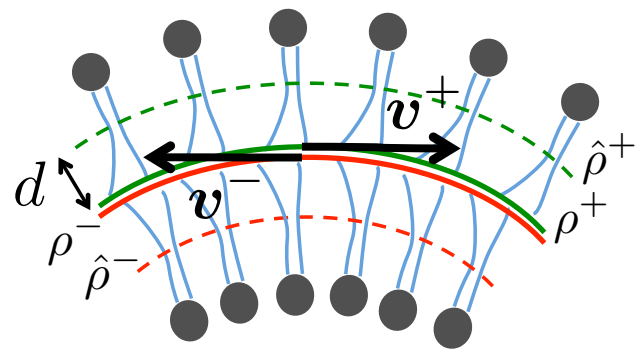

Figure 2.1: (Color online) Description of a bilayer membrane. $\boldsymbol{v}^\pm$ denotes the tangential velocity field of each monolayer on the midsurface. The density field on the neutral surface of each monolayer $\hat{\rho}^\pm$, and the projected density field on the midsurface $\rho^\pm$ are also shown.

the time derivative of this parametrization is not in general the velocity of material particles. We express it as

$$\boldsymbol{x}_{,t} = \boldsymbol{W} = \boldsymbol{w} + v_n \boldsymbol{n}, \tag{2.1}$$

where the normal velocity v_n has mechanical relevance, since it characterizes the rate of shape changes, whereas the tangential field $\boldsymbol{w}$ is the velocity of points with fixed parametric coordinates. We denote by $g_{ab} = \boldsymbol{x}_{,a} \cdot \boldsymbol{x}_{,b}$ the metric tensor, by $\boldsymbol{n}$ the unit normal to the surface, and by $\boldsymbol{k} = -\nabla \boldsymbol{n}$ the second fundamental form, where ∇ denotes the covariant derivative and $(\cdot)_{,a}$ denotes partial differentiation with respect to ξ^a.

To describe the physical tangential velocity of each leaflet, we consider independent vector fields on Γ_t, $\boldsymbol{v}^\pm$, which we define as the velocity of the ends of the tails of the amphiphiles in each leaflet, see Fig. 2.1. This definition is convenient in the formulation of the inter-monolayer friction. For numerical convenience, we allow for general tangential motions of the parameterization, and formulate the mechanics covariantly in this respect. Such a description of motion is often referred to as Arbitrarily Lagrangian-Eulerian (ALE) kinematics, see [Donea and Huerta, 2003, Belytschko et al., 2000] for details. The tangential convective velocity, i.e. the tangential physical velocity relative to points of fixed parameter value (ξ^1, ξ^2), is $\boldsymbol{c}^\pm = \boldsymbol{v}^\pm - \boldsymbol{w}$. If

$\boldsymbol{w} = 0$, we recover an Eulerian description in the tangential direction. Lagrangian descriptions are characterized by zero convective velocity. It is clear that we cannot recover a purely Lagrangian formulation since in general the leaflets slip relative to each other, and therefore $\boldsymbol{w}$ cannot equal $\boldsymbol{v}^+$ and $\boldsymbol{v}^-$ at the same time.

2.2 Continuity equation

Following [Seifert, 1997], we describe each leaflet by a neutral surface representative of its mechanics, i.e. the density of the lipids in this surface $\hat{\rho}^\pm$ is the order parameter that allows us to define the areal elastic energy. The projected densities onto the midsurface of the bilayer $\rho^\pm$, see Fig. 2.1, deviate from $\hat{\rho}^\pm$ according to the following relation

$$\hat{\rho}^\pm = \rho^\pm \left(1 \mp 2dH + O(d^2K)\right). \tag{2.2}$$

where d is the distance between the bilayer midsurface and the neutral surface of the monolayers, usually located close to the polar-apolar interface [Marsh, 2007], H denotes the mean curvature (half the trace of the second fundamental form), and K denotes the Gaussian curvature (the determinant of the second fundamental form). A convenient approximation for small deviations from a reference density of lipids ρ_0, is

$$\hat{\rho}^\pm \approx \rho^\pm \mp 2\rho_0 dH. \tag{2.3}$$

Since the rate-of-change of local area for a time-evolving material interface is given by div $\boldsymbol{v}^\pm - 2v_nH$ [Arroyo and DeSimone, 2009], the conservation of mass for each leaflet takes the form

$$\frac{d\rho^\pm}{dt} + \rho^\pm(\text{div } \boldsymbol{v}^\pm - 2v_nH) = 0, \tag{2.4}$$

where d/dt denotes the material time derivative. In practice, we are interested in time derivatives for a fixed value of (ξ_1, ξ_2). From the chain rule we have [Donea and Huerta, 2003]

$$\rho^\pm_{,t} + \boldsymbol{c}^\pm \cdot \nabla\rho^\pm + \rho^\pm(\text{div } \boldsymbol{v}^\pm - 2v_nH) = 0, \tag{2.5}$$

where we stress that by $\rho^{\pm}_{,t}$ we denote a time derivative for a fixed value of the parameters (ξ_1, ξ_2).

2.3 Free energy

2.3.1 Elastic energy

Deviations from the equilibrium density ρ_0 result in excess elastic energy. Additionally, each leaflet stores elastic energy when curved, for which we follow the classic Helfrich functional ignoring the Gaussian curvature term for simplicity. Consequently the total elastic energy can be written as [Seifert, 1997]

$$\Pi[\boldsymbol{x}, \rho^{\pm}] = \int_\Gamma \frac{K_s}{2}\left(\phi^{+2} + \phi^{-2}\right) dS + \int_\Gamma \frac{\kappa}{2}(2H - C_0)^2 dS + \int_\Gamma f_0 dS,$$

where K_s is the elastic stretching modulus of each monolayer, κ is the bending modulus, C_0 is the spontaneous curvature, $\phi^{\pm} = \hat{\rho}^{\pm}/\rho_0 - 1$ are the reduced density deviations, and f_0 is the surface energy, which is negligible for a highly curved and stretched membrane, compared to the other terms. We rewrite the total elastic energy by substituting Eq. (2.3)

$$\Pi[\boldsymbol{x}, \rho^{\pm}] = \int_\Gamma \frac{K_s}{2}\left(\frac{\rho^{\pm}}{\rho_0} - 1 \mp 2dH\right)^2 dS + \int_\Gamma \frac{\kappa}{2}(2H - C_0)^2.$$

Here and in subsequent expressions we imply a summation of the "+" and "−" contributions. The interested reader can find in Appendix A.1 the expression of the elastic surface stress tensor derived from this Hamiltonian.

We compute now the rate of change of the elastic energy functional, required to derive the governing equations. The resulting expression should be independent of the parametrization of the midsurface, and hence, should depend on $\boldsymbol{x}_{,t}$ through v_n alone. In fact the reparameterization invariance of the Helfrich energy can be easily checked analytically using the expressions in appendix A.2 for the general variations

of the element of area and the mean curvature and the divergence theorem on the surface. By using the continuity equation, we express this functional in terms of the velocities v_n and $\boldsymbol{v}^{\pm}$, instead of v_n and $\rho^{\pm}_{,t}$. For convenience, we consider in this derivation an Eulerian gauge, for which the rate of change of the area element is $-2v_nH\ dS$, and the rate of change of the mean curvature follows the classical expression $2H_{,t} = \Delta v_n + v_n(4H^2 - 2K)$. Using these two expressions, Eq. (2.5) with $\boldsymbol{c}^{\pm} = \boldsymbol{v}^{\pm}$, and rearranging terms, we find $\dot{\Pi} = \dot{\Pi}_{\kappa} + \dot{\Pi}_{K_s}$ with

$$\dot{\Pi}_{\kappa}[v_n] = \kappa \int_{\Gamma} (2H - C_0) \Big\{ \Delta v_n + \left(2H^2 - 2K + HC_0\right) v_n \Big\} dS, \tag{2.6}$$

and

$$\begin{aligned} \dot{\Pi}_{K_s}[v_n, \boldsymbol{v}^{\pm}] = K_s \int_{\Gamma} \left(\frac{\rho^{\pm}}{\rho_0} - 1 \mp 2dH \right) \Big\{ - \mathrm{d}iv \left(\frac{\rho^{\pm}}{\rho_0} \boldsymbol{v}^{\pm} \right) \\ + v_n H \left(\frac{\rho^{\pm}}{\rho_0} + 1 \right) \mp d \left[\Delta v_n + 2v_n(H^2 - K) \right] \Big\} \, dS. \end{aligned} \tag{2.7}$$

where the parametric dependence on $\boldsymbol{x}$ and $\rho^{\pm}$ is omitted. Interestingly, the rate of change of the stretching elastic energy depends on the tangential rearrangements of the lipids, which alter the lipid density but leave the shape unchanged.

Very often in modeling of lipid bilayers, we consider an open surface to simulate an infinite membrane (for instance in modeling of tether extraction or the fusion of a buds). The surface tension $\boldsymbol{\sigma}_0$, applied on the boundary, provides the following external power to the system

$$\dot{\Pi}_{\sigma} = \int_{\gamma_0} \boldsymbol{\sigma}_0^{\pm} \cdot \boldsymbol{v}_0^{\pm} \, d\gamma_0. \tag{2.8}$$

where by $d\gamma_0$ we denote the arc length element of the membrane boundary.

2.3.2 Adhesion and Osmotic potentials

When membranes interact with substrates or sub-cellular structures, they experience attractive and/or repulsive forces. We express the free energy associated to this interaction as an adhesion potential $U(t)$, which is a function of the separation distance t. Thus, the adhesion energy can be expressed as

$$\Pi_{\mathrm{Adh}} = \int_\Gamma U(t) dS.$$

and its rate of change as

$$\dot{\Pi}_{\mathrm{Adh}}[v_n, \boldsymbol{v}^\pm] = \int_\Gamma \left\{ U'(t)\dot{t} + U(t) \left[\mathrm{div}(\boldsymbol{v}^+ + \boldsymbol{v}^-)/2 + v_n H \right] \right\} dS.$$

To consider osmotic effects, we assume that the bilayer separates two osmotic media, e.g. a closed vesicle of volume V enclosing N osmolite molecules. The bilayer is semipermeable, and allows water but not the osmolites to permeate [Olbrich et al., 2000]. Introducing the osmolarity of the enclosed solution at a reference volume $M_0 = N/V_0$, and the corresponding volume $v = V/V_0$, we express the osmotic pressure difference across the bilayer as $\Delta p^{osm} = p^{osm}_{int} - p^{osm}_{out} = \bar{R}T\,(M_0/v - M_{out})$, where R is the gas constant, T the thermodynamical temperature, and M_{out} the osmolarity of the ambient solution, which we view as a control parameter. We can define a potential for the osmotic pressure by

$$\Pi_{osm}(V) = RTV_0\,(M_{out}v - M_0 \ln v)\,. \tag{2.9}$$

The rate of change of osmotic free energy is then

$$\dot{\Pi}_{osm}(V) = RT \left(M_{out} - \frac{N}{V} \right) \dot{V}, \tag{2.10}$$

where the rate of change of volume follows from $\dot{V} = \int_\Gamma v_n \, dS$.

2.4 Dissipation

2.4.1 Internal dissipation

The internal dissipative mechanisms of the bilayer include the monolayer surface viscosity and the friction between two monolayers. We consider each monolayer as a Newtonian interfacial fluid [Scriven, 1960], which can only support a tangential viscous stress

$$\boldsymbol{\sigma}_{\parallel}^{\mathrm{visc},\pm} = 2\mu \boldsymbol{d}^{\pm} + \lambda(tr\ \boldsymbol{d}^{\pm})\boldsymbol{g}, \tag{2.11}$$

where μ and λ are the monolayer shear and dilatational viscosities, see [Dimova et al., 2006] for measured coefficients), and the rate-of-deformation tensor $\boldsymbol{d}$ includes a contribution from the normal velocity of the interface in the presence of curvature

$$\boldsymbol{d}^{\pm} = \frac{1}{2}\left[\boldsymbol{\nabla} \boldsymbol{v}^{\pm} + (\boldsymbol{\nabla} \boldsymbol{v}^{\pm})^{T}\right] - v_n \boldsymbol{k}. \tag{2.12}$$

Assuming as usual a linear relation between the inter-monolayer shear traction and the slippage velocity $\boldsymbol{\tau} = b_m(\boldsymbol{v}^{+} - \boldsymbol{v}^{-})$, we can write the internal Rayleigh dissipation potential from which these viscous stresses derive

$$\begin{aligned} W_{\mathrm{mem}}[v_n, \boldsymbol{v}^{\pm}] &= W_{\mu}[v_n, \boldsymbol{v}^{\pm}] + W_{b_m}[\boldsymbol{v}^{\pm}] \\ &= \frac{1}{2}\int_{\Gamma} \left(2\mu \boldsymbol{d} : \boldsymbol{d} + \lambda(\mathrm{tr}\boldsymbol{d})^2\right)^{\pm} dS \\ &\quad + \frac{b_m}{2}\int_{\Gamma} \|\boldsymbol{v}^{+} - \boldsymbol{v}^{-}\|^2\ dS. \end{aligned} \tag{2.13}$$

See [Arroyo and DeSimone, 2009] for a detailed account of the membrane dissipation.

2.4.2 External dissipation

We assume that the velocities of the membrane and of the surrounding fluid coincide, i.e. no slip as conventionally assumed for lipid-water interactions [Stone and Ajdari, 1998]. Thus the bilayer model is coupled to a bulk fluid velocity field that possibly

includes a permeation component. At the bilayer surface, the lipid velocity is given by

$$\boldsymbol{V}^{\pm} = \boldsymbol{v}^{\pm} + v_n \boldsymbol{n}, \tag{2.14}$$

while the fluid velocity $\boldsymbol{V}_b^{\pm}$ on the surface is

$$\boldsymbol{V}_b^{\pm} \mid_{\Gamma} = \boldsymbol{v}^{\pm} + (v_n + v_n^p)\boldsymbol{n}, \tag{2.15}$$

where v_n^p is the permeation velocity across the membrane. We consider an infinite incompressible fluid at rest at infinity. Introducing the stress tensor from the bulk fluid $\boldsymbol{\sigma}_b$, and the rate of deformation tensor $\boldsymbol{D} = 1/2[\boldsymbol{\nabla V}_b + (\boldsymbol{\nabla V}_b)^T]$, the dissipation potential for a 3D Newtonian fluid reads [Happel and Brenner, 1965]

$$W_{\text{bulk}} = \frac{1}{2}\int_{\Omega} \boldsymbol{\sigma}^b : \boldsymbol{D}\ dV = \mu_b \int_{\Omega} \boldsymbol{D} : \boldsymbol{D}\ dV. \tag{2.16}$$

where μ_b is the ambient fluid shear viscosity.

Also, if the substrate is present and is dynamically interacting with the membrane, we include an additional dissipation term, to account for the friction between the lower monolayer and the substrate [Jonsson et al., 2009],

$$W_{b_s} = \frac{b_s}{2}\int_{\Omega} \|\boldsymbol{v}^-\|^2 dS,$$

where b_s is the corresponding friction coefficient.

2.4.3 Permeation dissipation

If the system is osmotically out of the equilibrium, the membrane allows for water permeation, which dissipates a significant amount of energy. Besides the lipid dissipation, the permeation dissipation also takes place at the membrane. It can be modeled

with the potential [Olbrich et al., 2000]

$$W_{perm}[v_n^p] = \frac{1}{2C}\int_\Gamma (v_n^p)^2 dS, \tag{2.17}$$

where C is a permeation coefficient generally expressed as $P_f V_w/(RT)$, P_f is a constant with units of velocity, and V_w is the volume of a water molecule.

2.5 Governing equations

The dynamics of the system can be obtained by minimizing the Rayleigh dissipation potential plus the rate of change of the elastic energy with respect to the variables expressing the rate of change of the system [Goldstein et al., 2001]. This minimization is often constrained, for instance by boundary conditions or a fixed enclosed volume. For this purpose, we form the Lagrangian

$$\mathcal{L}[v_n, v_n^p, \boldsymbol{v}^\pm, \boldsymbol{V}_b, \boldsymbol{\Lambda}] = W[v_n, v_n^p, \boldsymbol{v}^\pm, \boldsymbol{V}_b] + \dot{\Pi}[v_n, v_n^p, \boldsymbol{v}^\pm, \boldsymbol{V}_b] - \boldsymbol{\Lambda}\cdot\boldsymbol{C}[v_n, v_n^p, \boldsymbol{v}^\pm, \boldsymbol{V}_b], \tag{2.18}$$

where $\boldsymbol{C}[v_n, v_n^p, \boldsymbol{v}^\pm, \boldsymbol{V}_b]$ collects all the constraints and $\boldsymbol{\Lambda}$ the corresponding Lagrange multipliers. For instance, a fixed enclosed volume constraint for a closed bilayer is expressed as $\int_\Gamma v_n \; dS = 0$, and the associate Lagrange multiplier is the hydrostatic pressure jump across the bilayer. The governing equations are then obtained by making the Lagrangian stationary for all admissible variations

$$\delta_{v_n}\mathcal{L} = \delta_{v_n^p}\mathcal{L} = \delta_{\boldsymbol{v}^+}\mathcal{L} = \delta_{\boldsymbol{v}^-}\mathcal{L} = \delta_{\boldsymbol{V}_b}\mathcal{L} = \delta_{\boldsymbol{\Lambda}}\mathcal{L} = 0, \tag{2.19}$$

which is a form of the principle of virtual power. It is straightforward to include external forces such as a prescribed membrane tension at the boundary of a domain. From these equations, by integration by parts, the Euler-Lagrange equations can be derived by a direct calculation. The only term involving complex calculations is the membrane dissipation, see [Arroyo and DeSimone, 2009].

In an ALE formulation, the physics are independent of the choice of parametrization of the midsurface, and therefore independent on the tangential parametrization velocity $\boldsymbol{w}$. In numerical calculations, this allows us to freely choose the parametrization velocity, which can be interpreted as a mesh velocity. It can be prescribed, for instance to zero in a tangentially Eulerian approach, although this introduces numerical stiffness in the equations. It is also possible to exploit the freedom of the tangential motions of the mesh to adapt to discretization density to the features of the solution, although we do not attempt this here. Instead, we view the mesh velocity as an additional unknown. To break the invariance of the physical equations with respect to $\boldsymbol{w}$, we include a functional to damp the mesh velocity

$$\widehat{W}[\boldsymbol{w}] = \frac{\hat{\mu}}{2S}\int_{\Gamma} |\boldsymbol{w}|^2 dS, \tag{2.20}$$

where $\hat{\mu}$ is a numerical parameter with units of physical viscosity and S is the bilayer surface area. This functional can be understood as a penalty approach to enforce approximately the Eulerian gauge.

Once the lipid, shape, and parametrization velocities have been obtained from these equations, one can integrate in time the parametrization from Eq. (2.1), and monolayer densities from the local statement of balance of mass in Eq. (2.5).

2.6 Particularization to axisymmetric surfaces

We consider the parametric description of an axisymmetric surface in terms of the generating curve, i.e. the surface Γ_t at a given instant t by

$$\boldsymbol{x}(u,\theta,t) = \{r(u,t)\cos\theta, r(u,t)\sin\theta, z(u,t)\}, \tag{2.21}$$

where $u \in [0,1], \theta \in [0,2\pi]$, and $\{r(u,t), z(u,t)\}$ is the parametric description of the generating curve. The velocity of the parametrization is

$$\{r_{,t}, z_{,t}\} = w\boldsymbol{t} + v_n\boldsymbol{n},$$

where $\boldsymbol{t} = 1/a\{r', z'\}$ is a tangent unit vector to the generating curve, $\boldsymbol{n} = 1/a\{-z', r'\}$ a unit normal, and $a(u) = \sqrt{[r'(u)]^2 + [z'(u)]^2}$ is the norm of the curve speed. Throughout the paper, $(\cdot)'$ denotes partial differentiation with respect to the parameter u. From the above relations, we have

$$w = \frac{1}{a}(r'r_{,t} + z'z_{,t}), \qquad v_n = \frac{1}{a}(-z'r_{,t} + r'z_{,t}). \tag{2.22}$$

We assume that the tangential velocity of the lipids in each monolayer does not have azimuthal components, i.e. $\boldsymbol{v}^{\pm} = v^{\pm}\boldsymbol{t}$.

For axisymmetric surfaces, integrals on the surface can be brought to the interval $[0,1]$ with the relation $dS = (2\pi ar)du$. Following [Arroyo and DeSimone, 2009, Arroyo et al., 2012], the rate-of-deformation tensor can be written in an orthonormal coordinate system with basis vectors along the generating curves and the parallels of the surface as

$$\boldsymbol{d}^{\pm} = \frac{1}{a}\begin{bmatrix} v^{\pm\prime} & 0 \\ 0 & v^{\pm}r'/r \end{bmatrix} - \frac{v_n}{a}\begin{bmatrix} b/a^2 & 0 \\ 0 & z'/r \end{bmatrix},$$

where $b(u) = -r''(u)z'(u) + r'(u)z''(u)$. The mean and Gaussian curvature are given by

$$2H = \frac{1}{a}\left(\frac{b}{a^2} + \frac{z'}{r}\right), \qquad K = \frac{bz'}{a^4 r}.$$

The continuity equation (2.5) can be written as

$$\rho^{\pm}_{,t} + \rho^{\pm\prime}\frac{v^{\pm} - w}{a} + \rho^{\pm}\left[\frac{(rv^{\pm})'}{ra} - 2v_nH\right] = 0. \tag{2.23}$$

Specializing Eq. (2.13) in the present setting, the dissipation potentials can be

written concisely as

$$W_{b_m}[v^{\pm}] = \frac{b_m}{2}\int_0^1 \left[v^+, v^-\right] \begin{bmatrix} 1 & -1 \\ -1 & 1 \end{bmatrix} \begin{bmatrix} v^+ \\ v^- \end{bmatrix} (2\pi ar)du, \tag{2.24}$$

and

$$W_{\mu}[r_{,t}, z_{,t}, v^{\pm}] = \frac{1}{2}\int_0^1 \mathbf{U}^T\mathbf{A}\mathbf{U}\ (2\pi ar)du, \tag{2.25}$$

where $\mathbf{U}^T = [r_{,t}, z_{,t}, v^+, v^-, v^{+\prime}, v^{-\prime}]$ and $\mathbf{A}$ is a symmetric matrix given in Appendix A.3.

The parametrization dissipation potential takes the simple form

$$\widehat{W}[r_{,t}, z_{,t}] = \frac{\hat{\mu}}{S}\int_0^1 \frac{\pi r}{a}\left[r_{,t}, z_{,t}\right] \begin{bmatrix} r'^2 & r'z' \\ r'z' & z'^2 \end{bmatrix} \begin{bmatrix} r_{,t} \\ z_{,t} \end{bmatrix} du. \tag{2.26}$$

Similarly we implement the axisymmetric version of the elastic energy. With a view on the numerical implementation, rather than using the general expression in the previous section for the rate of change of the elastic energy, we can avoid third order derivatives of the parametrization of the generating curve by taking variations directly of the axisymmetric functional

$$\begin{aligned} \Pi[r, z, \rho^{\pm}] = & \int_0^1 \frac{K_s}{2}\left(\frac{\rho^{\pm}}{\rho_0} \mp 2dH - 1\right)^2 (2\pi ar)du \\ + & \int_0^1 \frac{\kappa}{2}(2H - C_0)^2(2\pi ar)du, \end{aligned} \tag{2.27}$$

which results in

$$\begin{aligned}\dot{\Pi}[r_{,t}, z_{,t}, \dot{\rho}^{\pm}] \;=\; & \int_0^1 K_s \Bigg[\left(\mp 2dH_{,t} + \frac{\rho^{\pm}_{,t}}{\rho_0}\right)\left(\frac{\rho^{\pm}}{\rho_0} \mp 2dH - 1\right) \\ & +2\kappa(2H - C_0)H_{,t}\Bigg](2\pi ar)du \\ & + \int_0^1 \Bigg[\frac{K_s}{2}\left(\frac{\rho^{\pm}}{\rho_0} \mp 2dH - 1\right)^2 \\ & +\frac{\kappa}{2}(2H - C_0)^2\Bigg]\left(a_{,t}r + ar_{,t}\right)2\pi du \end{aligned} \tag{2.28}$$

where $H_{,t}$, $a_{,t}$, and $\rho^{\pm}_{,t}$ are given in Appendix A.4. Using the continuity equation, $\dot{\Pi}$ becomes a functional of velocities only. Despite the long expressions, this functional has a simple structure of the form

$$\dot{\Pi}[r_{,t}, z_{,t}, v^{\pm}_t] = -\int_0^1 \mathbf{F}^T\mathbf{W}(2\pi ar)du \tag{2.29}$$

where $\mathbf{W}^T = \left[r_{,t}, r'_{,t}, r''_{,t}, z_{,t}, z'_{,t}, z''_{,t}, v^+, v^-, v^{+\prime}, v^{-\prime}\right]$ and $\mathbf{F}$ is a column vector depending nonlinearly on the shape and monolayer densities. This form highlights its linearity with respect to the variables expressing the rate of change of the system.

A common assumption when studying bilayer vesicles is that the enclosed volume remains constant [Seifert and Lipowsky, 1995]. This condition is expressed in the present setting as

$$0 = C^{\text{vol}}[r_{,t}, z_{,t}] = \dot{V} = \int_0^1 (-z'r_{,t} + r'z_{,t})(2\pi r)du.$$

Minimizing the Lagrangian subject to the constraints, one can find the velocities $\{r_{,t}, z_{,t}, v^{\pm}\}$ at each configuration $\{r, z, \rho^{\pm}\}$. Then, the surface parametrization can be integrated in time from $\{r_{,t}, z_{,t}\}$, and the monolayer densities from the continuity equation.

2.7 Summary

We have proposed a comprehensive dynamical continuum model for lipid bilayers to investigate out-of-equilibrium phenomena. With a particular attention to the membrane fluidity, our model includes important internal and external dissipative mechanisms, coupled with the membrane bending and stretching elasticity. Assuming an interfacial, Newtonian compressible flow for each monolayer, and for axisymmetric surfaces, we have derived the governing equations of the bilayer viscoelasticity, which will be used in the following chapters, to be implemented numerically or to be particularized for different physical situations.

Chapter 3

Numerical approximation

In this chapter, we discretize the governing equations with a Galerkin method. We represent numerically shape and the surface physical fields using B-Splines and derive the space-discretized form of the governing equations, a system of differential-algebraic equations.

3.1 Spacial semi-discretization

3.1.1 Shape and physical fields on the membrane

The generating curve of the axisymmetric surface is represented numerically as a B-Spline curve

$$\{r(u,t), z(u,t)\} \approx \sum_{I=1}^{N} B_I(u) \underbrace{\{r_I(t), z_I(t)\}}_{\mathbf{P}_I(t)}, \tag{3.1}$$

where $B_I(u)$ are the B-Spline basis functions Piegl and Tiller [1997] defined on the interval $[0,1]$, and $\{r_I(t), z_I(t)\}$ is the position of the $I-$th control point of the B-Spline curve at instant t. Similarly, the density field is represented as

$$\rho^{\pm}(u;t) \approx \sum_{I=1}^{N} \tilde{B}_I(u)\rho_I^{\pm}(t). \tag{3.2}$$

We then have

$$\begin{aligned} \{r_{,t}, z_{,t}\} &\approx \sum_{I=1}^{N} B_I(u) \underbrace{\{\dot{r}_I(t), \dot{z}_I(t)\}}_{\dot{\mathbf{P}}_I(t)}, \\ \rho^{\pm}_{,t} &\approx \sum_{I=1}^{\tilde{N}} \tilde{B}_I(u) \dot{\rho}^{\pm}_I(t). \end{aligned} \tag{3.3}$$

Finally, the tangential velocity of each monolayer can be numerically expressed by,

$$v^{\pm}(u;t) \approx \sum_{I=1}^{\hat{N}} \hat{B}_I(u) v^{\pm}_I(t). \tag{3.4}$$

We note that the basis functions for the parametrization of the curve, the density field and the velocity field can be B-Splines of different orders. Since the energy functional involves second derivatives of r and z, B_I need to be at least quadratic B-Splines to have continuous derivatives and square-integrable second derivatives. While higher order B-Splines have superior accuracy, their computational cost is also higher, because the bandwidth of the dissipation matrices described below becomes larger, and the numerical integration requires more quadrature points. We found the results to be quite insensitive to the degree of the basis functions, and in the calculations we consider cubic B-Splines for the shape and for the tangential velocity fields, and quadratic B-Splines for the density. This combination provides stable and accurate results at a reasonable computational cost.

3.1.2 Bulk velocity field

We represent numerically the bulk velocity field using finite element approximation to derive the space-discretized form of the bulk dissipation.

The 3D velocity field can be represented numerically as

$$\boldsymbol{V}_b(\boldsymbol{X},t) \approx \sum_{I=1}^{n_b} \boldsymbol{N}_I(\mathscr{X})\boldsymbol{V}_{bI}(t), \qquad \boldsymbol{X} \in \Omega, \qquad \mathscr{X} \in \bar{\Omega}, \tag{3.5}$$

By $\boldsymbol{N}_I$, we denote the 3D shape functions and by $\bar{\Omega}$, we denote the parametric space.

3.2 Discretized form of the governing equations

Plugging these representations into Eqs. (2.24,2.25,2.26,2.29), and making the Lagrangian stationary with respect to $\dot{\mathbf{P}}_I$, $v_I^{\pm}$, and the Lagrange multipliers $\boldsymbol{\Lambda}$ we obtain a system of differential algebraic equations (DAEs)

$$\begin{bmatrix} \mathbf{D}_{\text{mem}} & \mathbf{0} \\ \mathbf{0} & \mathbf{D}_{\text{bulk}} \end{bmatrix} \begin{bmatrix} \dot{\mathbf{P}} \\ \mathbf{V} \\ \mathbf{U}_b \end{bmatrix} + \begin{bmatrix} \widehat{\mathbf{D}} & \mathbf{0} & \mathbf{0} \\ \mathbf{0} & \mathbf{D}_{\text{fr}} & \mathbf{0} \\ \mathbf{0} & \mathbf{0} & \mathbf{0} \end{bmatrix} \begin{bmatrix} \dot{\mathbf{P}} \\ \mathbf{V} \\ \mathbf{U}_b \end{bmatrix} + \mathbf{Q}\boldsymbol{\Lambda} = \begin{bmatrix} \mathbf{f}(\boldsymbol{\rho},\mathbf{P}) \\ \mathbf{0} \end{bmatrix},$$
$$\mathbf{Q}^T \begin{bmatrix} \dot{\mathbf{P}} \\ \mathbf{V} \\ \mathbf{U}_b \end{bmatrix} = \mathbf{0}, \tag{3.6}$$

where the global column arrays $\mathbf{P}$, $\mathbf{V}$, $\mathbf{U}_b$ and $\boldsymbol{\rho}$ collect all the degrees of freedom, $\mathbf{U}_b = [\boldsymbol{V}_{b1}^T, \boldsymbol{V}_{b2}^T, ..., \boldsymbol{V}_{bn_b}^T]^T$, $\mathbf{V}$ collects the surface velocity of outer and inner monolayers, and $\mathbf{D}_{\text{mem}}$ has the dimention of $\dot{\mathbf{P}}$ and $\mathbf{V}$. All the dissipation and constraint matrices depend nonlinearly on $\mathbf{P}$. The constraint matrix $\mathbf{Q}$ encodes boundary conditions, possibly the fixed volume constraint, and the no-slip condition between the bulk fluid and the bilayer.

The membrane dissipation matrix $\mathbf{D}_{\text{mem}}$ follows from Eq. (2.25) and takes the form

$$\mathbf{D}_{\text{mem}} = \int_\Gamma \mathbf{B}^T\mathbf{A}\mathbf{B}\, dS,$$

where $\mathbf{B}$ is a matrix whose entries are B_I, $\hat{B}_I$ and $\hat{B}'_I$, the integrals are performed

by Gaussian numerical quadrature and the global matrix is filled with the standard assembly process in finite elements (Belytschko et al. [2000]). Similarly, the inter-monolayer friction matrix is assembled from local matrices of the form

$$(\mathbf{D}_{\text{fr}})_{IJ} = b_m \int_\Gamma \begin{bmatrix} \hat{B}_I & 0 \\ 0 & \hat{B}_I \end{bmatrix} \begin{bmatrix} 1 & -1 \\ -1 & 1 \end{bmatrix} \begin{bmatrix} \hat{B}_J & 0 \\ 0 & \hat{B}_J \end{bmatrix} dS,$$

and for the parametrization dissipation we have

$$(\widehat{\mathbf{D}})_{IJ} = \frac{\hat{\mu_s}}{S} \int_\Gamma \frac{1}{a^2} \begin{bmatrix} B_I & 0 \\ 0 & B_I \end{bmatrix} \begin{bmatrix} r'^2 & r'z' \\ r'z' & z'^2 \end{bmatrix} \begin{bmatrix} B_J & 0 \\ 0 & B_J \end{bmatrix} dS,$$

From Eq. (2.29) we have

$$\mathbf{f} = \int_\Gamma \bar{\mathbf{B}}^T \mathbf{F} \; dS,$$

where now $\bar{\mathbf{B}}$ is filled with B_I, B'_I, B''_I, $\hat{B}_I$ and $\hat{B}'_I$.

The continuity equation is a partial differential equation governing the evolution of the density field. Due to the convective term $(\boldsymbol{c}^\pm \cdot \nabla\rho)$, the Galerkin finite element method needs to be stabilized. We use the standard Streamline Upwind Petrov Galerkin (SUPG) stabilization method (Belytschko et al. [2000], Donea and Huerta [2003]). After spacial discretization, see Appendix B.1, the continuity equation can be written as

$$\mathbf{M}^\pm \dot{\boldsymbol{\rho}}^\pm + \mathbf{L}^\pm \boldsymbol{\rho}^\pm = 0, \tag{3.7}$$

where the $\mathbf{M}$ and $\mathbf{L}$ matrices depend on $\dot{\mathbf{P}}$ and $\mathbf{V}$.

The system of DAEs can be understood as follows. Given a state of the system at time t, $(\mathbf{P}(t), \boldsymbol{\rho}(t))$, we find $\mathbf{V}(t)$, $\boldsymbol{\Lambda}(t)$ and $\dot{\mathbf{P}}(t)$ from Eq. (3.6). We then use Eq. (3.7) to compute $\dot{\boldsymbol{\rho}}(t)$. Thus, we can formally express the rate of change of the system as $(\dot{\mathbf{P}}(t), \dot{\boldsymbol{\rho}}(t)) = \boldsymbol{G}(\mathbf{P}(t), \boldsymbol{\rho}(t))$. We integrate forward in time this ODE with specialized semi-implicit ODE solvers for stiff problems (Shampine et al. [1999]).

Chapter 4

Numerical results

We exercise now the model in selected applications of interest. We first revisit the problem of tether extension as a validation of our model and simulations. We then present a suite of examples that illustrate the diversity of dynamical regimes of lipid bilayers, all of which bear biological relevance. We have carefully checked the convergence of the numerical approximation by mesh refinement. We find that the numerical method is robust to the order of the B-Spline basis functions, to the parametrization dissipation coefficient $\hat{\mu_s}$, and to the stabilization parameter τ of the SUPG method. In the examples presented here, we use at most 100 basis functions for each of the unknowns, r, z, $\rho^{\pm}$, and $v^{\pm}$. In examples studied in the present chapter, we focus on the role of the membrane viscosity and interlayer frictions.

4.1 Material parameters and time scales

Since our model includes several energetic and kinetic coupled mechanisms, the choice of material parameters (κ, K_s, μ_s, b_m, and d) plays an important role in the behavior of the system, and there is no canonical nondimensionalization of the equations (λ_s does not play a major role). Note carefully that K_s and μ_s are monolayer parameters, and therefore a factor of 2 is needed to relate the model to some reported measurements. We set the distance between the bilayer midsurface and the monolayer neutral surface to $d = 1$ nm. It is useful to define non-dimensional parameters comparing elastic and

dissipative mechanisms respectively. On the one hand, $\epsilon = \kappa/(2K_s d^2)$ takes values on the order of 1 for lipid bilayers. On the other hand, $\alpha = 2\mu_s/(b_m d^2)$ shows a larger variability. With reported values for the membrane shear viscosity $10^{-10} < 2\mu_s < 5 \cdot 10^{-9}$ Js/m^2 and for the inter-monolayer friction $10^8 < b_m < 10^9$ Js/m^4, α ranges between 0.1 and 50. Here we consider $\alpha = 1$. In all the simulations, we consider $\kappa = 10^{-19}$ J, $2K_s = 0.1$ J/m^2, $b_m = 10^9$ Js/m^4 and $2\mu_s = 10^{-9}$ Js/m^2 [Dimova et al., 2002, 2006].

We discuss next a number of time scales that govern the dynamics under different circumstances. Let us denote by $\bar{\rho}$ the density average and by $\hat{\rho}$ the density difference between the two monolayers, normalized by ρ_0. At fixed shape, the gradients in the density difference $\hat{\rho}$ have been shown to evolve according to a diffusion equation with diffusivity $D = K_s/b_m$ [Evans and Yeung, 1994], which introduces a relaxation time scale $t_1 = \bar{S}/D$, where $\bar{S}$ is the relevant area, here of a density difference disturbance. Density differences can also relax by changing shape and creating curvature, see Fig. 4.5, which when dragged by membrane viscosity gives rise to the time scale $t_2 = \sqrt{\bar{S}}\mu_s/(K_s d\hat{\rho})$. For our parameter choice, $t_2/t_1 = \alpha d/(2\sqrt{\bar{S}}\hat{\rho})$, and therefore in most cases the density difference relaxation by inter-monolayer friction is slower than by membrane viscosity (induced by shape changes). When the shape change is driven by curvature elasticity, $t_3 = \bar{S}\mu_s/\kappa$ is relevant. Gradients in the density average $\bar{\rho}$ do not mobilize the inter-monolayer friction and exhibit an extremely fast characteristic time scale $t_4 = \mu_s/(K_s\bar{\rho})$, typically smaller than a microsecond, which needs to be resolved by the simulations at initial stages. When the dynamics mobilize bending energy and inter-monolayer friction, the relevant time scale is $t_5 = \bar{S}d^2 b_m/\kappa$. Some of these time scales have been considered previously, e.g. [Sens, 2004].

4.2 Dynamics of tether formation and extrusion

The statics of bilayer tubular structures has been extensively studied from a theoretical point of view. One can easily estimate the equilibrium configuration of a tether pulled out of a giant vesicle under constant surface tension σ by minimizing the energy of a

uniform cylindrical membrane $E = \pi\kappa L/r + 2\pi\sigma r L$ with respect to the tube length L and radius r, leading to expressions for the equilibrium radius $r = \sqrt{\kappa/2\sigma}$, and for the static force needed hold the tube

$$f^s = \pi\kappa/r + 2\pi\sigma r = 2\pi\sqrt{2\kappa\sigma}. \tag{4.1}$$

The equilibrium force during quasi-static tether nucleation, eventually converging to f^s, has been studied theoretically [Powers et al., 2002, Derényi et al., 2002].

The dynamical features of tether growth and retraction have been investigated theoretically and experimentally in many studies [Evans and Yeung, 1994, Li et al., 2002, Rossier et al., 2003]. Evans and Yeung [Evans and Yeung, 1994] considered a giant vesicle kept at constant tension σ by a micro-pipette, and pulled out a tether with an adhesive micro bead at constant velocity $\dot{L}$. They provided a theoretical estimation of the pulling force f when the tube area is much smaller than that of the vesicle

$$\begin{aligned} f &= 2\pi\left(r\sigma + \frac{\kappa}{2r}\right) + 2\pi\left(\frac{2K_s d^2}{R^2}\right) L \\ &\quad + 2\pi \underbrace{\left[2\mu_s - 3\mu_b r + \left(4b_m d^2\right)\ln\frac{R}{r}\right]}_{\eta_{\text{eff}}} \dot{L}, \end{aligned} \tag{4.2}$$

where μ_b denotes the water viscosity, R denotes the radius of the vesicle, and η_{eff} denotes the effective viscosity of the tether. The first line is an elastic force f_{elast}, with a first term corresponding to the constant static force f^s and a second term, proportional to the tether's length, accounting for the global area difference between the monolayers. The second line is the rate-dependent force f_{rate}, which groups all hydrodynamic effects, i.e. the bulk and membrane viscous forces and the slippage between the monolayers at the tether's neck. For large vesicles, the nonlocal elastic term can be neglected, and the viscous forces are overwhelmingly dominated by inter-monolayer friction.

We test our simulations against these theoretical predictions. We remove the

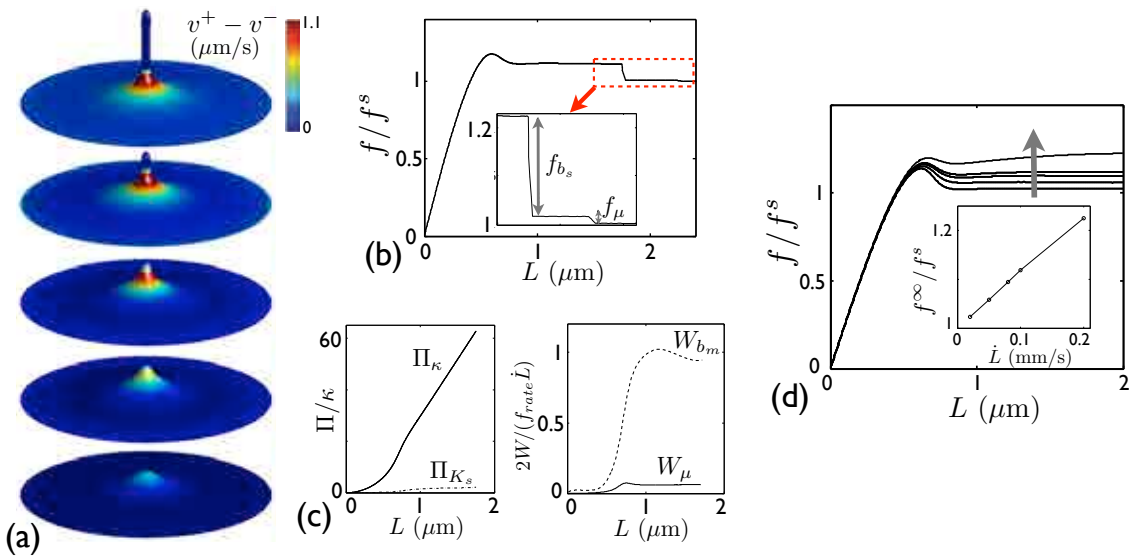

Figure 4.1: Nucleation and extension of a tether out of a planar disk of radius 2 µm kept at constant surface tension ($\sigma = \sigma^+ + \sigma^- = 10^{-4} K_s$). All figures but the right plot are for a pulling rate $\dot{L} = 0.1$ mm/s. (a) Selected snapshots with a colormap of the inter-monolayer slippage velocity. Once the tether is fully formed, the process reaches a steady state, where the shape, slippage at the neck, and the radius of the tether do not change. (b) Force-extension curve normalized by the static tether force in Eq. (4.1). The end of the process and the inset highlight the effect of membrane shear viscosity and inter-monolayer friction on the dynamical part of the force. (c) Evolution of the elastic energy (Π) and dissipation power ($2W$) components during the process. (d) Effect of the loading rate for $\dot{L} = 0.02, 0.05, 0.08, 0.1, 0.2$ mm/s. The arrow indicates increasing rate. The inset shows the normalized steady-state force f^∞ as a function of strain rate. From the slope of this curve, we can compute the effective tether viscosity η_{eff} in Eq. (4.2).

nonlocal effect by pulling a tether out of large enough planar membrane disk of radius R with constant surface tension σ boundary condition, and uncoupled monolayers (other than by frictional forces). More specifically, at the boundary of the disk ($u = 1$), the parametric surface does not move $r_{,t}(1) = 0$ and $z_{,t}(1) = 0$, and a power of the form $\pi R\sigma v^{\pm}(1)$ is added to the variational principle. The tangential velocities at the boundary of the domain $v^{\pm}(1)$ are free, and are taken into account in the balance of mass since the system exchanges mass with its surrounding. Figure 4.1 shows a tether nucleation and extraction at constant rate. The color map, Fig. 4.1(a), shows the velocity difference between the leaflets, visualizing the inter-monolayer slippage at the tether's neck. The radius of the tube during this process ranges between 71.1 and 76.3 nm. By stopping the extraction, we check that the small deviation from the static radius ($r = 70.7$ nm) is due to dynamical effects. The maximum pulling force, about 1.17 f^s, is attained for a critical length 0.32 R, a value known to depend on the radius of the vesicle or the disk [Derényi et al., 2002]. The steady state pulling force from our simulations is $f^{\infty} = 1.12\ f^s$, where the 12% deviation from f^s is explained by the additional terms in Eq. (4.2). To assess their magnitude, we annihilate in the computations the friction coefficient first, and then the membrane viscosity. The resulting drops in the tether force are shown in the inset of Fig. 4.1(b). Most of the rate-dependent part of the force is due, as expected, to inter-monolayer friction. The membrane shear viscosity contribution is only $f_{\mu_s} = 0.00712\ f^s$, very close to the the theoretical estimation from Eq. (4.2), $0.00707\ f^s$, which shows the quantitative agreement between the simulations and the available theoretical predictions. We can further understand the phenomenon by tracking elastic energies and dissipation powers during the process, Fig. 4.1(c). It can be observed that, while the stretching energy slightly deviates from zero due to rate effects, the curvature energy grows significantly during the experiment. This is not surprising, since most of the resisting force is static and explained by f_s. Before the tube has fully nucleated, the growth of the curvature energy is quadratic, and after the buckling event that forms the tether, it grows linearly, with as slope that we check is very close (within 1%) to half f^s as predicted by Eq. (4.1). It can also be observed that most of the dissipation in this

process is due to inter-monolayer friction. It can be easily seen from Eq. (4.2) that the viscoelastic time constant for this process is $t_5 = \bar{S}d^2 b_m/\kappa = rLd^2 b_m/\kappa$. Recalling the expression for the tube radius, the characteristic tether pulling velocity at which viscous forces are comparable to elastic forces is $\dot{L}_c = L/t_5 = \sqrt{2\kappa\sigma}/(4b_m d^2) \approx 0.25$ mm/s, in agreement with our results, Fig. 4.1(d).

The left plot in Fig. 4.1 shows the effect of pulling rate on the resisting force. The rate of the process changes slightly the bucking point, but more importantly the steady state force f^∞ increases with rate. From Eq. (4.2), the slope of f^∞ as a function of $\dot{L}$ should provide the effective tether viscosity η_{eff} (see the figure inset), which has been examined experimentally [Waugh, 1982, Li et al., 2002]. We find that for the largest rate, the relation slightly departs from linearity, due to the dynamically induced elastic force resulting from Π_{K_s} mentioned above.

In summary, this example validates our model and simulations in a well-understood situation, and provides a detailed picture of the rate effects during such process. Tether extension may behave quite differently, for instance for vesicles pulled at two opposing points [Lee et al., 2008]. In this reference, the tension is not constant but rather increases as the tethers are extended, and therefore these thin down.

We also consider a flaccid vesicle ($R = 4$ µm) with the reduced volume equal to 0.9, pulled out with a constant rate ($\dot{L}_t = 0.075$ mm/s) on one point while the opposite side is fixed. Figure 4.2 presents the dynamic tether formation from a large vesicle (the color map represents the velocity difference between the leaflets). In this figure, the shape deformations of the tether and the vesicle are remarkable. We show the variations of the average surface stress during the tether extraction. Interestingly, the surface tension is increasing linearly after the onset of buckling similar to the pulling force. We understand this linear in growth in terms of quadratic growth of the extensional energy. We note that bending energy increases linearly resulting in a constant force contribution. We also investigate the importance of each dissipative mechanism in this dynamical process. The contribution of the membrane dissipation before the tubulation is larger here than in the tethering from a planar membrane with a constant surface tension. Due to the considerable global shape changes in

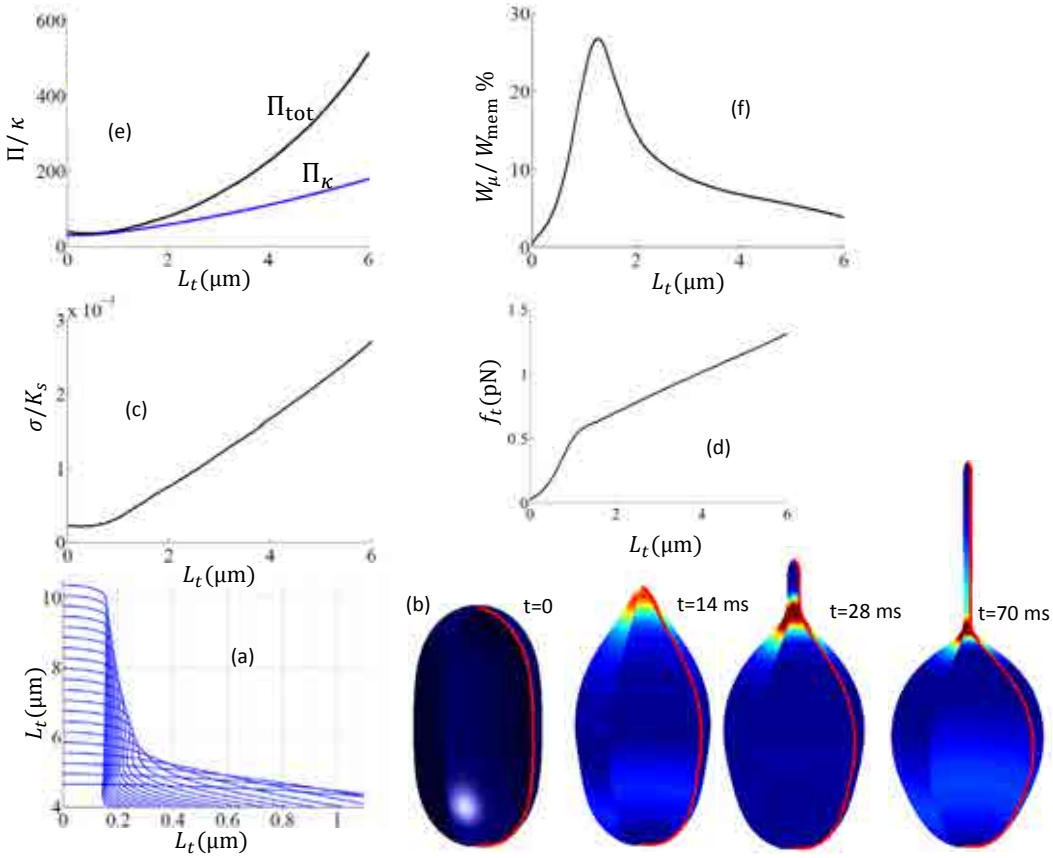

Figure 4.2: Nucleation and extension of a tether out of a vesicle of radius 4 µm with a constant pulling rate ($\dot{L}_t = 0.075$ mm/s). (a) Generating curves of the membrane highlighting the tether formation. As the tether is pulled, shape and radius change. (b) Selected snapshots with a colormap of the inter-monolayer slippage velocity. (c) Total surface tension, $\sigma^+ + \sigma^-$, as computed from appendix A.1, averaged over the vesicle surface. (d) Force-extension curve grows linearly as a consequence of the quadratic growth of the extensional energy. (e) Evolution of the elastic energy, Π_{tot}, Π_κ, and their difference represents the stretching energy. (f) Contribution of the shear viscosity in total membrane dissipation during the process $W_{\mu_s}/(W_{\mu_s} + W_{b_m})$. The rest of the dissipation is balanced by interlayer friction.

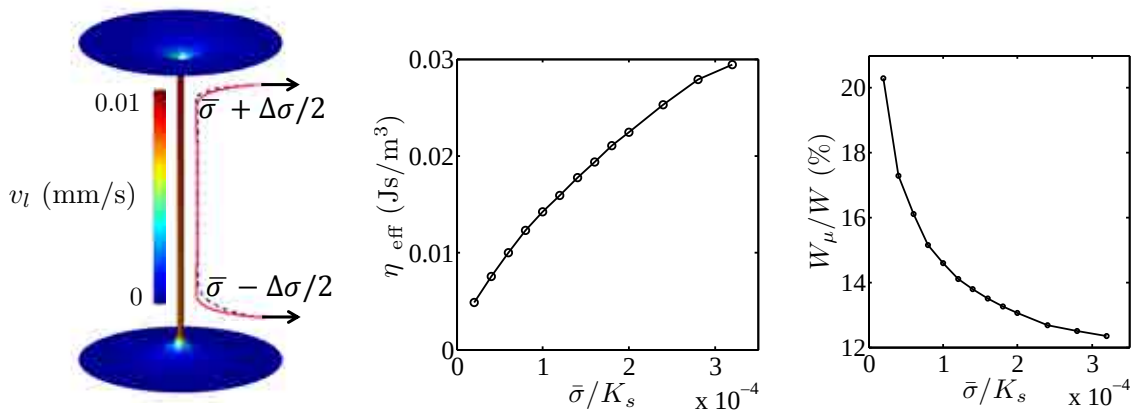

Figure 4.3: Cell-to cell communication via tunneling nanotubes. Geometry and lipid velocity field of the inner monolayer at steady state for $\Delta\sigma = 1.36 \cdot 10^{-4}$ mN/m and $\bar{\sigma} = 0.005$ mN/m $= 10^{-4} K_s$, corresponding to $r = 100$ nm (left). The shape change as a result of the tension difference is highlighted by the dashed-blue generating curve, to be compared with the static shape (solid-red line). Effective viscosity as a function of the average tension between the two connected membrane patches $\bar{\sigma}$ (middle). Fraction of the of the membrane shear dissipation relative to the total dissipation as a function of $\bar{\sigma}$ (right).

the vesicle. Interestingly the interlayer friction contribution increases after the tube formation, since the tube neck decreases gradually.

4.3 Cell communication via tunneling nanotubes

In recent years, a novel cell-to-cell communication mechanism mediated by membrane nanotubes bridging animal cells has been identified. Such open-ended membrane tethers, called tunneling nanotubes (TNTs) have been shown to facilitate physiological functions in cell-to-cell communication during health and disease [Rustom et al., 2004, Gerdes and Carvalho, 2008, Dubey and Ben-Yehuda, 2011]. For instance, there is evidence that HIV-1 can spread quickly via TNTs between cells in the human immune system [Sowinski et al., 2008].

TNTs have diameters $2r$ ranging from 50 to 200 nm and lengths L of up to tens of micrometers. Transport of objects through TNTs has been shown *in vitro* to be mostly driven by the difference of surface tension $\Delta\sigma$ between the connected liposomes, and

not by the internal pressure difference Δp [Karlsson et al., 2002]. Indeed, the fluid velocity profile inside the tube can be expressed as $v(s) = v_l - v_0\,[1-(s/r)^2]$, where s is the radial position, v_l is the inner monolayer lipid velocity driven by the tension difference $\Delta\sigma$, and $v_0 = r\Delta p/(2\mu_b L)$ is the amplitude of the backward flow due to the pressure difference. For long thin tubes, v_0 can be neglected. As before, the radius of the connecting tube can be estimated by $r = \sqrt{\kappa/2\bar{\sigma}}$ where $\bar{\sigma}$ is the average tension between the two cells. This phenomenon, driven by gradients in the surface tension, can thus be interpreted as a Marangoni effect.

We consider a long tether ($L = 8$ µm) bridging two giant vesicles modeled by two circular disks of radius $R = 3$ µm, see Fig. 4.3 (left). Initially, we obtain the static equilibrium by fixing the same surface tension at the top and bottom boundaries. Then, we induce the lipid flow by increasing the tension difference $\Delta\sigma$, while their average $\bar{\sigma}$ is fixed. If the process is performed very slowly, we can assume that the membrane flow is at steady state. We visualize the flow of the lipid membrane by the lipid velocity of inner monolayer v_l. The velocity is not uniform along the tube due to the gradient of the surface tension, which in turn changes the tube radius. The figure illustrates the steady state shape after the tension difference has been applied (blue dashed line) compared to the equilibrium shape for $\Delta\sigma = 0$ (solid-red line). We can define an effective viscosity relating the velocity of the lipids to the tension difference, $\Delta\sigma = \eta_{eff} v_l$. We find that indeed the relation between v_l and $\Delta\sigma$ is linear in a wide range of tension differences of up to 20% of $\bar{\sigma}$. Figure 4.3 (middle) shows how the effective viscosity increases with average tension (as the tube radius decreases). As the tube becomes narrower, the role of inter-monolayer friction relative to membrane shear viscosity increases in setting η_{eff}, see Fig. 4.3 (right). Remarkably, for tubes in the physiological range, the membrane shear viscosity contributes between 10 and 20% of the total dissipation, and is therefore not negligible for quantitative predictions. Focusing on the main contribution, we can estimate the order of magnitude of the effective viscosity by scaling arguments as $\eta_{eff} \approx b_m d^2/r = b_m d^2\sqrt{2\bar{\sigma}/\kappa}$, leading to a characteristic time for transport across the TNT of $t_6 = b_m d^2 L\sqrt{2\bar{\sigma}/\ kappa}/\Delta\sigma$.

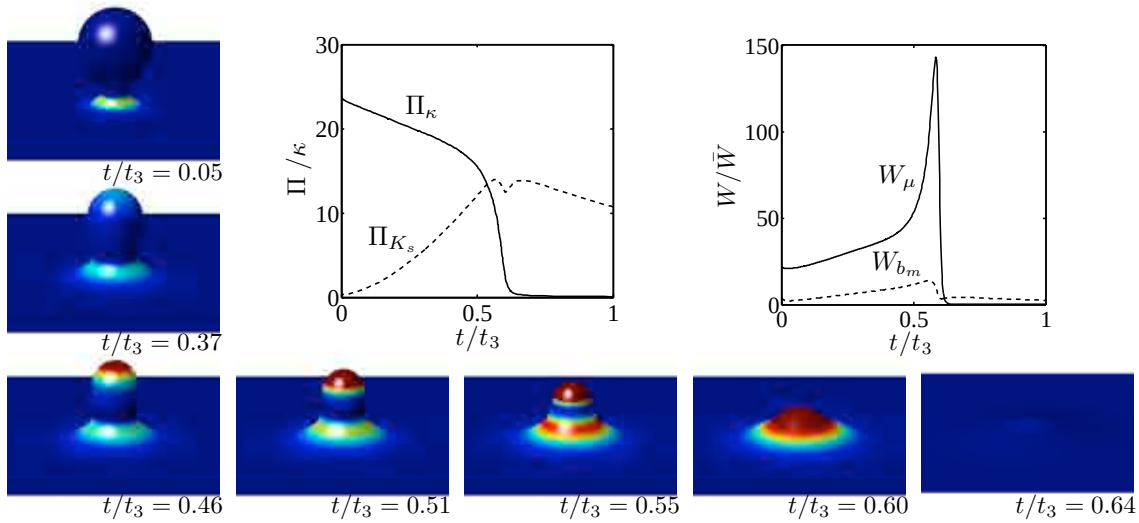

Figure 4.4: Relaxation dynamics of a bud of radius $R = 0.34$ µm connected to a tense planar membrane disk ($\sigma = 0.006$ mN/m). The color map on the snapshots shows the membrane dissipation power density in the same scale during the process. The left plot shows the curvature and stretching elastic energies during the process, while the right plot shows the membrane shear and inter-monolayer friction dissipation powers, in non dimensional terms with $\bar{W} = 2\mu_s \bar{S}/t_3^2$. Here, $t_3 \approx 3.6$ ms. The stretching energy Π_{K_s} due to the lipid density asymmetry arising from the bud absorption relaxes following the time scale $t_1 \approx 15$ ms (not shown).

4.4 Bud relaxation

We consider now the relaxation of a vesicle that has formed a fusion pore with a planar membrane disk under constant tension. Figure 4.4 shows selected snapshots of the process, by which the bud is eventually absorbed completely and the bilayer disk becomes planar. Here, the curvature forces are the main elastic mechanism driving the process (see Fig. 4.4, left plot). The applied membrane tension also drives the absorption. The dominant dissipative mechanism is the membrane shear dissipation (see Fig. 4.4, right plot), and therefore, as expected, the relaxation dynamics are governed by $t_3 \approx 3.6$ ms. It can be observed that, during the bud absorption, some amount of stretching elasticity is stored since initially the bud and the planar bilayer were at their equilibrium lipid density. The density difference created as the bud disappears then dissipates slowly through inter-monolayer friction in a time scale of

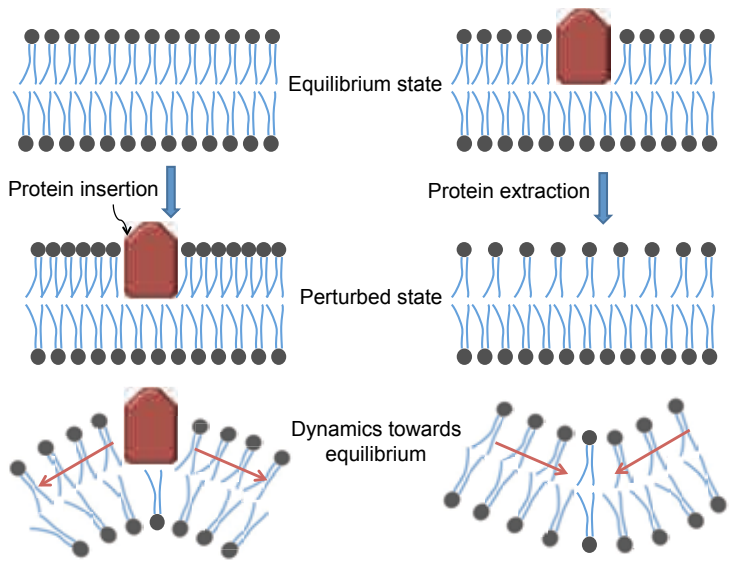

Figure 4.5: Illustration of how a molecule insertion/extraction in a monolayer disturbs the lipid density asymmetrically. The lipid density contrast across the monolayers can be relaxed either by flowing lipids away from/towards the disturbance (thin red arrows), or by curving the bilayer to form buds/invaginations.

$t_1 \approx 15$ ms.

The process proceeds first rather slowly, with the membrane shear dissipation concentrated at the neck of the bud. Recalling Eqs. (2.12,2.13), we can interpret that this localized shear dissipation density is caused by tangential velocity gradients. As the neck opens up, the membrane dissipation becomes larger at the top of the bud, now caused by the large normal velocity and curvature in this region, see Eq. (2.12). At a critical point ($t \approx 0.6\, t_3$), the curvature elastic energy sharply decreases, accompanied by a high membrane dissipation. The snapshots illustrate how the change in geometry facilitates the lipid flow, and as a consequence speeds up the shape transition.

4.5 Density asymmetry excitations in vesicles

Organelles and cells are often placed out-of-equilibrium by localized density disturbances caused by a myriad of physicochemical phenomena. Proteins or polymers

inserting the bilayer, effectively changing the lipid packing, can induce shape changes [Shibata et al., 2009, Tsafrir et al., 2003]. Lipid molecules can locally change their shape and size, for instance under localized pH alterations, leading to transient shape changes [Fournier et al., 2009, Khalifat et al., 2008]. Lipid translocation between the monolayers driven by flippases can induce budding [Sens, 2004, Papadopulos et al., 2007]. Figure 4.5 illustrates how the insertion/extraction of a molecule in one monolayer locally increases/decreases the lipid density, mobilizing inter-monolayer slippage and/or creating curvature.

In this study, we focus on deflated, spheroidal, axisymmetric vesicles initially in equilibrium. Since lipid membranes are almost area preserving, a completely spherical vesicle is too tight to allow for shape changes. The excess area relative to the vesicle volume is conventionally quantified by the reduced volume, defined as the ratio between the enclosed volume and the volume of a sphere with equal surface area. We start with a prolate spheroid, with a reduced volume of 0.98, although analogous results are found with prolate shapes as long as there is available excess area to change shape without stretching significantly the bilayer. In fact, the last example presented here exhibits a transition between a prolate and an oblate configuration, triggered by a localized density asymmetry. We consider a small vesicle of radius $R = 100$ nm, a large vesicle ($R = 2$ µm) and a giant vesicle ($R = 4$ µm). We chose a different number of lipids in each monolayer so that the equilibrium density in the neutral surface of the monolayers is close to ρ_0. To accomplish this, we set initially the projected densities to $\rho^{\pm} = \rho_0(1 \pm 2d/R)$, and then find the equilibrium state by minimizing Π subject to the mass and volume constraints, which slightly perturbs $\rho^{\pm}$ due to the non-uniform curvature of the prolate shape.

Once the initial state has been prepared, we locally perturb the lipid density of the outer monolayer, and examine numerically the relaxation dynamics. Specifically, the lipid density at the neutral surface of the outer monolayer $\hat{\rho}^{+}$ is disturbed with the profile $\delta\rho \times f(\phi)$ shown in Fig. 4.6, where $\phi \in [0, \pi]$ is the spherical angle of the vesicle domain. We choose the width of the disturbance and its amplitude as $w = 10$ % and $\delta\rho = 0.05\ \rho_0$.

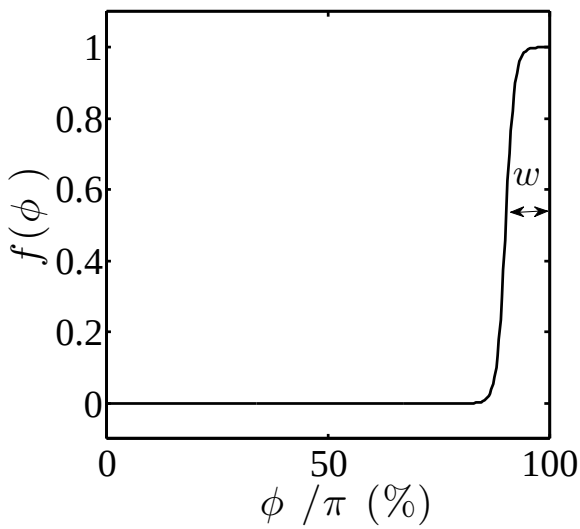

Figure 4.6: Profile of the density perturbation on the outer monolayer. The density at the neutral surface $\hat{\rho}^+$ is disturbed by $\delta\rho \times f(\phi)$. With our choice of width of the profile, $w = 10$ %, the disturbance occupies about 2.5% of the area of the vesicle.

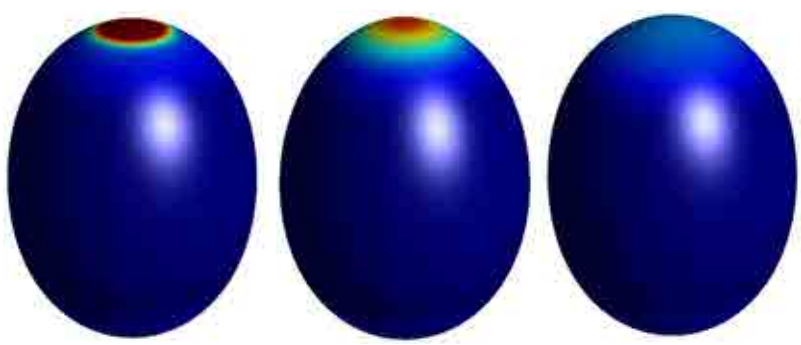

Figure 4.7: Relaxation dynamics of the small vesicle ($R = 100$ nm, $t_1 = 0.06$ ms, $t_2 = 0.02$ ms). The density disturbance diffuses without noticeable shape changes. The color maps represent the difference between the monolayer lipid densities at the neutral surface, $\hat{\rho}^+ - \hat{\rho}^-$, where red corresponds to $\delta\rho$ and blue to 0.

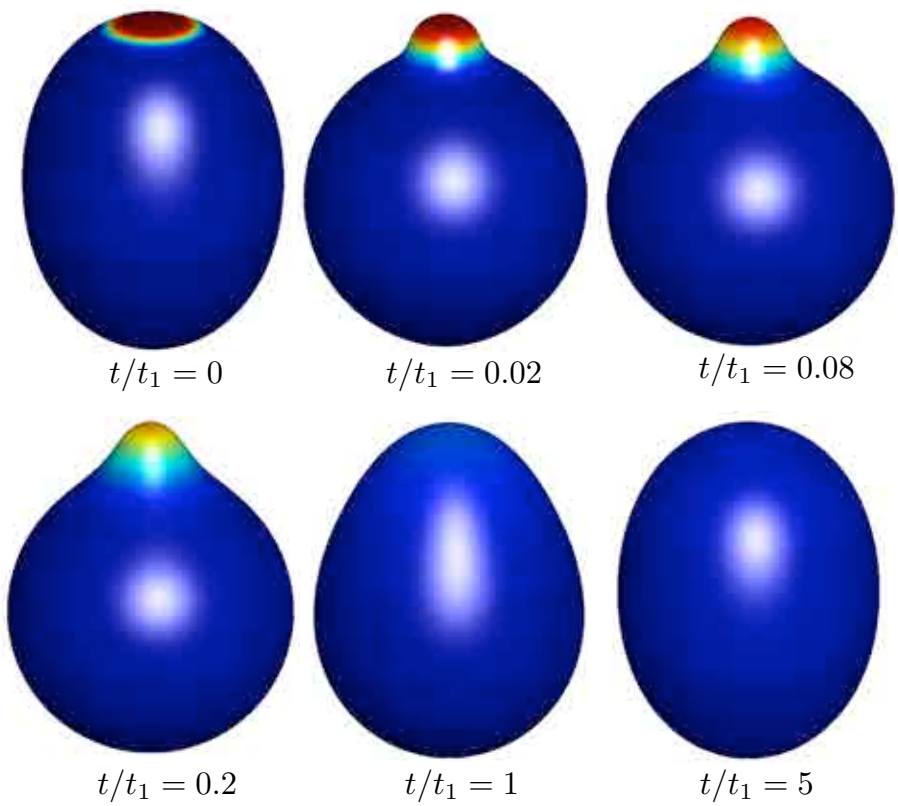

Figure 4.8: (Color online) Relaxation dynamics of the large vesicle ($R = 2$ µm, $t_1 = 25$ ms, $t_2 = 0.44$ ms). At early stages, the density disturbance relaxes by forming a bud, which then disappears and the density difference diffuses by inter-monolayer friction. The color maps represent the difference between the monolayer lipid densities at the neutral surface, $\hat{\rho}^+ - \hat{\rho}^-$, where red corresponds to $\delta\rho$ and blue to 0.

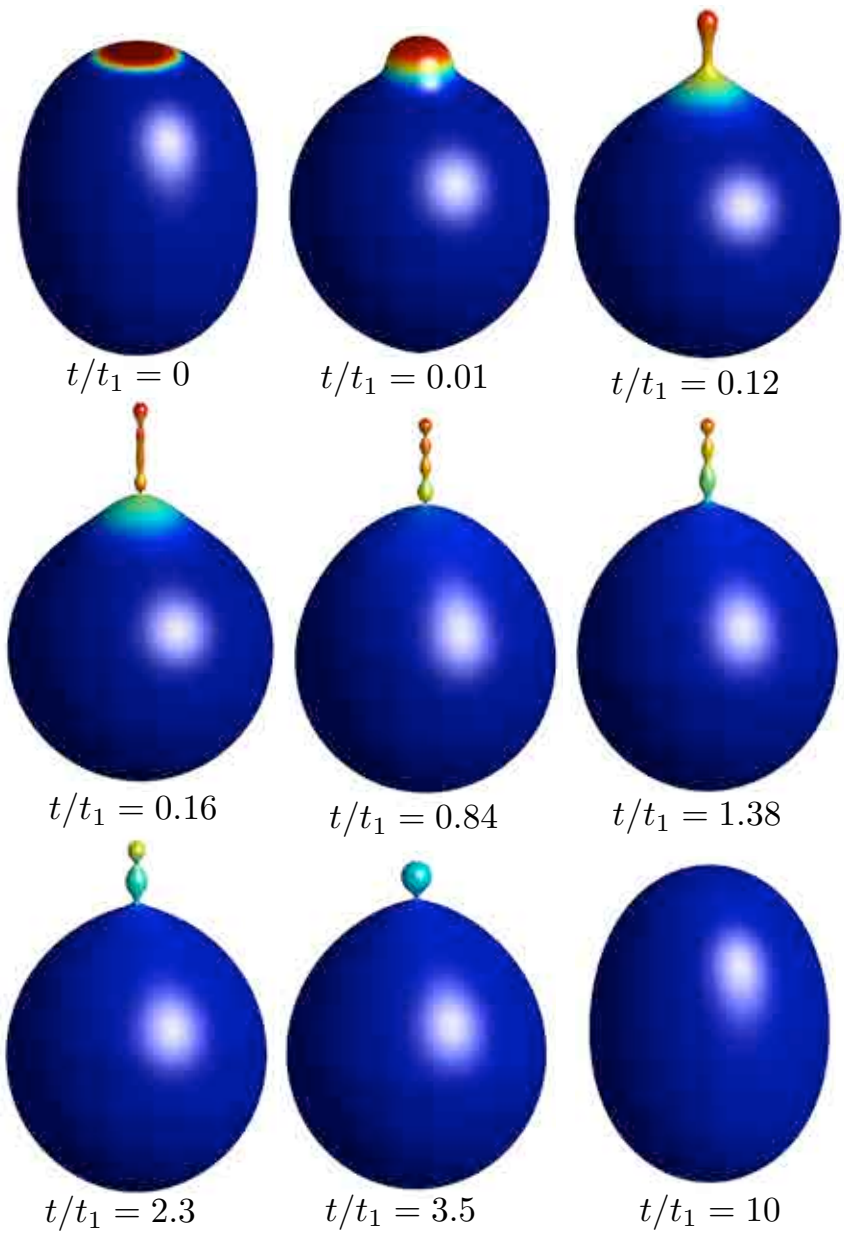

Figure 4.9: (Color online) Relaxation dynamics of the giant vesicle ($R = 4$ µm, $t_1 = 98$ ms, $t_2 = 0.88$ ms). The density difference relaxation by inter-monolayer slippage is slowed down significantly by the dramatic shape changes, which transiently trap the density asymmetries. At a later time ($t/t_1 \approx 10$) not shown here, the spherical bud is absorbed by the mother vesicle. The color maps represent the difference between the monolayer lipid densities at the neutral surface, $\hat{\rho}^+ - \hat{\rho}^-$, where red corresponds to $\delta\rho$ and blue to 0.

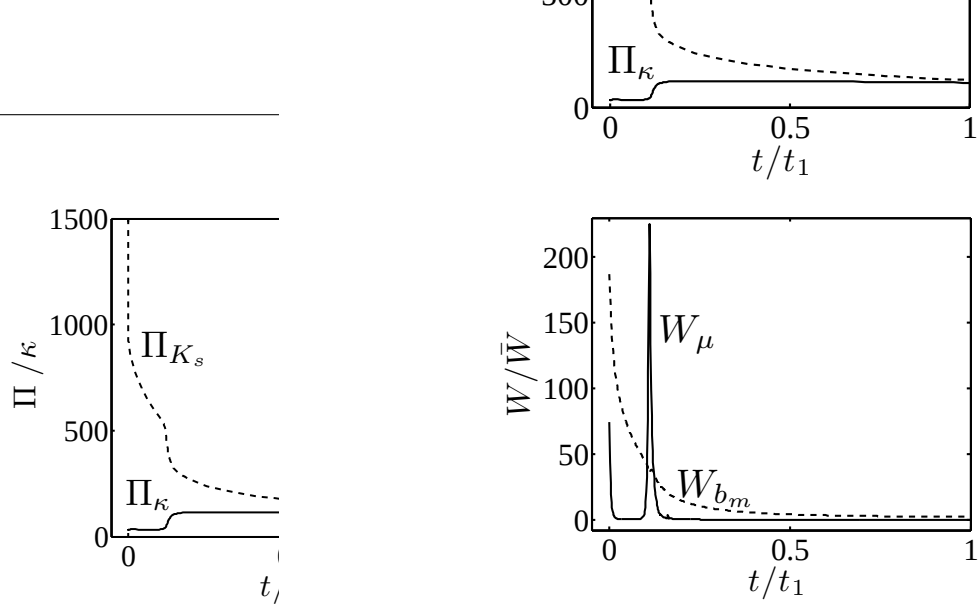

Figure 4.10: Elastic energy (top) and dissipation power (bottom) during the relaxation of the giant vesicle, $R = 4$ μm. The dissipation power is normalized by $\bar{W} = \bar{S} b_m d^2/(\hat{\rho} t_1^2)$. After a fast initial relaxation of the density difference by budding, which leaves as a signature a first spike in the membrane shear dissipation, the dynamics are dictated by the inter-monolayer friction. Yet, at $t \approx 0.12\ t_1$, the density difference field is such that a rapid shape transition from a bud to an elongated protrusion occurs, leaving another large spike of membrane shear dissipation.

Such density perturbation creates a gradient of both density average and density difference of magnitude $\delta\rho/2$ [Seifert, 1997]. The density average disturbance relaxes, dragged by membrane shear viscosity, extremely fast in a time scale commensurate to t_4. This initial event needs to be captured by the simulations, although we do not report on it. Then, the density difference disturbance relaxes by local curvature. Such a localized shape change is dragged mainly by membrane shear viscosity in a time scale given by t_2. The amplitude and nature of this moderately fast relaxation emerges as a competition between bending and the stretching elasticity, and is strongly size dependent. The shape changes caused by density difference gradients are barely noticeable for density disturbances smaller than $\ell = \kappa/(K_s d\hat{\rho}) \approx 80$ nm, when curvature elasticity exerts strong forces opposing deformation. Then, in a slower process dictated by t_1, the density difference is dissipated through inter-monolayer slip. During this process, the shape disturbance adapts very quickly to the diffusing density difference, and eventually disappears.

Figures 4.7-4.9 show the shape and density evolution of perturbed prolate vesicles of different radii as they relax towards a new equilibrium state. For the small

vesicle, Fig. 4.7, the density deviations hardly produce any shape deformation due to the large resistance of bending elasticity relative to stretching elasticity as the size of the disturbance is smaller than ℓ. The aggregated density diffuses in the lateral direction dragged by inter-monolayer slippage. The time scale for density diffusion is $t_1 = \bar{S} b_m / K_s \approx 0.06$ ms, where $\bar{S} = 2\pi \left(1 - \cos w\phi\right) R^2$ is the area of the asymmetry patch. The small shape perturbation occurs at a faster time scale given by $t_2 \approx 0.36\, t_1$. For the large vesicle, Fig. 4.8, the resisting elastic forces due to curvature are much less relevant, and in a very fast time scale commensurate to $t_2 \approx 2 \cdot 10^{-2}\ t_1$, a geometric feature of significant amplitude relaxes part of the stretching elastic energy. Due to the time scale separation, the shape adapts almost instantaneously to equilibrate stretching and curvature forces as the density slowly relaxes by inter-monolayer friction. The transient bud eventually disappears as the density fully equilibrates. A similar behavior can be observed for the giant vesicle, Fig. 4.9, where now the dynamics are complicated by a richer shape landscape at the current ratio between the disturbance size and ℓ. As before, in the very initial stages given by t_2, a large amplitude bud forms at the density disturbance. As the density diffuses, there is a shape transition by which the bud elongates into a short tube at $t \approx 0.12\ t_1$. This fast shape transition relaxes abruptly the stretching energy and slightly increases the curvature energy, resulting in a net decrease of the total energy. This abrupt shape change is accompanied by a spike in the membrane shear viscosity (see Fig. 4.10). This figure also shows the initial spike in membrane dissipation associated with t_2.

Subsequently, the elongated protrusion pearls, and the number of pearls decreases in steps until there is a single vesicle connected to the mother vesicle by a narrow neck. The color map in Fig. 4.9 shows how the density difference is quantized by the size of the pearls. Interestingly, these complex shapes transiently trap the density asymmetries, and slow down significantly the density relaxation by inter-monolayer slip. The full relaxation takes $t \approx 10\ t_1$. This example shows the intimate coupling between lipid flow and shape dynamics. Previous insightful theoretical work [Sens, 2004] captures the essential physics, but is restricted to a shape ansatz that does not agree with the shapes we find and that are reported in some experiments.

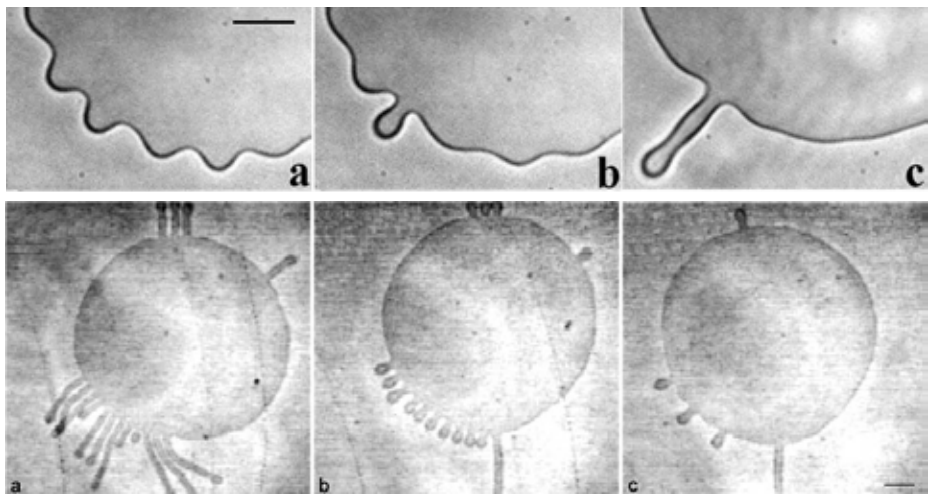

Figure 4.11: Experimental observations by [Tsafrir et al., 2003]; tube and bud formation after a local injection of polymers in the vicinity of a flaccid giant vesicle. The first row shows the nucleation of buds and their transient elongation into tubes. The second row shows further elongation and the subsequent retraction of the bud-tube shapes

Similar phenomena have been observed experimentally, for instance by locally anchoring polymers or amphiphilic molecules to oblate lipid vesicles [Tsafrir et al., 2003]. Once polymers anchor to the bilayer, they induce curvature both by increasing the area of the monolayer, and by a local deformation of the bilayer (spontaneous curvature), the anchoring molecules diffuse on the membrane. Figure 4.11 shows the experimental observations from [Tsafrir et al., 2003], which are qualitatively in agreement with our simulations. Similarly, a localized pH gradient can change the repulsion between the lipid head-groups of the exposed monolayer and form the metastable pearled tubes [Fournier et al., 2009, Khalifat et al., 2008]. Such asymmetries have been modeled mathematically by considering a transient spontaneous curvature [Campelo and Hernandez-Machado, 2008], an area difference [Khalifat et al., 2008], or a density asymmetry parameter [Fournier et al., 2009].

Stomatocyte morphologies are often observed in vesicles at equilibrium, and have been explained on the basis of area difference or spontaneous curvature [Svetina, 2009]. However, the dynamical studies of the stomatocyte formation are limited. The

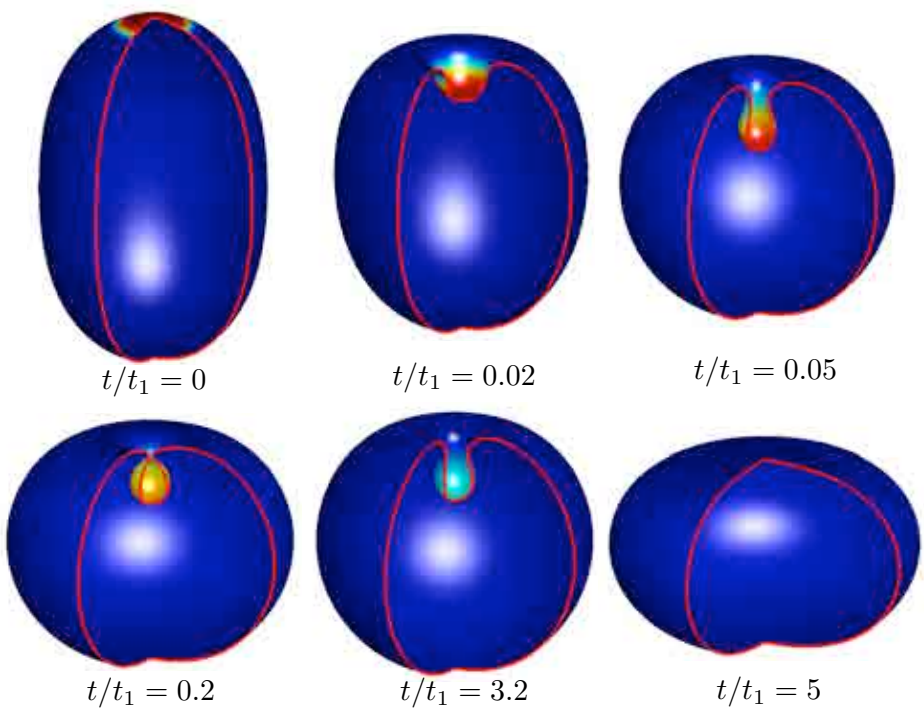

Figure 4.12: (Color online) Stomatocyte formation from a large vesicle of radius $R = 2$ µm, locally perturbed by an inverse density asymmetry. During the relaxation of the density disturbance, the vesicle switches from a prolate to an oblate

reversible dynamics of membrane invaginations has been studied by a local acid injection [Khalifat et al., 2008]. Going back to Fig. 4.5, we explore the transient formation of stomatocytes by removing lipids locally from the outer leaflet. We consider a large vesicle $R = 2$ µm, with a density disturbance characterized by $\delta\rho = -0.05\ \rho_0$ and $w = 10\%$. Figure 4.12 shows the stomatocyte formation by relaxation of density difference through shape changes at a time scale t_2, and then the full relaxation through inter-monolayer slippage at a time scale slightly longer than t_1. Again, the second stage of the relaxation dynamics is slowed down by the complex shapes adopted by the vesicle. Interestingly, these dynamics provide a pathway between two meta-stable branches of the equilibrium phase diagram, prolates and oblates.

We finally note that our results quantitatively depend on the reduced volume, the magnitude of the density disturbance, and its size relative to the vesicle size. A systematic characterization of the dynamical behavior of such density disturbances is the topic of current work. In the present study, we have not considered larger vesicles since then, the effect of the bulk fluid viscosity, ignored here for simplicity, may become important.

4.6 Summary

After validating the model with the well-understood membrane tethering, we have presented a gallery of examples, which highlight the versatility and generality of the model in describing very different processes involving lipid hydrodynamics and shape dynamics. These examples show that some usual assumptions can oversimplify the response of bilayers to various stimuli, and illustrate a wide diversity of dynamical regimes. In tether pulling, the viscoelastic behavior is given by the bending elasticity and the inter-monolayer friction. In the inter-cell communication through tunneling tubes, membrane tension gradients, together with inter-monolayer friction and membrane shear viscosity, set the time scale of transport. In the relaxation dynamics of a bud absorption into a planar bilayer, two time scales are operative: the faster one, given by bending elasticity and the membrane shear viscosity, attenuates the

geometry of the bud, while the slower one, given by stretching elasticity and intermonolayer friction, relaxes a residual density difference between the monolayers. This latter time scale is the dominant one in the relaxation of localized asymmetric density disturbances in vesicles, which also possess a faster time scale given by stretching elasticity and membrane shear viscosity. It is important to note that these observations are specific to our parameter choice (material parameters such as α, size, applied tension,...), and in general the dynamics depend very much on the details. Furthermore, our simulations illustrate the highly nontrivial effect of the bilayer shape on the dynamics. We conclude that the proposed model and simulation method is a valuable tool to interpret experiments and interrogate hypothesis about biological phenomena mediated by bilayers.

Chapter 5

Protrusions from confined bilayers stabilized by stress and pressure

---

Membrane protrusions are ubiquitous in cells; some of them are driven by molecular motors or actin polymerization; others are scaffolded into specialized proteins. In this chapter, we examine another mechanism, by which stressed membranes delaminate from their adjacent confining structures. For example, cell blebs delaminate from the contracting cortex [Charras and Paluch, 2008]; vacuole-like dilations (VLDs) invaginate in shrinking cells adhered to substrates [Morris and Homann, 179]. Blebs and VLDs play a role in cell motility [Charras and Paluch, 2008], pressure equilibration [Charras et al., 2005], apoptosis, and area homeostasis [Morris and Homann, 179, Charras and Paluch, 2008]. Recently, similar protrusions have been observed in confined model membrane systems, such as supported bilayers or lipogel particles [Staykova et al., 2011, Saleem et al., 2011]. These findings suggest that the mechanisms behind protrusions in confined membranes may not be cell-specific, but rather determined by the mechanics of confinement, which we investigate here with experiments, theory and simulations.

Recently, an experiment was developed that subjects a supported lipid bilayer (SLB) to lateral strain by deforming (inflating or deflating) the PDMS substrate underneath the membrane with an externally applied pressure [Staykova et al., 2011]. For the experiments reported here, we integrate this system in a microfluidic channel

to control the osmolarity of the solution above the membrane and thus modify the volume of interstitial fluid between the bilayer and the substrate (Fig. 5.1a). Our observations show that supported planar membranes readily form out-of-plane protrusions, tubular or spherical whose morphology can be controlled by the magnitude and the rate of the applied strain, and the volume of interstitial fluid. These transformations are passive, occur under conditions common for cells, and may suggest a generic, non-motor or scaffold-driven route for the regulation of the physiology of confined cells or membrane-bound organelles.

We develop a theoretical model for the confined bilayer in equilibrium and rationalize the observations in terms of this model. We show that our quasi-static model can explain the morphology of protrusions, tubular or spherical, in terms of a strain-volume (ε_C, v) phase diagram. We validate the equilibrium model by comparing the results with simulations. Furthermore, in our experiments, we observe more complex membrane morphologies such as tube-sphere complexes and branched tube-discocyte, which cannot be explained by our equilibrium model. We understand these observations by the dynamical effects associated with the rate of the strain, and investigate them by our axisymmetric simulations allowing for general shapes and lipid density distributions.

5.1 Experimental setup

For the experiments, we construct a channel between a glass cover slip and a PDMS slab, and we coat it with a uniform lipid bilayer composed of 1,2-dioleoyl-sn-glycero-3-phosphocholine (DOPC) and fluorescently labeled with 1 mol% 1,2-dipalmitoyl-sn-glycero-3-phosphoethanolamine-N-(lissamine rhodamine B sulfonyl) (ammonium salt) (Rh-DPPE) (see procedure in [Staykova et al., 2011]). The PDMS slab contains an additional cylindrical puncture (1 mm in diameter) between the inlet and outlet, which is covered by a thin PDMS sheet (about 100 μm thick), and connected at the other end to a microsyringe pump (Fig. 5.1a). Initially, both the solution in the channel, and the few nanometer thick interstitial liquid film, which separates the membrane

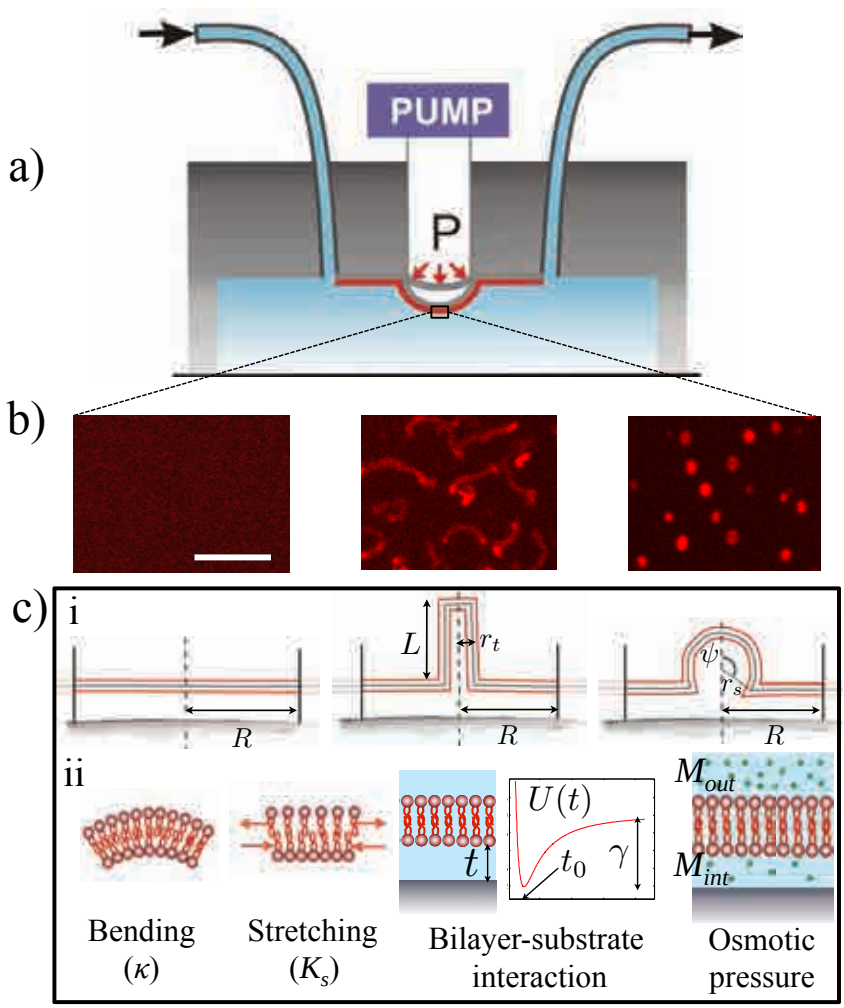

Figure 5.1: (a) Experimental setup to investigate the effects of strain and osmotic pressure on a supported lipid bilayer. It is observed experimentally (b) (confocal images) and shown by model theoretically three membrane morphologies (c-i) a planar disc of uniform membrane with radius R; a planar membrane with a tubular protrusion (radius r_t, length L); and with a spherical protrusion (radius r_s, contact angle ψ). Scale-bar: 5 μm. (c-ii) Contributions to the free energy of the system and corresponding material properties.

from the substrate [Swain and Andelman, 2001] are at the osmolarity at which the bilayer is prepared ($M_0 = 0.3$ Osm). Using this original setup, we can 1) subject a supported lipid membrane to a lateral strain by deforming (inflating or deflating) the PDMS sheet underneath the membrane Staykova et al. [2011], and 2) modify the volume of interstitial liquid by controlling the osmolarity of the solution above the membrane.

Our confocal observations reveal that single-component, supported bilayers in the fluid phase exhibit different morphologies –a uniform state, or states with tubular or spherical lipid protrusions, which can be controlled reversibly by the magnitude of the applied strain and the interstitial volume, and are nearly uniformly spaced (Fig. 5.1b). Since we cannot control the nucleation sites of the protrusions in the current setup and, therefore, the distance between them, we cannot expect a full quantitative agreement between the experiment and the theory. For instance, the shape transitions in the experiments do not occur in perfect synchrony for all protrusions, and their size may slightly vary depending on the density of the protrusions. Note that the distance between the protrusions is determined presumably by the friction between the bilayer and the substrate and by a lower membrane adhesion at preexisting irregularities on the PDMS surface.

Moreover, we will demonstrate that highly curved tubules protruding from confined bilayers remain stable, even without the assistance of commonly appreciated mechanisms, such as localized forces [Derényi et al., 2007] or spontaneous curvature [Lipowsky, 2013].

5.2 Equilibrium theoretical model

To understand the experimental observations, we develop a theoretical model for the confined bilayer in equilibrium. We idealize the membrane as a collection of juxtaposed cells with one protrusion at the center of each, which allows us to focus on a single cell of radius R_0 commensurate to half of the average distance between protrusions. We define a reference volume $V_0 = A_0 t_0$, where $A_0 = \pi R_0^2$ is the relaxed

area of the patch of bilayer, and t_0 the equilibrium separation with the substrate. We define a reduced volume as

$$v = \frac{V}{V_0}, \tag{5.1}$$

which is a relative measure of the amount of water in the interstitial space. The radius of the initial disk R_0 can be understood as a measure of the protrusion density in the confined supported bilayer, while R measures the compressive strain

$$\varepsilon_c = \frac{\Delta S}{S_0} = 1 - \left(\frac{R}{R_0}\right)^2. \tag{5.2}$$

In this model, the bilayer adopts the state of lowest free energy amongst three predefined families of shapes, planar, tubular or spherical (Fig. 5.1c), consistent with our experimental observations and with simulations allowing for general shapes and density distributions (see later). For each family, the equilibrium state is given by minimizing the free energy, i.e. $\int f \, dA$, where

$$f = \frac{K_s}{2}\left(\phi^{+2} + \phi^{-2}\right) + \frac{\kappa}{2}(2H)^2 + U(t). \tag{5.3}$$

The above free energy includes the stretching and bending elasticity, and poorly characterized bilayer-substrate interaction potential $U(t)$, as a function of the separation t (Fig. 5.1d). The competition between the energy terms is arbitrated by the substrate area, relative to a fixed number of lipids, and by the volume enclosed between the membrane and the substrate.

5.2.1 Substrate-bilayer interaction energy

The interaction potential with the substrate is far from being understood, although it is known to depend on pH, the surface chemistry, the lipid composition and the surface roughness. Reported values for the adhesion energy γ vary by orders of magnitude, ranging from $5 \cdot 10^{-6}$ J/m^2 between bilayers (Swain and Andelman [2001]), to $3.5 \cdot 10^{-3}$ J/m^2 for mica (Schönherr et al. [2004]), and $2.5 \cdot 10^{-3}$ J/m^2 for glass (Ursell et al.

[2011]). We follow the functional form proposed by Swain and Andelman [2001], We follow the functional form proposed by Swain and Andelman [2001]

$$U(t) = -\frac{A_0}{12\pi}\left[\left(\frac{1}{t}\right)^2 - \left(\frac{1}{t+\delta}\right)^2\right] + be^{-\alpha t}, \tag{5.4}$$

and scale the energy units in the potential parameters to achieve the desired adhesion energy while maintaining the equilibrium separation $t_0 \approx 3$ nm and the dissociation separation $t_d \approx 3.5$ nm of the original potential.

As discussed we discuss later, we adopt $\gamma = 2 \cdot 10^{-3}$ J/m^2. Across a large part of the phase diagram, the bilayer departs very little from the potential well in the adhered parts of the membrane, and the bilayer-substrate interaction can be modeled with a hard potential and the surface energy. However, for strongly deflated tubes or for uniformly adhered bilayers, we find that the adhesion stiffness enters the energy competition.

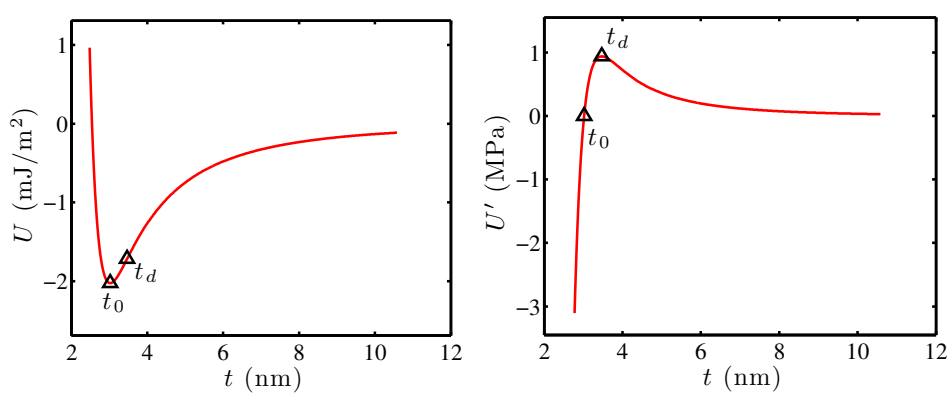

Figure 5.2: Adhesion potential and its first derivative considered here. We highlight the equilibrium separation t_0 and the dissociation separation characterized by $U''(t_d) = 0$.

5.2.2 Planar state

In the absence of bifurcations, the system behaves uniformly under compression. The interstitial volume is $V = \pi R^2 t$, and therefore

$$t = \frac{V}{\pi R^2}. \tag{5.5}$$

The balance of mass in each leaflet (labelled as + and −) is expressed as,

$$\pi R_0^2 \rho_0 = \pi R^2 \hat{\rho}^{\pm}. \tag{5.6}$$

Introducing the reduced density deviations

$$\phi^{\pm} = \frac{\hat{\rho}^{\pm}}{\rho_0} - 1, \tag{5.7}$$

this results in

$$\phi^{\pm} = (R_0/R)^2 - 1. \tag{5.8}$$

The energy of the system can then be computed as

$$E_{uniform} = \pi R^2 \left[\frac{K_s}{2} \phi^{\pm 2} + \mathcal{V}(t) \right]. \tag{5.9}$$

We find that the planar adhered configuration is never the state of lowest energy for $\varepsilon_C > 0$ and $v > 1$, yet it is experimentally observed for small ε_C and v. This fact, together with our numerical simulations, suggests that the planar state is metastable in a region whose boundary can be estimated by linear stability analysis. We perform in appendix C.1 a linear stability analysis of the uniformly compressed supported bilayer. This analysis acknowledges the destabilizing effect of the incompressibility constraint, which upon compression of the bilayer, pushes the bilayer towards the point of instability of the membrane-substrate potential. It allows us to estimate if the planar state is marginally stable, even if a protruded state is thermodynamically

favorable. Even if this is the case, the system may have to cross an energy barrier significantly higher than the agitation of the system to buckle, and therefore the planar state would be observed. The linearized buckling analysis may provide an overestimation of the stability of the planar configuration, if the destabilizing imperfections in the system are important, or an underestimation for example if there are pinning points in SLB.

5.2.3 Protruding tube

We consider now the energetics of an idealized tube of radius r and length L forming at the center of the compressed disk. Inspired by the simulations, we assume the radius of the tube is uniform. We also show later by simulations (see Fig. 5.9) that the lipid density in each leaflet is uniform as well (even between the adhered and the tube regions). Therefore, the configuration of the system is given by r, L, $\phi^{\pm}$ and t. The volume constraint reads

$$V = \pi R^2 t + \pi (r - 2d)^2 L. \tag{5.10}$$

The conservation of mass within each leaflet reads

$$\left[\pi R^2 + 2\pi (r \pm d) L\right] (\phi^{\pm} + 1) = S_0. \tag{5.11}$$

It is important here to perturb the radius by $\pm d$ to retain the area difference effect. Ignoring the curvature energy of the neck and cap regions of the tube, the energy of the system is

$$E_{tube} = \pi \left[K_s \phi^{\pm 2} \left(\frac{R^2}{2} + rL \right) + \frac{\kappa L}{r} + R^2 \mathcal{V}(t) \right]. \tag{5.12}$$

To better account for the energy of shallow and wide protrusions, for which the assumption $r \ll R$ may be inaccurate, we rather write

$$E_{tube} = \pi \left[K_s \phi^{\pm 2} \left(\frac{R^2}{2} + rL \right) + \frac{\kappa L}{r} + (R^2 - r^2)\mathcal{V}(t) + r^2 \mathcal{V}(L+t) \right] \tag{5.13}$$

The equilibrium shapes result from minimizing the energy subject to the mass and volume constraints. We introduce the Lagrangian

$$\begin{aligned} \mathcal{L}\left(\phi^{\pm}, r, L, t, \sigma^{\pm}, p\right) &= \pi \left[K_s \phi^{\pm 2} \left(\frac{R^2}{2} + rL \right) + \frac{\kappa L}{r} + (R^2 - r^2)\mathcal{V}(t) + r^2 \mathcal{V}(L+t) \right] \\ &\quad - p \left[\pi R^2 t + \pi (r - 2d)^2 L - V \right] \\ &\quad + \sigma^{\pm} \left\{ \left[\pi R^2 + 2\pi (r \pm d) L \right] (\phi^{\pm} + 1) - S_0 \right\} \end{aligned} \tag{5.14}$$

where the tension in each leaflet $\sigma^{\pm}$ (positive in tension, negative in compression) and the pressure difference between the interstitial and the bulk media p appear as Lagrange multipliers for the constraints. The first order optimality conditions are found by making stationary the Lagrangian. Besides the constraints in Eqs. (5.10,5.11), we obtain

$$0 = \frac{\partial \mathcal{L}}{\partial \phi^{\pm}} = 2\pi K_s \phi^{\pm} \left(\frac{R^2}{2} + rL \right) + \sigma^{\pm} \left[\pi R^2 + 2\pi (r \pm d) L \right], \tag{5.15}$$

$$\begin{aligned} 0 &= \frac{\partial \mathcal{L}}{\partial r} \\ &= \pi L K_s \phi^{\pm 2} - \frac{\pi \kappa L}{r^2} + 2\pi r \left[\mathcal{V}(L+t) - \mathcal{V}(t) \right] - 2\pi p L (r - 2d) + 2\pi L \sigma^{\pm} (\phi^{\pm} + 1), \end{aligned} \tag{5.16}$$

$$0 = \frac{\partial \mathcal{L}}{\partial L} = \pi r K_s \phi^{\pm 2} + \frac{\pi \kappa}{r} - \pi p (r - 2d)^2 + 2\pi (r \pm d) \sigma^{\pm} (\phi^{\pm} + 1), \tag{5.17}$$

$$0 = \frac{\partial \mathcal{L}}{\partial t} = \pi (R^2 - r^2) \frac{\partial \mathcal{V}}{\partial t}(t) + \pi r^2 \frac{\partial \mathcal{V}}{\partial t}(L+t) - \pi R^2 p. \tag{5.18}$$

From the first and the last of these equations, we obtain the expected results

$$\sigma^{\pm} = -\frac{R^2 + 2rL}{R^2 + 2(r \pm d)L} \, K_s \phi^{\pm} \approx -K_s \phi^{\pm} \tag{5.19}$$

and

$$p = \frac{R^2 - r^2}{R^2}\ \frac{\partial \mathcal{V}}{\partial t}(t) + \frac{r^2}{R^2}\frac{\partial \mathcal{V}}{\partial t}(L+t) \approx \frac{\partial \mathcal{V}}{\partial t}(t). \tag{5.20}$$

Despite the simplicity of the model, it is not possible to solve it analytically, and we rather resort to numerical optimization. For this purpose, it is convenient to eliminate some variables using the constraints:

$$t(r, L) = \frac{V - \pi(r - 2d)^2 L}{\pi R^2}, \tag{5.21}$$

and

$$\phi^{\pm}(r, L) = \frac{R_0^2}{R^2 + 2(r \pm d)L} - 1. \tag{5.22}$$

Replacing back into the energy of the system, we obtain

$$E_{tube}(r, L) = \pi \left\{ K_s[\phi^{\pm}(r, L)]^2 \left(\frac{R^2}{2} + rL \right) + \frac{\kappa L}{r} + (R^2 - r^2)\mathcal{V}(t(r, L)) + r^2 \mathcal{V}(L + t(r, L)) \right\}, \tag{5.23}$$

which is numerically minimized. We do not allow for short and wide tubes, since the energy above is not a good estimate for shallow and wide protrusions. In the minimization, we include the constraints

$$L \geq 4r, \quad r \geq 0. \tag{5.24}$$

The leaflet densities and tensions, the bilayer-substrate separation, and the pressure difference between the interstitial and the bulk media can be recovered with the equations above.

5.2.4 Protruding spherical cap/bud

We consider now a protruding spherical cap, forming a circular neck in its intersection with the adhered planar bilayer. Its shape is parameterized by the radius of the sphere r measured from its center to the mid plane of the bilayer, and by the angle ψ that

segment joining the center of the sphere and a point in the neck forms with a line perpendicular to the substrate and passing through the center of the sphere. The radius of the neck, the area of the cap, and its enclosed volume can be computed as

$$r_{neck} = r \sin\psi, \tag{5.25}$$

$$A_{cap} = 2\pi(1 - \cos\psi)r^2, \tag{5.26}$$

and

$$V_{cap} = \frac{\pi}{3}(2 - 3\cos\psi + \cos^3\psi)(r - 2d)^3. \tag{5.27}$$

Following the same steps as before, we have as constraints:

$$V = \pi R^2 t + \frac{\pi}{3}(2 - 3\cos\psi + \cos^3\psi)(r - 2d)^3, \tag{5.28}$$

and

$$\left[\pi(R^2 - r^2\sin^2\psi) + 2\pi(1 - \cos\psi)(r \pm d)^2\right](\phi^{\pm} + 1) = S_0. \tag{5.29}$$

Ignoring the curvature energy of the neck, the energy of this configuration is

$$\begin{aligned} E_{sphere} &= \pi\Bigg\{K_s\phi^{\pm 2}\left[\frac{R^2 - r^2\sin^2\psi}{2} + (1 - \cos\psi)r^2\right] && (5.30)\\ &\quad +4(1 - \cos\psi)\kappa + (R^2 - r^2\sin^2\psi)\mathcal{V}(t)\Bigg\}. && (5.31)\end{aligned}$$

As before, we find,

$$\sigma^{\pm} = -\frac{R^2 - r^2\sin^2\psi + 2(1 - \cos\psi)r^2}{R^2 - r^2\sin^2\psi + 2(1 - \cos\psi)(r \pm d)^2}K_s\phi^{\pm} \approx -K_s\phi^{\pm} \tag{5.32}$$

and

$$p = \frac{R^2 - r^2\sin^2\psi}{R^2}\frac{\partial\mathcal{V}}{\partial t}(t) \approx \frac{\partial\mathcal{V}}{\partial t}(t). \tag{5.33}$$

Eliminating unknowns using the constraints, we obtain

$$t(r,\psi) = \frac{V - \pi/3(2 - 3\cos\psi + \cos^3\psi)(r - 2d)^3}{\pi R^2}, \tag{5.34}$$

and

$$\phi^{\pm}(r,\psi) = \frac{R_0^2}{(R^2 - r^2\sin^2\psi) + 2(1-\cos\psi)(r \pm d)^2} - 1. \tag{5.35}$$

Replacing back into the energy of the system, we obtain

$$\begin{aligned} E_{sphere}(r,\psi) &= \pi\Bigg\{ K_s\left[\phi^{\pm}(r,\psi)\right]^2\left[\frac{R^2 - r^2\sin^2\psi}{2} + (1-\cos\psi)r^2\right] & (5.36)\\ &\quad +4(1-\cos\psi)\kappa + (R^2 - r^2\sin^2\psi)\mathcal{V}(t(r,\psi))\Bigg\}. & (5.37) \end{aligned}$$

which is numerically minimized subject to the constraints

$$0 \le \psi \le \pi, \quad r \ge 0. \tag{5.38}$$

To interpret the result, we define the apparent radius, which would be observed by looking perpendicularly at the compressed bilayer with a spherical cap protrusion:

$$r_{app} = \begin{cases} r & \text{if } \psi \ge \pi/2 \\ r_{neck} & \text{if } \psi < \pi/2 \end{cases} \tag{5.39}$$

In many situations of interest, the model for the spherical cap protrusions can be significantly simplified. As we shall see later, for relatively large caps the area difference effect and the curvature energy can be neglected. In addition to this, the bilayer departs very little from the equilibrium position, and the adhesion may be incorporated simply with an adhesion energy $\gamma = -\mathcal{V}(t_0)$. The model then reduces

to minimizing

$$E_{sphere} = \pi \left\{ K_s \phi^2 \left[R^2 - r^2 \sin^2 \psi + 2(1 - \cos \psi) r^2 \right] - (R^2 - r^2 \sin^2 \psi) \gamma \right\}. \quad (5.40)$$

subject to

$$V = \pi R^2 t + \frac{\pi}{3}(2 - 3\cos \psi + \cos^3 \psi) r^3, \quad (5.41)$$

and

$$\left[\pi(R^2 - r^2 \sin^2 \psi) + 2\pi(1 - \cos \psi) r^2 \right] (\phi + 1) = S_0. \quad (5.42)$$

5.3 Results

5.3.1 Phase diagram $\varepsilon_c - v$

We organize our experimental and theoretical observations on the membrane morphologies in a strain-volume (ε_C, v) phase diagram (Fig. 5.3), which depends also on the separation R between the protrusions. For small ε_C and v the lipid membrane is in a planar, adhered configuration (black region).

For reduced volumes smaller than one (not shown here), the uniformly compressed state is initially preferred, but very soon, at small compressive strains, tubes become more stable. The mere global energy minimization underlying these phase diagrams does not provide accurate information on the nucleation of a protrusion out of an initially uniformly compressed bilayer. The region in which the applied strain is smaller than the critical buckling strain is also shown in the diagram. This additional information explains the larger range of relative stability of uniformly compressed supported bilayers observed in experiments. For sufficiently large reduced volumes, the uniformly compressed states are not even marginally stable for any compressive strain, and shallow spherical caps are predicted instead at low strains.

At $v = 1$, tubes are the energetically preferred morphology for any compressive strain. For larger values of v, spherical caps are initially preferred and after a com-

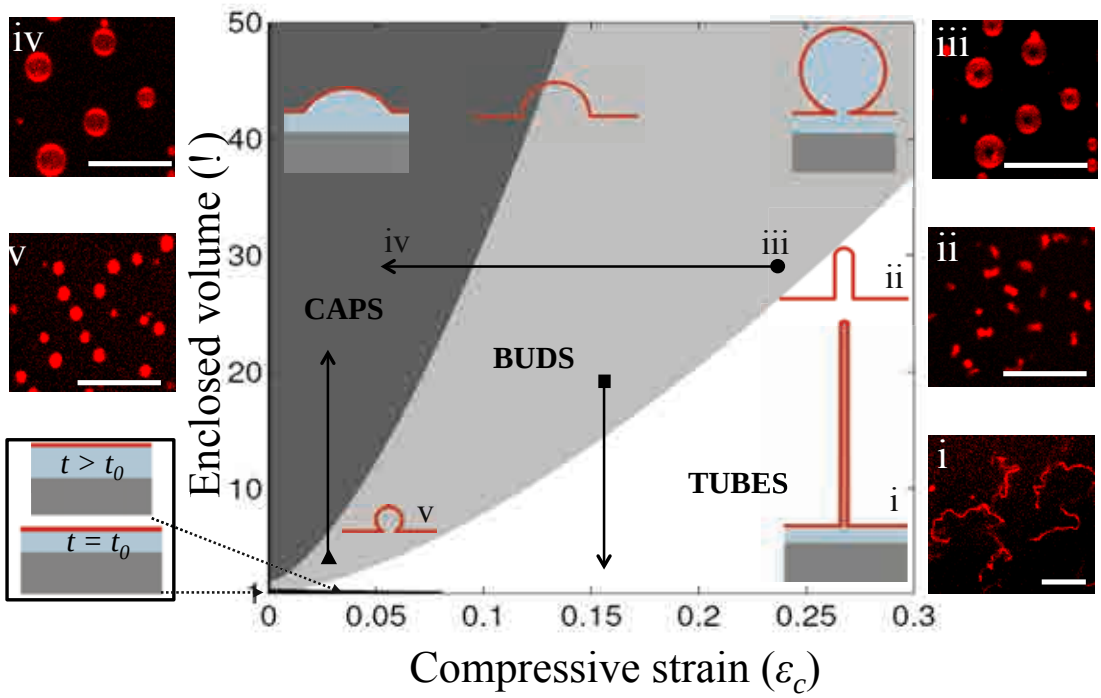

Figure 5.3: Morphological strain-volume phase diagram of confined lipid bilayers. The diagram is derived theoretically for $R_0 = 4$ μm, as measured from the experimental images. We distinguish between a fully adhered planar bilayer (black region), and a bilayer with tubular protrusions, labeled TUBES (white area), or with spherical protrusions, labeled BUDS (light grey) and CAPS (dark grey). Buds ($\pi/2 \leq \psi < \pi$) range between almost full spheres (iii) and half spheres, whereas caps ($\psi < \pi/2$) are shallower spherical protrusions (iv). Buds and caps can be distinguished by the neck opening, which appears as a dark center in the confocal images of the protrusions. The scale bar is 10 μm.

pressive strain which grows with the reduced volume, tubes become preferred. The bud-tube boundary can be estimated as

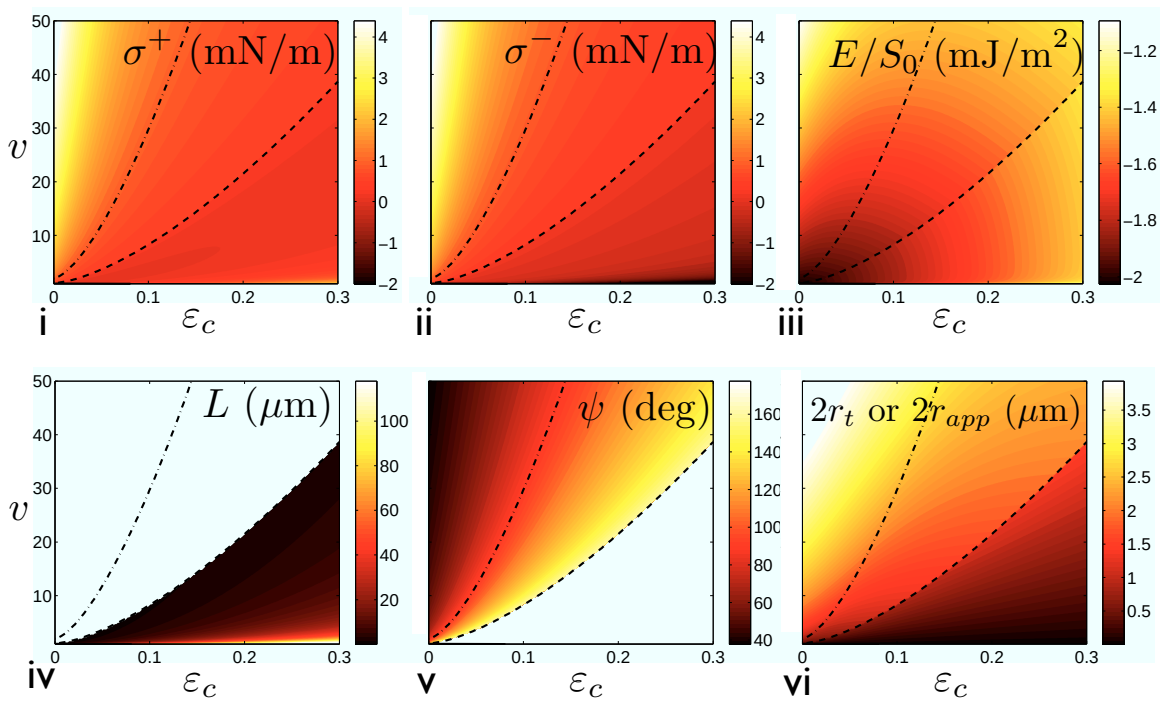

Figure 5.4: Strain-volume phase diagram for $R_0 = 4$ μm; The morphological features of the protrusions (length of the tubes, sphere contact angle, and tube diameter/sphere apparent diameter) are described in panels (iv-vi).

Figure. 5.4 shows the geometric parameters characterizing the protrusion geometry across the diagram. It can be observed that as the compressive strain increases, the tube radius decreases and the tube length increases. Regarding the morphology of the spherical caps, it can be noticed that for a sufficiently large reduced volume and for small strain, very shallow caps with large apparent radius form. As the strain progressively increases, the apparent radius decreases and the angle ψ becomes closer to π, i.e. the spherical caps become nearly full spheres. This happens near the phase boundary with tubes. At this transition, the apparent radius of the spherical cap is significantly larger than the tube radius. This transition is also consistent with the

experimental observations.

5.3.3 Surface stress and pressure

We turn now to the mechanical state of the system, and show how confined bilayers are able to passively regulate stresses, the bilayer tension (σ) and trans-bilayer pressure (Δp_{mech}) by forming out of plane protrusions. Starting from the relaxed system ($\varepsilon_C = 0$ and $v = 1$), the contraction of the substrate squeezes laterally the lipid bilayer and the constrained interstitial liquid film, which becomes thicker because of the incompressibility of water. In addition to the negative bilayer tension, the membrane separates from the substrate ($t > t_0$) and the interstitial pressure substantially increases ($\Delta p_{mech} > 0$). Consequently, the adhered membrane becomes unstable and forms protrusions, through which it relieves the accumulated σ and Δp_{mech} (Fig. 5.5a,b). Due to the adhesion, the bilayer can support high stresses before buckling. For example, at $\varepsilon_C = 0$, the maximum osmotic pressure attainable by complete dilution of the outside solution ($\approx$ 7.5 bar) cannot destabilize the adhered bilayer.

The mechanics of protruded states emerge from the energy competition in different ways across the phase diagram. Except for small volumes or strains, the stress and aspect ratio of the protrusions can be characterized by the volume to area ratio [Miao et al., 1994] applied to the excess quantities, which here yields $6\sqrt{\pi}(V - V_0)/(S - S_0)^{3/2} = (6t_0/R_0)(v - 1)/\varepsilon_C^{3/2}$. For example, around the tube-bud phase boundary, the volume to area ratio is about one, i.e. the protrusions are near spheres with little penalty in their elastic and adhesion energies. If the volume to area ratio is increased, there is a competition between stretching and adhesion and the spherical protrusions become increasingly tense with $\sigma \approx \gamma/(1 - \cos\psi)$. Experimentally, we observe that shallow caps lyse, expelling part of their enclosed volume, and then heal to a state of lower membrane tension (Fig. 5.5c). This observation provides us with an estimate for the adhesion energy of few mJ/m^2, which is consistent with literature reports on bilayer-glass adhesion [Ursell et al., 2011, Reviakine and Brisson, 2000]. If instead the

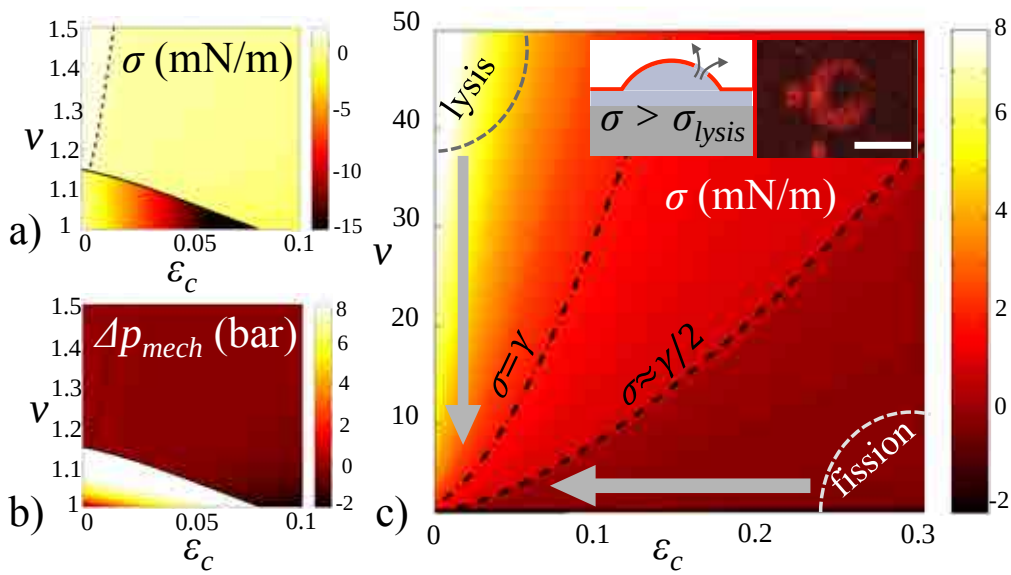

Figure 5.5: Confined bilayers self-regulate stress. Numerical plots of (a) the bilayer tension and (b) the interstitial pressure, as displayed near the planar state of the phase diagram. (c) Numerical plot of the bilayer tension in the protrusions over the entire phase diagram. The regions in the diagram where shallow caps lyse (lysis) and thin tubes detach from the membrane (fission) are shown with contours, whereas the relaxation of the membrane tension accompanying these events is depicted by grey arrows. The inset shows a sketch and a confocal micrograph of the cap lysis; scale bar is 2 µm.

volume becomes scarce, the system accommodates the excess area by forming long thin tubes, where bending, monolayer stretching and substrate repulsion compete. Our simulations show that the tubes have thinner necks at the contact point with the planar bilayer, due to the high adhesion energy. In the thin-tube regime, the Young-Laplace law, which relates pressure difference and tension and is valid for large spherical protrusions, is supplemented by a term of comparable magnitude due to bending elasticity, $\Delta p \approx \sigma/r_t - \kappa/(2r_t^3)$ [Rossier et al., 2003]. Tubes are stabilized by a negative Δp_{mech}, and experience significant negative σ, in contrast to the usual notion of membrane tubes, which are formed by localized forces [Derényi et al., 2007] or by spontaneous curvature [Lipowsky, 2013]. In agreement with experimental observations on thin tube fission [Domanov and Kinnunen, 2006, Bashkirov et al., 2008], we observe that after a strong hyper-osmotic shock (rapid decrease in v), the tubular protrusions collapse and detach at their necks, which reduces the bilayer tension (Fig. 5.5c). According to our model, such tubes reach a small radius of 10 nm and a negative membrane tension of a few mN/m. Thus, the confined membrane is able to further self-regulate its pressure and tension by disrupting the bilayer in the highly stressed protrusions.

5.3.4 Alternative strain-osmolarity phase diagram

When the system is in osmotic equilibrium, the pressure jump across the bilayer is given by

$$\Delta p_{osm} = \bar{R}T \left(\frac{M_0}{v} - M_{out} \right), \tag{5.43}$$

where M_{out} is the chamber osmolarity, considered here as a control parameter, and M_0 is the preparation osmolarity. This relation maps the strain-volume phase diagram to a strain-chamber osmolarity phase diagram, shown in Fig. 5.6. Spherical protrusions occur under hypo-osmotic conditions, and at high strains, only for nearly complete dilution of the chamber fluid. Under hyper-osmotic conditions and for very small strains, the planar conformation is the energetically optimal solution, with reduced volumes smaller than one, see Fig. 5.6(ii). Note that shallow caps at low strain

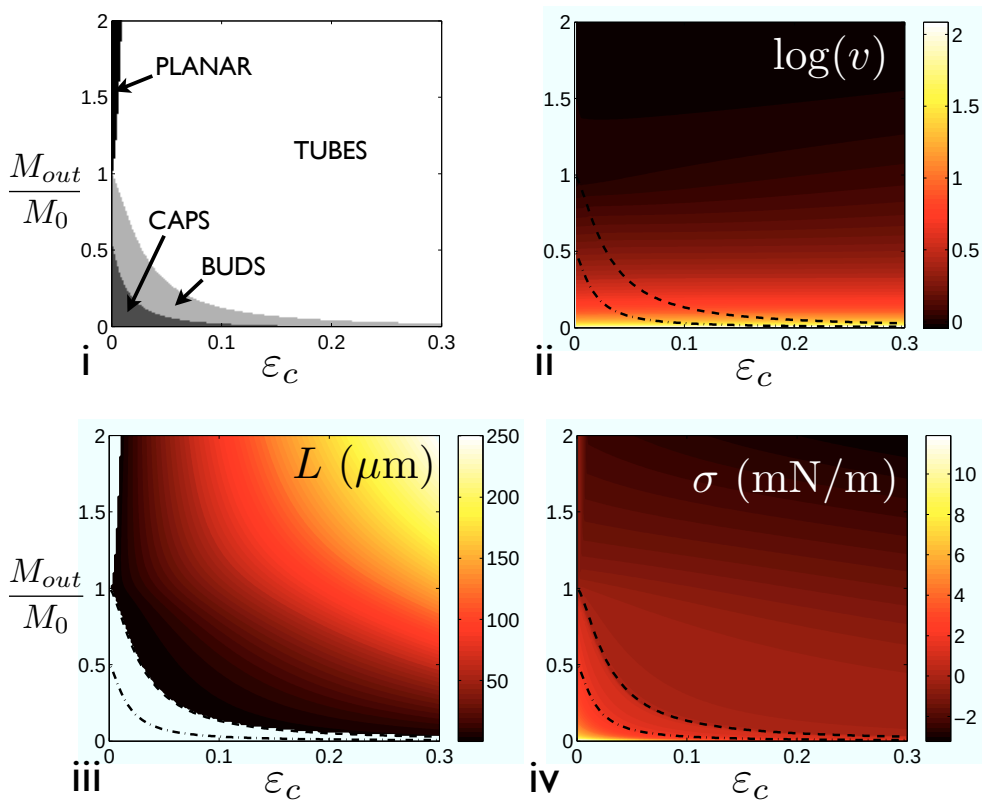

Figure 5.6: Strain-chamber osmolarity phase diagram for $R_0 = 4$ μm (i). Spherical protrusions occur under hypo-osmotic conditions, and at high strains, only for nearly complete dilution of the chamber fluid. Under hyper-osmotic conditions and for very small strains, the planar conformation is the energetically optimal solution, with reduced volumes smaller than one (ii). The rest of the diagram is occupied by tubes, that become longer under increasing strain and osmolar strength (iii). We plot the reduced volume in this phase diagram in logarithmic scale (ii), and note that it ranges from slightly below 1 for strong hyper-osmotic conditions to over 100 for a highly diluted chamber. As noted in Fig. 5.5, shallow caps at low strain and osmolar strength exhibit very high positive tensions, above the lysis tension (iv).

and osmolar strength exhibit very high positive tensions, above the lysis tension, see Fig. 5.6(iv). On the other hand, at high osmolar strength, the tension in thin tubes becomes negative, of significant magnitude, and increasing with strain. In the experiments displaying tube collapse, we subject protrusions to osmotic strengths beyond $M_{out}/M_0 \approx 3$.

5.3.5 Permeation dynamics

Common observations on cells show that the volume in the membrane protrusions changes dynamically due to the semi-permeable nature of the lipid membrane and the porosity of the confining structure. To examine the dynamical effects associated with changing v, we subject the membrane to hypo- (increasing v) or hyper-osmotic (decreasing v) outer solution. The permeation dynamics is generally written as [Olbrich et al., 2000]

$$\dot{V} = P_f V_w S_m \Delta M = \frac{P_f V_w S_m}{\bar{R}T} \Delta p_{osm}, \tag{5.44}$$

where P_f is the osmotic water permeation coefficient, V_w is the volume of a water molecule, S_m is the surface area of semipermeable membrane, and ΔM is the osmolarity jump across the membrane. If, in addition to the osmotic pressure, the membrane is subject to a mechanical pressure difference Δp_{mech}, their difference is the driving force for water permeation until equilibrium is reached, $\Delta p_{mech} = \Delta p_{osm}$. Consequently, for our system, the volume dynamics obey

$$\dot{V} = \frac{P_f V_w S_m}{\bar{R}T} \left[\Delta p_{osm}(v) - \Delta p_{mech}(\varepsilon_c, v)\right]. \tag{5.45}$$

We consider here the interstitial volume dynamics by permeation across the membrane when the system is bought out of equilibrium. This can be achieved either osmotically or mechanically, as a change in strain at constant osmolarity of the chamber changes the mechanical pressure difference, which needs to be balanced by the osmotic pressure difference. We assume that the permeation dynamics is much slower than the characteristic times of all other dissipative mechanisms (the membrane viscosity, the inter-monolayer friction and the friction with the substrate). In agreement with the model predictions, we find experimentally that permeation takes place in tens of seconds to minutes.

In hypo-osmotic conditions, we observe that the apparent diameter of most buds grows monotonically (vertical paths in Fig. 5.3) until an equilibrium plateau (Fig. 5.7a, circles). The buds accommodate their expanding volume (v increases from 3.5 to 22

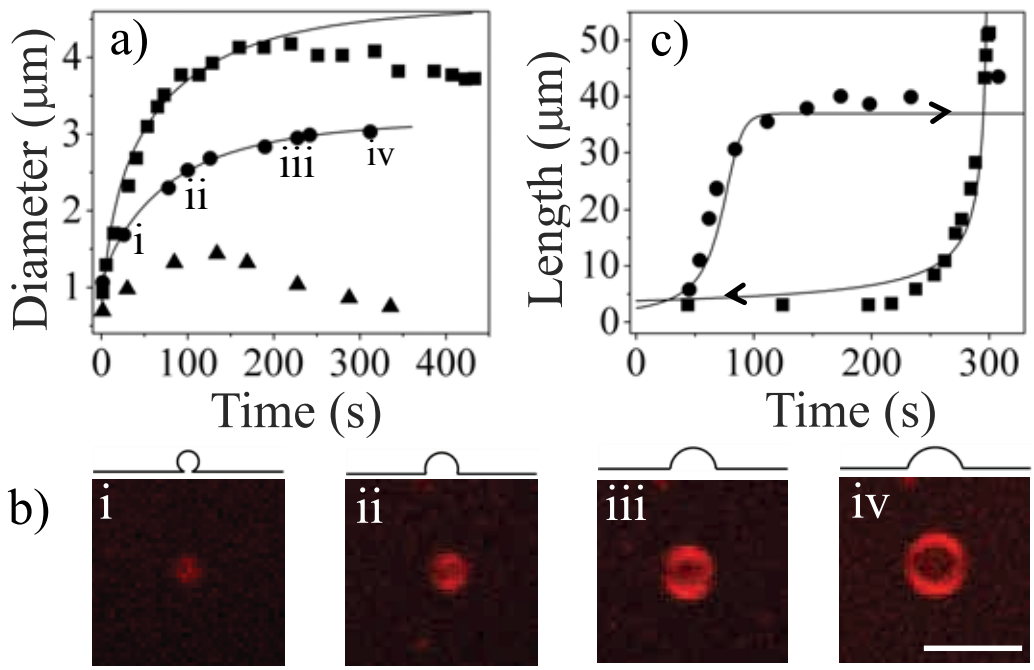

Figure 5.7: Volume dynamics of membrane protrusions upon osmotic changes, determined both experimentally (symbols) and theoretically (lines). (a) Volume dynamics of buds in hypo-osmotic conditions (upon complete dilution of the outer solution): gradual bud inflation up to a plateau (•), partial bud lysis (■), or bud annihilation by coarsening of the protrusion pattern (▲). For the theoretical fits, the initial values for ε_C and v are obtained using the relations shown in Fig. 5.3 and $P_f \approx 45$ μm/s, measured for DOPC in tension [Olbrich et al., 2000]. (b) Snapshots of the gradual bud inflation, visualized by confocal images (scale bar 5 μm) and the corresponding theoretical profiles. (c) Reversible tube transformations, fitted with $P_f \approx 0.75$ µm/s: a gradual bud elongation into a tube (•) in hyper-osmotic conditions (increase in external osmolarity from 0.3 to 0.5 Osm), and a tube to bud retraction (*blacksquare*) upon diluting the outer solution (from 0.6 Osm to water).

according to the model) at fixed excess area by flattening into shallow caps and by further membrane delamination in the neck region (Fig. 5.7a, i-iv), which resembles the dynamics of bleb growth in cells [Charras et al., 2005]. However, as discussed above (Fig. 5.5c), the volume expansion of the buds at a fixed surface area is accompanied by an increase in the membrane tension. If σ_{lysis} is reached in samples with smaller area available for the protrusions (smaller ε_C) and large v, the caps may undergo transient lysis and partially expel their contents (Fig. 5.7a, squares). Alternatively,

we also observe experimentally a collective mechanism of tension relief by coarsening, in which smaller caps disappear at the expense of growing spherical protrusions with increasing contact angle ψ (Fig. 5.7a, triangles).

The dynamical transformations of tubes under volume changes are shown in Fig. 5.7b. In moderate hyper-osmotic conditions, tubes elongate in the first 100 s and then reach a plateau (Fig. 5.7c, circles), whereas in a stronger hyper-osmotic shock, the elongation proceeds more rapidly and leads to tubes collapse and detachment, as discussed previously (Fig. 5.5c). In hypo-osmotic conditions, tubes are converted into buds (Fig. 5.7c, squares). Theoretically, we can fit the tube dynamics by using a permeation coefficient 60 times smaller than the one used in Fig. 5.7 and reported for DOPC vesicles in tension [Olbrich et al., 2000]. We rationalize the reduced water permeation by the decreased area/lipid in the tubes under negative tension, consistent with previous experiments on bilayers of different composition [Mathai et al., 2008]. To our knowledge, these are the first observations showing that the membrane permeability can be controlled by the strain.

5.4 Simulation results

5.4.1 Protrusions in equilibrium

We perform the simulation at very slow rate to avoid dynamical effects. We compressively strain a disk of radius $R_0 = 4$ µm, and reduced volume of $v = 1.5$. Upon compression , a spherical protrusion forms, and then evolves into a tube as shown in Fig. 5.8. We continue the simulation by allowing slow volume exchange, from $v = 1.5$ to $v = 2.6$, and observe a transformation from a tubular to a vesicular protrusion.

To assess the accuracy of the theoretical model of section 5.2, we compare it against these slow dynamic axisymmetric simulations. Figures 5.9 compares the morphologies predicted by each model for a process in which the bilayer is first compressed, then the interstitial volume is increased at constant compression, and finally the compression is removed. Despite the rigidity in the shapes allowed by the proposed model, they

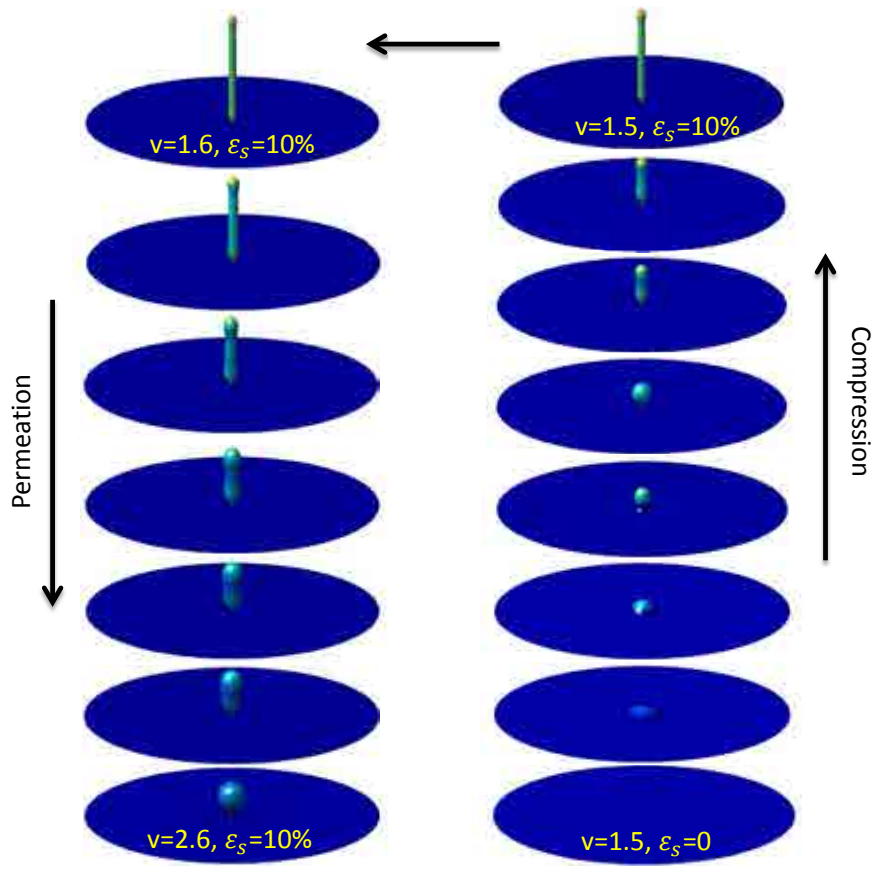

Figure 5.8: Morphological protrusions out of planar membrane characterized in terms of the area strain and enclosed volume. A planar disk of radius $R = 4$ µm, adhered to the substrate is compressed to 10% of its initial area, leading to spherical and tubular morphologies. The simulation is followed by a volume exchange ($v = 1.5$ to $v = 2.6$) resulting in retraction of spherical protrusions.

agree with the morphologies observed in the simulations remarkably well.

5.4.2 Rate effects: observation of complexes

In our experiments, more complex membrane morphologies were observed, which cannot be explained by an equilibrium model. For example, in case of rapid membrane expansion, instead of a gradual tube shortening, an abrupt retraction of the tubes into lipid globules was observed (Fig. 5.10i). When expelled again by adding area or volume, the protrusions assume complex shapes like tube-sphere complexes (ii),

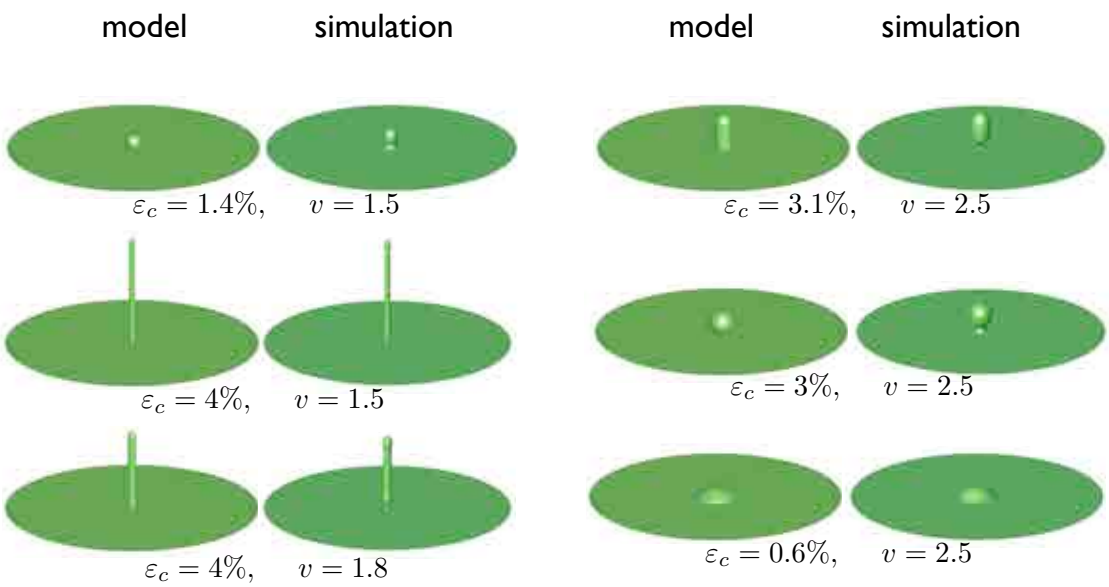

Figure 5.9: Validation of the theoretical model against numerical simulations. We compare the morphologies predicted by the equilibrium model with numerical axisymmetric simulations, which allow for general shapes and density distributions. These dynamical simulations combine the free energy described here with the dissipative forces coming from membrane hydrodynamics and from inter-monolayer and bilayer-substrate friction. We perform very slow simulations to eliminate rate effects, and follow a path in strain-volume space. The selected snapshots show that the geometric ansatz in the analytical model quite closely resemble the morphologies predicted by the simulations. The free energy discrepancies are below 5%, and the simulations show that, as assumed, the lipid densities at the monolayer neutral surface are nearly uniform. Our simulations show that tubes have thinner necks at the contact point with the planar bilayer, due to the high adhesion energy.

branched tube-discocyte (iii), starfish (iv), as well as branched tubes (v) (Fig. 5.10, confocal micrographs).

We explain these observations by the dynamical effects associated with the rate of strain ($\dot{\varepsilon}_c$), and investigate them by performing simulations. We expect that for large strain rates, the friction with the substrate retards the lipid flow velocity (v^-) in the lower monolayer (Fig. 5.10a) and leads to a difference in the number of lipids between the monolayers in the protrusion, which we can quantify by m_0 [Miao et al., 1994]. By analogy to the model of [Evans and Yeung, 1994], we introduce here a critical compression rate as $\dot{\varepsilon}_{cr} = K_s/(\pi R_0^2 b_s)$. Thus we expect the retardation to be

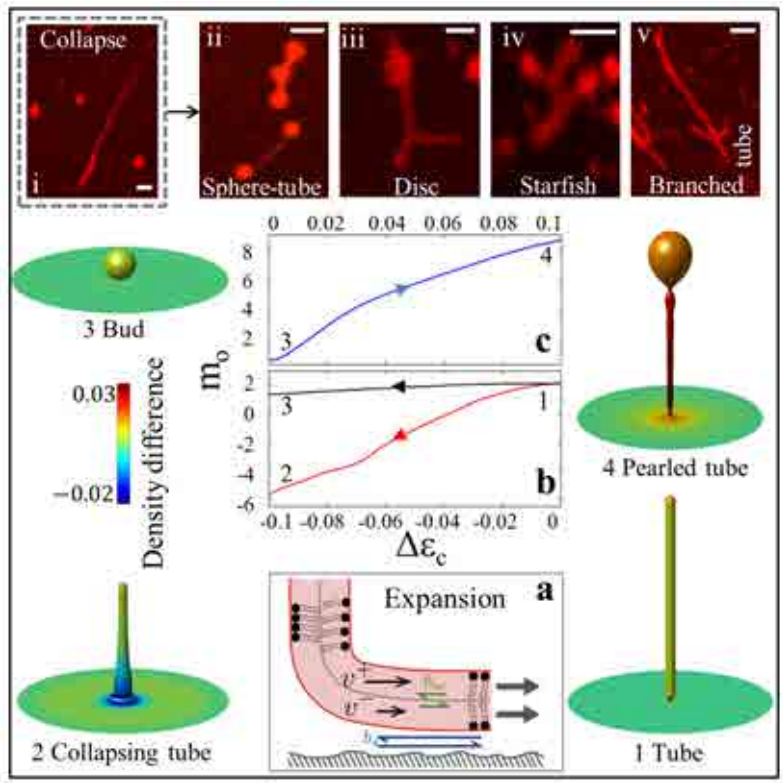

Figure 5.10: Dynamic strain effects. Confocal micrographs of i) a collapsing tube and the various emanating shapes, like sphere-tube complex (ii), branched tube-discocyte (iii), starfish (iv), as well as branched tubes (v). Scale bar 2.5 µm. (a) A sketch of the lipid retardation due to friction in the lower monolayer upon expansion is given. v^+ and v^- are the velocities in the lower and upper monolayers, respectively, and b_m and b_s are the friction coefficients between the two monolayers and between the substrate and the lower monolayer, respectively. (b) Area difference (m_0) during tube retraction upon slow (black curve), and fast, (red curve) expansion rates. (c) Positive area difference developing in a bud upon fast, membrane compression (blue curve). Simulation snapshots of the 1) tube, 2) the collapsing tube, 3) the bud and 4) the pearled tube are given, with a color plot indicating the normalized density difference between the monolayers.

significant for strain rates larger than $\dot{\varepsilon}_{cr}$, in which case our simulations show that the friction force depletes the outer monolayer of lipids (Fig. 5.10a) and results in a negative m_0 (Fig. 5.10b). For tubes (snapshot 1), the depletion is most significant at

the base, where the membrane bends inward into a disc-like feature, causing the rapid retraction. In contrast, when $\dot{\varepsilon}_c = \dot{\varepsilon}_{cr}$, the tube gradually shortens to a bud (snapshot 3), in agreement with the equilibrium picture. Upon rapid membrane compression on the other hand, friction forces result in large positive (Fig. 5.10c), which may trigger outward membrane bending, as for example, the bud elongation into a pearled tube. According to our estimates, the timescale for the relaxation of the area difference is of a second or less, which is very fast to be captured by the confocal imaging rates. We hypothesize that during the rapid tube collapse, triggered by negative m_0, the bilayer undergoes irreversible topological changes (e.g. inward budding), which may account for the complex morphology of the protrusions; for example, it is observed experimentally that the branches of the starfish often nucleate from structures within the protrusion.

5.5 Summary

We have shown that supported bilayers form a variety of protrusions, whose shapes can be experimentally controlled and quantitatively understood in terms of the bilayer-substrate mechanics. The proposed mechanisms do not depend on the previously studied effects of bilayer asymmetry or spontaneous curvature by proteins [McMahon and Gallop, 2005, Li et al., 2011]. In fact, passive mechanical and protein-regulated transformations of membranes may act in concert. Our results provide a mechanistic interpretation of the initiation and growth of blebs [Charras and Paluch, 2008], tubular invaginations [Morris and Homann, 179], and micro-vesicles in cells [Sens and Gov, 2007]. Since our experimental system offers a high degree of control, generates diversity of shapes and lipid densities, it is an ideal workbench to study protein affinity to curvature and lipid packing [Antonny, 2011]. Our findings could also help engineer new functionalities into drug delivery systems, such as strain- or pressure-responsive bilayer coated particles.

Chapter 6

Cholesterol adsorption

Cholesterol is a major constituent of cell membranes. It is crucial for the cell functionality by regulating the membrane fluidity, permeability, elastic stiffnesses (bending and stretching), etc [Kwik et al., 2003]. Multiple medical disorders, including atherosclerosis, Tangier disease, and Alzheimer's disease, are correlated to the elevated cellular cholesterol level [Maxfield and Tabas, 2005]. The cholesterol content of the cell is regulated by complex mechanisms of modification and storage, such as the esterification/hydrolysis cycles. When the cholesterol content of peripheral tissues is deregulated, macrophages engulf saturated lipoprotein particles [Tabas, 2000]. A key pathogenic event in the development of atherosclerosis is related to morphological changes of macrophages in vessel walls, leading to the formation of foam cells. It has been speculated that such drastic reorganizations are due to the cholesterol intake by the cell membrane and its interaction with F-actin network [Qin et al., 2006, Norman et al., 2010, Grosheva et al., 2009]. Elevating the cholesterol content of macrophage membranes results in cell spreading and also formation of membrane ruffles in the presence of the cell adhesion [Qin et al., 2006].

We hypothesize that the morphological and functional changes in macrophages may result from the bilayer reorganizations upon cholesterol intake under confinement. In this study, our goal is to utilize a model experimental system, which mimics the cell membrane in confinement and the cholesterol delivery to the plasma membrane, to observe dynamical reorganizations of the membrane. We consider supported lipid

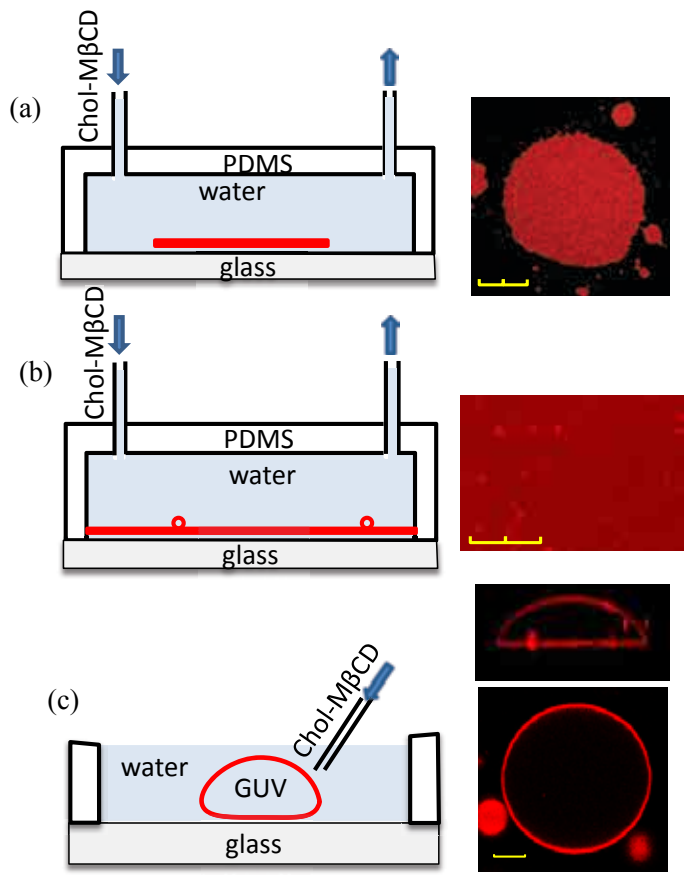

Figure 6.1: Experimental setup: (a) a SLB patch, (b) a continuous SLB, (c) a giant unilamellar vesicle (GUV) adhered to the substrate. The preparation methods are explained in section 6.1. In (a) and (b), the solution above the bilayer is replaced by the MβCD-Chol solution with a pump. In (c), the difference in the molecular weight of the sucrose (outer solution) and glucose (inner solution) leads to GUV sedimentation on the glass. The microscope images of the bilayer in three systems are shown. A horizontal cross-section microscope image of a GUV, adhered to the substrate, are also shown. Scale-bar is 10 µm in all snapshots.

bilayers (SLBs), previously used as a model system for confined plasma membranes.

Free cholesterol molecules are highly hydrophobic, and therefore insoluble in blood and water. The transport of cholesterol in the bloodstream and in other fluid environments inside or outside of cells is mediated by lipoproteins. Lipoproteins are protein-

rich vesicular particles enclosed by a monolayer lipid membrane, which are able to store fats (cholesterol and triglyceride esters) in their interior. Methyl-β-cyclodextrin (MβCD) has been shown to behave as synthetic a proxy for lipoproteins [Qin et al., 2006], encapsulating cholesterol molecules and making the compound MβCD soluble in water. For instance, MβCD has been shown to become loaded with cholesterol, depleting exposed cell membranes [Christian et al., 1997]. MβCD has been used to manipulate the cholesterol content of cell membranes in a number of in-vivo experiments [Qin et al., 2006, Norman et al., 2010, Grosheva et al., 2009]. Here, we deliver cholesterol to model membranes with a solution of MβCD.

Due to their fluidity, flexibility and bilayer structure, amphiphilic membranes may undergo fast shape transformations and reorganizations. However, previous experiments on cell membrane cholesterol manipulation, either depletion or elevation, are limited to observations before and after 15-30 minutes incubation [Qin et al., 2006, Norman et al., 2010, Grosheva et al., 2009]. Therefore, the mechanisms behind cell spreading, morphological changes, aggregation of lipid droplets, and, most importantly, the formation of foam cells, have remained elusive. Previous studies have shown that local perturbations of the membrane by inserting lipids [Thid et al., 2007, Giger et al., 2008] or proteins [Domanov and Kinnunen, 2006], lipid flip-flop [Papadopulos et al., 2007, Sens, 2004], or anchoring polymers [Tsafrir et al., 2003] can induce the fast formation of membrane protrusions, and possibly topological changes, suggesting such events may take place upon cholesterol intake. Here, we consider a simple in-vitro experimental system, which allows us to track the fast shape transformations of model membranes exposed to the cholesterol solution.

We explore experimentally the response of lipid bilayers to the cholesterol solution in three different conditions of confinement, see Fig. 6.1. First, we deliver the cholesterol to SLB patches (a), which are not confined laterally. Consequently, we observe that the membrane easily spreads over the substrate upon the cholesterol intake, although when the spreading is fast, it is noticeably retarded by the membrane-substrate friction. We then repeat the experiment on continuous SLBs (b), laterally confined and separating osmotically the chamber solution and the interstitial fluid

film trapped between the bilayer and the substrate. Finally, we deliver cholesterol to GUVs adhered to the substrate, in a situation closer to cells confined by other cells, the extra-cellular matrix, etc. We observe a variety of dynamical responses that may explain physiological processes such as the formation of foam cells, and that can be understood in terms of the excess area upon cholesterol delivery and the bilayer confinement [Staykova et al., 2013]. To interpret the observations on SLB patches, we formulate a model for the adsorption dynamics coupled with a binary mixture viscoelastic lipid bilayer.

6.1 Materials and Methods

6.1.1 Materials

DOPC (1,2-dioleoyl-sn-glycero-3-phosphocholine), Rh-DPPE (1,2-dipalmitoyl-sn-glycero-3- phosphoethanolamine -*N*-(lissamine rhodamine-B sulphonyl) (ammonium salt)) were purchased from Avanti Polar Lipids, and chloroform, trizma hydrichloride (Tris.HCl), sucrose, Methyl-β-cyclodextrin (MβCD), and cholesterol-chelated methyl-β-cyclodextrin, also known as cholesterol water soluble were purchased from Sigma Aldrich. The concentrations of the cholesterol-chelated-MβCD (Chol-MβCD) solutions varied between 2 and 50 mg/ml in our experiments, with molar ratio of 1:6 cholesterol: MβCD, in consensus with most of the previous studies performed at 10 mg/mL. All materials were used without further purification. For the chamber, we use PDMS and curing agent from Dow Corning (Sylgard 184 Silicone Elastomer Kit, catalog no. 240 401 9862), microscope slides from Fisher Scientific (catalog no 12-544-1), and cover glasses from VWR (catalog no. 48366 045). For the preparation procedure of GUVs we used Indium Tin Oxide coated glasses (ITO glasses) from Delta Technologies (no. X180).

6.1.2 GUVs

Giant vesicles were prepared following the standard electroformation technique [Angelova and Dimitrov, 1986]. Briefly, lipid solution in chloroform with a total lipid concentration of 4 mM, consisting of 99.5 mol% DOPC and 0.5 mol% Rh-DPPE was used. A thin film of the lipid mixture was deposited on the ITO-coated glass, and dried overnight under vacuum. The electroformation chamber was assembled by two ITO-coated coverslips with the conductive sites facing each other, and separated by a 3 mm thick teflon gasket (the dimensions of the chamber were $1.0 \times 1.0 \times 0.3$ cm^3). The chamber was filled with 0.3 M solution of Glucose, connected to a sinusoidal AC electric field of frequency of 10 Hz and amplitude of 1.7 Vpp for 90 minutes, which resulted in the formation of giant lipid vesicles. For the experiments, freshly formed GUV suspension was diluted in a 0.3 M sucrose solution, at a 5:1 volume ratio.

6.1.3 Supported lipid bilayer

To prepare isolated patches of supported lipid bilayers (SLB patches), the GUV solution was diluted in Tris buffer (10 mM Tris.HCl, 150 mM NaCl, 2 mM CaCl2, adjusted with 1 M HCl to pH $\approx$ 7.5) at a 5:1 volume ratio and immediately deposited on a cleaned coverslip glass. After incubation for a couple of minutes the GUVs fused over the glass and formed circular patches of unilamellar lipid bilayers.

Continuous supported lipid bilayers (contSLB) were prepared using the standard SUV fusion method. Briefly, 25 µL of lipid solution (DOPC and Rh-DPPE in a 99.5/0.5 mol % ratio) was dried on the walls of a glass vial overnight and rehydrated in 2 mL Tris buffer. The resulting turbid suspension was sonicated with a probe sonicator (Branson) for 10 min at 40% power to obtain small unilamellar vesicles (SUV). The SUVs solution was diluted in Tris buffer at 5:1 volume ratio and immediately deposited on a cleaned coverslip glass. After incubation for about 10 min, we observed that an unilamelar contSLB covers the walls of the chamber.

6.1.4 Experimental setup

For our experiments on contSLBs and SLB patches, we prepared homemade channels of dimensions $l = 1$ cm, $w = 2$ mm $h = 1$ mm, constructed between a cleaned coverslip and PDMS. After filling the chambers with SUV or GUV suspensions and incubating for about half an hour to form contSLB or patches, respectively, we removed the unfused vesicles by washing with 0.3 M sucrose solution. The MβCD-Chol solution was introduced in the channel via a micro-syringe pump (Harvard Apparatus) at a velocity of about 10 µL/min. For the given cross section area of the chamber, this resulted in a flow with an average velocity of 5 mm/min, which had negligible effects on the bilayer integrity and transformations. The pump was stopped after the chamber was filled with the MβCD-Chol solution.

The local manipulation of GUVs was performed in an open well, about 5mm thick and wide. The density difference between the inner glucose solution and the outer sucrose solutions (0.3 M) drove the sedimentation of the GUVs on the glass substrate. A micromanipulator was used to introduce locally about 2 µL of MβCD-Chol solution, adjusted to 0.3 M to prevent osmotic shocks.

6.2 Results and discussions

6.2.1 Experimental observations: SLB patches

Upon exposure to the MβCD-Chol solution, the isolated SLB patches rapidly undergo a significant expansion as a result of cholesterol adsorption (Fig. 6.2a). After this initial expansion, we observe that the patch geometry is stable for some time, and then, in a longer time scale, the system undergoes an area contraction. Figure 6.2b quantifies these mechanisms, by plotting the normalized area deviation Δa of the bilayer patch exposed to MβCD-Chol solutions of different concentrations as a function of time. We understand the membrane contraction in terms of two effects, (1) cholesterol ordering, known also as membrane condensing, and (2) the tendency of free cyclodextrin, either originally present in the solution or left after cholesterol de-

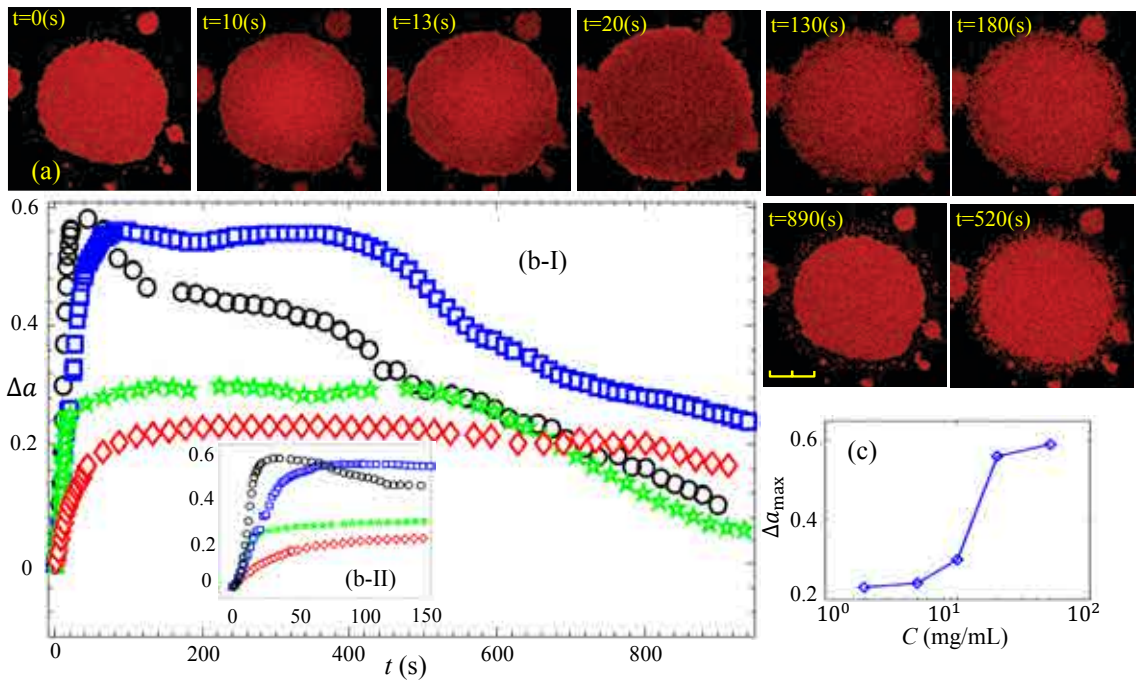

Figure 6.2: Dynamical transformations of an SLB patch upon the cholesterol adsorption. (a) Microscopy images of a bilayer patch exposed to the 50mg/mL MβCD-Chol solution. (b-I) Normalized area deviation of SLB patches $\Delta a = (A - A_0)/A_0$ versus time for several concentrations: 2 mg/mL (diamonds), 10mg/mL (stars), 20mg/mL (squares), 50 mg/mL (circles). We set $t = 0$ to the onset of the expansion, which occurs faster the higher the MβCD-Chol concentration. The area expansion occurs in the initial 30 to 100s (b-II), while retraction starts after about 500 s. (c) Maximum area expansion of SLB patches versus the MβCD-Chol concentration. Scale-bar: 10 µm.

livery, to borrow lipid molecules from the bilayer. Regarding (1), the bilayer physical properties, including the area per molecule and the thickness, have been shown to depend strongly on the cholesterol content [Alwarawrah et al., 2010, Edholm and Nagle, 2005, Pan et al., 2009]. In particular, the area per lipid molecule of a DOPC bilayer, studied by molecular simulation, decreases by increasing the membrane cholesterol mole fraction [Alwarawrah et al., 2010]. As for (2), free cyclodextrin has been shown to extract phospholipids from bilayers at longer time scales as compared to those of cholesterol delivery ([Zidovetzki and Levitan, 2007]). We quantify the contribution

of each of these membrane contraction mechanisms later, when studying continuous SLBs (Fig. 6.7c). During the membrane contraction, we observe fragments of lipid bilayer, indicating that the membrane tension is close to the lysis tension, as a result of the spreading tension due to adhesion energy (a few mN/m) [Ursell et al., 2011] and possibly a dynamical tension due to friction with the substrate.

Within the range of concentrations considered here, around that used in previous studies of cholesterol manipulation in cell membranes (10 mg/mL), we could not collapse the curves in 6.2b with a simple Langmuir adsorption model, with adsorption and desorption coefficients independent of concentration. We report the maximum normalized area expansion as a function of MβCD-Chol concentration in 6.2c.

As highlighted in Fig. 6.2b-II, the expansion is faster for higher concentrations. Interestingly, when the concentration is high and the expansion is very fast, e.g. for 50 mg/mL, we observe a transient nonuniform distribution of florescent intensity (FI) over the membrane (6.2a, t=10,13 s). We interpret the nonuniform FI as the result of a nonuniform distribution of labelled DOPC and cholesterol molecules in the membrane. The fact that such non uniformity arises when spreading is fast suggests that it is due to a rate-dependent force, such as friction between the expanding bilayer and the substrate. We scrutinize next the initial stages of the experiment, in which the patches rapidly grow (first tens of seconds), neglecting condensation or phospholipid removal by free MβCD.

6.2.2 Modeling the membrane spreading

We consider our previous viscoelastic bilayer model [Rahimi and Arroyo, 2012], and extend it to a bilayer made out of two species (cholesterol and DOPC). Here, we assume that the cholesterol concentration in the bulk is fixed, and ignore spacial gradients as a result of the injection or adsorption processes. At high concentrations the amount of cholesterol adsorbed is small compared to the cholesterol available in solution, and the diffusion in the bulk is faster than diffusion on the patch.

Surface binary mixture transport equations

For a binary mixture fluid interface with a gradient of concentration, there is a thermodynamic tendency toward uniform concentrations. The flux of particles is driven by the mixing entropy, and is given by the first Fick's law $\boldsymbol{J} = -D(\phi)\boldsymbol{\nabla}\phi\,(\boldsymbol{x}, t)$ [Dill, 2002, Brennen, 2005], where $\phi\,(\boldsymbol{x}, t)$ denotes the concentration field of particle A, here the area fraction of Cholesterol (Chol), and $D(\phi)$ denotes the diffusion coefficient. With this in mind, introducing $\phi^{\pm}$ as the Chol area fraction in each monolayer (by $\pm$ we denote the outer and inner monolayers), and ρ^{Chol} as the inverse of the area per Chol molecule a^{Chol}, we express the transport equation of Chol particles as

$$\frac{\partial\left(\rho^{Chol\pm}\phi^{\pm}\right)}{\partial t} + \nabla\cdot\left(\rho^{Chol\pm}\phi^{\pm}\boldsymbol{v}^{\pm}\right) - \boldsymbol{\nabla}\cdot\left(\rho^{Chol\pm}D[\phi^{\pm}]\boldsymbol{\nabla}\phi^{\pm}\right) \pm S_t(\phi^{+},\phi^{-}) = S^{\pm}(\phi^{\pm}), \tag{6.1}$$

Here, $\boldsymbol{v}^{\pm}$ denotes the velocity field of each monolayer and $S^{\pm}$ denotes the rate of the Chol adsorption per unit area. By S_t, we denote the transbilayer diffusion (flip-flop) due to the concentration contrast, often given as $\pm\alpha_t\left(\phi^{+} - \phi^{-}\right)$ [Evans and Yeung, 1994].

For an isolated SLB patch adhered to the substrate, we assume that the outer monolayer is exposed to the solution of MβCD-Chol, while the inner monolayer is deposited over the substrate. Then, the source term for the inner monolayer is $S^{-} = 0$, and for the outer monolayer is given based on a standard surface adsorption kinetics

$$S^{+} = \rho^{Chol+}\left[-k_d\phi^{+} + k_a C\left(\phi^{max} - \phi^{+}\right)\right], \tag{6.2}$$

where k_d, and k_a denote the desorption and adsorption rate constants, C denotes the cholesterol concentration in the ambient fluid, and ϕ^{max} denotes the maximum limit of the Chol area fraction. We note that assuming a homogeneous field of the cholesterol in an inextensible membrane results in an ordinary differential equation

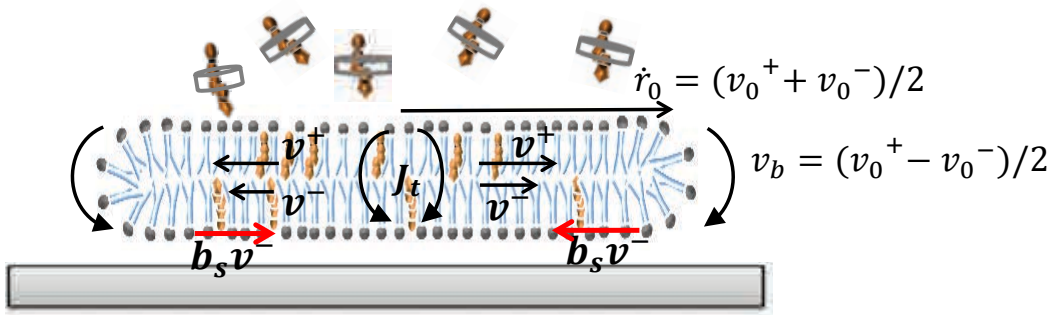

Figure 6.3: Chol-DOPC bilayer adsorption and spreading mechanisms. Observable velocity at the boundary $\dot{r}_0$, as well as the transbilayer flux J_t, and the lipid transfer velocity from the outer monolayer to the inner monolayer at the boundary v_b are shown. Friction force from the substrate is shown $b_s v_0^-$.

$\dot{\phi}^+ = -k_d\phi^+ + k_a C\left(\phi^{max} - \phi^+\right)$, whose solution is given by

$$\phi(t) = \frac{\phi^{max}}{1 + k_d/k_a C}\left(1 - e^{-[k_d + k_a C]t}\right).$$

Using the above relation, one can express the area variation of the patch by $\Delta A/A_0 = \phi/\left(1-\phi\right)$.

Since the cholesterol flip-flop is known to be very fast (in polyunsaturated bilayers, cholesterol undergoes flip-flop on a submicrosecond time scale Bennett et al. [2009]), for simplicity, we assume $\phi^- = \phi^+$. Then, we rewrite Eq. (6.1) for the outer, and inner monolayers as

$$\begin{aligned}
\frac{\partial\left(\rho^{Chol+}\phi\right)}{\partial t} + \nabla\cdot\left(\rho^{Chol+}\phi\boldsymbol{v}^+\right) - \boldsymbol{\nabla}\cdot\left(\rho^{Chol+}D[\phi]\boldsymbol{\nabla}\phi\right) &= S^+(\phi), \\
\frac{\partial\left(\rho^{Chol-}\phi\right)}{\partial t} + \nabla\cdot\left(\rho^{Chol-}\phi\boldsymbol{v}^-\right) - \boldsymbol{\nabla}\cdot\left(\rho^{Chol-}D[\phi]\boldsymbol{\nabla}\phi\right) &= 0,
\end{aligned} \tag{6.3}$$

Introducing a_0^{Chol} as the area per Chol molecule and a_0^{DOPC} as the area per DOPC molecule in a relaxed binary mixture bilayer, the average density of a relaxed bilayer

can be expressed by

$$\rho_0 = \frac{n_{tot}}{A_{tot}} = \frac{n_{Chol}}{A_{tot}} + \frac{n_0^{DOPC}}{A_{tot}} = \frac{A_{chol}/a_0^{chol}}{A_{tot}} + \frac{A_{DOPC}/a_0^{DOPC}}{A_{tot}} = \phi\rho_0^{Chol} + (1-\phi)\,\rho_0^{DOPC}.$$

Similarly the average density in an out-of-equilibrium state can be expressed by

$$\rho^{\pm} = \phi\rho^{Chol\pm} + (1-\phi)\,\rho^{DOPC\pm}. \tag{6.4}$$

Substituting ϕ by $(1-\phi)$ in Eq. (6.3), we derive the transport equation for the DOPC molecules,

$$\frac{\partial\left(\rho^{DOPC+}\left[1-\phi\right]\right)}{\partial t} + \boldsymbol{\nabla}\cdot\left(\rho^{DOPC+}\left[1-\phi\right]\boldsymbol{v}^{\pm}\right) + \boldsymbol{\nabla}\cdot\left(\rho^{DOPC+}D[\phi]\boldsymbol{\nabla}\phi\right) = 0, \tag{6.5}$$

Using Eq. (6.4) and summing up Eq. (6.3) and Eq. (6.5), one can express the total conservation of mass as

$$\frac{\partial\rho^{\pm}}{\partial t} + \boldsymbol{\nabla}\cdot(\rho^{\pm}\boldsymbol{v}^{\pm}) = \boldsymbol{\nabla}\cdot\left(\left[\rho^{Chol\pm} - \rho^{DOPC\pm}\right]D(\phi)\boldsymbol{\nabla}\phi\right) + S^{\pm}, \tag{6.6}$$

For simplicity in numerical calculation we attribute the compressibility of the membrane to that of the DOPC molecules. In other words, we assume that the area per Chol molecule is constant i.e. $\rho^{Chol\pm} \approx \rho_0^{Chol}$, even if the binary bilayer is stretched or compressed. Thus, Eqs. (6.3) can be simplified as

$$\begin{aligned}
\frac{\partial\left(\phi\right)}{\partial t} + \nabla\cdot\left(\phi\boldsymbol{v}^{+}\right) - \boldsymbol{\nabla}\cdot\left(D[\phi]\boldsymbol{\nabla}\phi\right) &= S^{+}(\phi)/\rho^{Chol}, \\
\frac{\partial\left(\phi\right)}{\partial t} + \nabla\cdot\left(\phi\boldsymbol{v}^{-}\right) - \boldsymbol{\nabla}\cdot\left(D[\phi]\boldsymbol{\nabla}\phi\right) &= 0.
\end{aligned} \tag{6.7}$$

Interestingly, subtracting Eqs. (6.7) we obtain

$$\nabla\cdot\left(\phi\left[\boldsymbol{v}^{+} - \boldsymbol{v}^{-}\right]\right) = S^{+}(\phi)/\rho^{Chol}. \tag{6.8}$$

This relation indicates that the Chol adsorption necessarily imposes an interlayer slippage to the system. To satisfy this condition on the boundary of the SLB patch, we allow a lipid flow from outer leaflet to the inner leaflet on the boundary as shown in Fig. 6.3.

Governing equations

For a planar bilayer, adhered to the substrate, the free energy is due to the deviations from the equilibrium density ρ_0, and the adhesion potential. Introducing K_s as the elastic stretching modulus of each monolayer, and γ as the adhesion energy between the bilayer and the substrate, the free energy per unit area can be written as

$$f = \frac{K_s}{2}\left[\left(\frac{\rho^+}{\rho_0}-1\right)^2+\left(\frac{\rho^-}{\rho_0}-1\right)^2\right]-\gamma.$$

Given the free energy per unit area we can calculate the total elastic energy

$$\Pi = \int_\Gamma f dS, \tag{6.9}$$

where, dS is the area element, and Γ is the evolving surface domain. We calculate now the rate of the elastic energy functional as a function of the velocity field $\boldsymbol{v}^\pm$ and the observable velocity of the boundary $\dot{r}_0$, required to derive the governing energy

$$\dot{\Pi}[\boldsymbol{v}^\pm, \dot{r}_0] = \int_\Gamma f_{,t} dS + \int_\Gamma f (dS)_{,t},$$

where

$$f_{,t} = K_s\left[\left(\frac{\rho^\pm_{,t}\rho_0 - \rho^\pm \rho_{0,t}}{\rho_0^2}\right)\left(\frac{\rho^\pm}{\rho_0}-1\right)\right],$$

$$\rho_{0,t} = \phi_{,t}\left(\rho_0^{Chol} - \rho_0^{DOPC}\right),$$

and $\rho^\pm_{,t}$ can be computed from Eq. (2.5), $\phi_{,t}$ can be computed from Eq. (6.7) and the rate of change of area element $(dS)_{,t}$ is given in appendix A.2 for general surfaces.

We note that for a planar axisymmetric surface, all variables can be described in parametric space, such as $r(u)$, which results in $dS = 2\pi r r' du$ and therefore $(dS)_{,t} = 2\pi(r' r_{,t} + r r'_{,t})du$.

The dissipative mechanisms of the bilayer include the monolayer surface viscosity, the friction between two monolayers and the friction between the substrate and the inner leaflet. We consider each monolayer as a Newtonian interfacial fluid, resulting in a linear relation between the surface shear stress and the rate of the deformation $\boldsymbol{d}$ [Arroyo and DeSimone, 2009]. In addition, we account for the interlayer slippage and the membrane- substrate friction following [Rahimi and Arroyo, 2012]. Thus, introducing μ_s as the membrane shear viscosity, λ_s as the dilatational viscosity, b_m as the interlayer friction coefficient, and b_s as the membrane-substrate friction, we can write the Rayleigh dissipation potential as

$$\begin{aligned} W[\boldsymbol{v}^{\pm}, \dot{r}_0] = & \quad \frac{1}{2}\int_{\Gamma} \left(2\mu_s \boldsymbol{d} : \boldsymbol{d} + \lambda_s (\mathrm{tr}\boldsymbol{d})^2\right)^{\pm} dS \\ + & \quad \frac{b_m}{2}\int_{\Gamma} \|\boldsymbol{v}^{+} - \boldsymbol{v}^{-}\|^2 dS + \frac{b_s}{2}\int_{\Gamma} \|\boldsymbol{v}^{-}\|^2 dS. \end{aligned} \tag{6.10}$$

The dynamics of the system can be obtained by minimizing the Rayleigh dissipation potential plus the rate of change of the elastic energy with respect to the variables expressing the rate of change of the system [Goldstein et al., 2001]. This minimization is often constrained. For this purpose, we form the Lagrangian

$$\mathcal{L}[\boldsymbol{v}^{\pm}, \boldsymbol{\Lambda}] = W[\boldsymbol{v}^{\pm}] + \dot{\Pi}[\boldsymbol{v}^{\pm}] - \boldsymbol{\Lambda} \cdot \boldsymbol{C}[v_n, \boldsymbol{v}^{\pm}], \tag{6.11}$$

Since this minimization is often constrained, $\boldsymbol{C}[\boldsymbol{v}^{\pm}]$ collects all the constraints and $\boldsymbol{\Lambda}$ the corresponding Lagrange multipliers. Here, for a SLB patch the only boundary condition is that the observable velocity of the boundary $\dot{r}_0$ is linked to the physical velocities of each leaflet at the boundary as $\dot{r}_0 = (v_0^{+} + v_0^{-})/2$. From the above minimization problem we calculate $\boldsymbol{v}^{\pm}$, and $\dot{r}_0$. We integrate forward $\dot{r}_0$ in time to update the geometry of the bilayer. Given $\boldsymbol{v}^{\pm}$, and $\dot{r}_0$, we solve the transport equations

for the average density and Chol area fraction (Eqs. (6.6) and (6.7)), which are partial differential equations. To accomplish this, we discretize all the governing equations with a Galerkin method and for axisymmetric surfaces.

6.2.3 Numerical results

Figure 6.4 presents the dynamical coupling of the membrane viscoelasticity with the cholesterol adsorption (50 mg/mL MβCD-Chol). The response of the system is calculated with both, the uniform adsorption model, and the coupled adsorption/viscoelastic non-uniform model, and the area expansion predictions are compared to the experimental observations in Fig. 6.4a. The significant drag of the membrane spreading by substrate friction is apparent from the figure, in good agreement with experimental observations (Fig. 6.4a).

Figure 6.4b shows the radial FI profile of the bilayer during the expansion, where the lower FI on the edge indicates a higher cholesterol area fraction. As cholesterol is adsorbed, the bilayer expansion is laterally impeded by substrate friction. Such impediment is stronger at the center of the patch, making it easier for the edge to relax its excess molecules by lateral flow and adsorb more cholesterol. On the other side, mixing entropy and stretching elasticity push the system towards a uniform state, chemically and mechanically. Figure 6.4c shows the difference of FI between the edge and the center of the patch, gathered from the experiment and simulations, demonstrating a good quantitative agreement in the non-uniformity of the patch. The dynamics of the system as predicted by the simulations is shown in Fig. 6.4d, where the color map represents the FI.

We choose the material parameters based on the reported values in the literature and the best fit with our experimental results (Table .6.1). The maximum area fraction ϕ^{max} can estimated based on the solubility limit given in the literature ($\mathscr{X}^{max} = 0.66$) [Alwarawrah et al., 2010] as

$$\mathscr{X} = \frac{n^{Chol}}{n^{Chol} + n^{DOPC}} = \frac{A^{Chol}}{A^{Chol} + A^{DOPC} a^{Chol}/a^{DOPC}} = \frac{A^{Chol}/A^{DOPC}}{A^{Chol}/A^{DOPC} + a^{Chol}/a^{DOPC}}$$

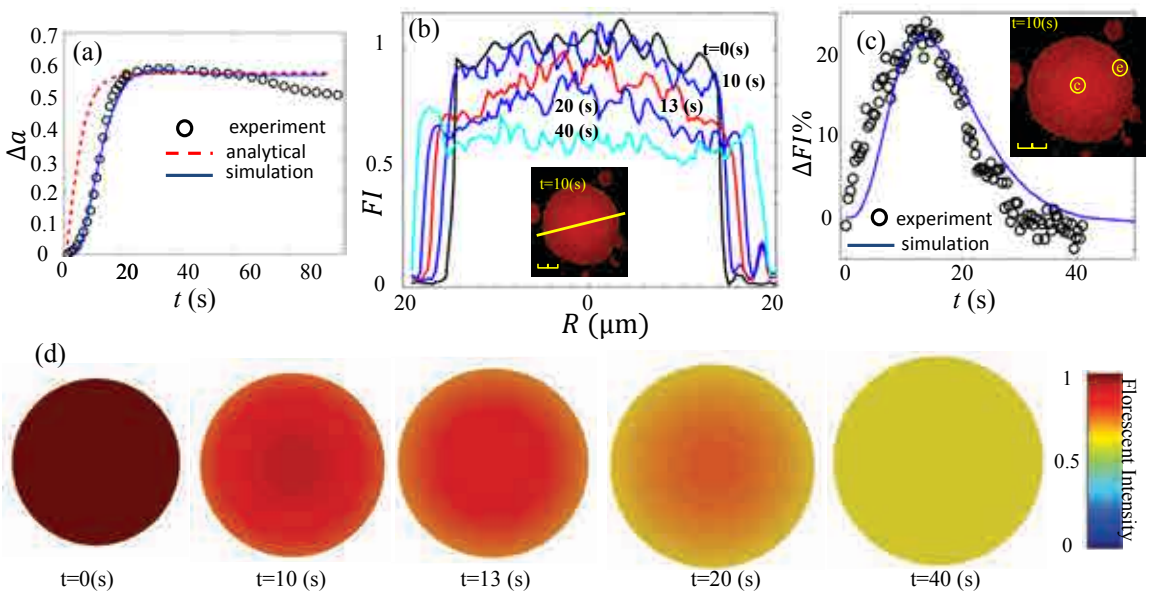

Figure 6.4: Nonuniform distribution of the cholesterol in DOPC bilayer during the expnsion, at high concentrations (50 mg/mL MβCD-Chol). (a) Normalized area deviation of the SLB patch during the spreading, measured experimentally, and predicted from the uniform adsorption model and the coupled adsorption/viscoelastic non-uniform model. (b) Radial FI profile at different time instants (t=0, 10, 13, 20, 80 s), showing the nonuniform cholesterol distribution. Scale-bar: 10 µm. (c) Normalized florescent intensity difference between the patch center and edge, $\Delta FI = (FI_c - FI_e)/FI_0$, from the experiment and simulation. (d) Simulation results for the dynamics of an isolated patch exposed to a 50 mg/mL MβCD-Chol solution. The color map represents normalized florescent intensity, computed from $FI \propto (1-\phi)\rho^{DOPC}$, where ρ^{DOPC} is the inverse of the area per DOPC molecule.

Table 6.1: Material properties

Dissipative parameters	μ_s	$10^{-9}\ Js/m^2$ [Jönsson et al., 2009]
	λ_s	0
	b_m	$1 \times 10^9\ Js/m^4$ [Merkel et al., 1989]
	b_s	$5 \times 10^9\ Js/m^4$ [Jönsson et al., 2009]
Elastic modulus	K_s	$0.1\ J/m^2$ [Jönsson et al., 2009]
Adsorption parameters	K_a	0.008 1/s
	K_d	0.15 1/s
	ϕ_{max}	0.5
Area per molecule ratio	a^{Chol}	0.25 nm^2 [Alwarawrah et al., 2010]
	a^{DOPC}	0.5 nm^2 [Alwarawrah et al., 2010]
Adhesion potential	γ	$2\ J/m^2$ [Swain and Andelman, 2001]
Entropic constant	$K_bT \times \rho^{Chol}$	$0.02\ J/m^2$

Thus $A^{Chol}/A^{DOPC} = a^{Chol}/a^{DOPC} \times \mathscr{X}/(1-\mathscr{X})$. On the other hand

$$\phi = \frac{A^{Chol}}{A^{Chol} + A^{DOPC}} = \frac{A^{Chol}/A^{DOPC}}{A^{Chol}/A^{DOPC} + 1} \rightarrow \phi = \frac{a^{Chol}/a^{DOPC}\,\mathscr{X}}{(a^{Chol}/a^{DOPC} - 1)\mathscr{X} + 1}$$

Therefore given the maximum solubility $\mathscr{X}^{max} = 0.66$, and the ratio of the area per molecule $a^{Chol}/a^{DOPC} \approx 0.5$ one can estimate $\phi^{max} \approx 0.5$.

The dynamics of the membrane spreading, including the cholesterol adsorption, the area expansion, and lipid hydrodynamics are presented in Fig. 6.5. Figure 6.5a shows the area expansion of a bilayer of radius $R = 16$ µm exposed to cholesterol solution of different concentrations. Figure 6.5b shows the FI gradient in the membrane, i.e. the difference of the FI between the middle and the edge of the membrane. Figure 6.5c shows the observable velocity of the patch growth, and the actual lipid velocities (outer and inner monolayers) on the boundary. Also the lipid flow on the edge between the leaflets is shown in this figure v_b. The profile of velocity fields for each monolayer is shown in Fig. 6.5d.

Figure 6.6 shows the relaxation dynamics of an SLB patch exposed to 50 mg/mL Chol solution, highlighting a drastic nonuniform lipid crowding. Here the lipid flow on the inner monolayer is extremely retarded by the substrate friction force.

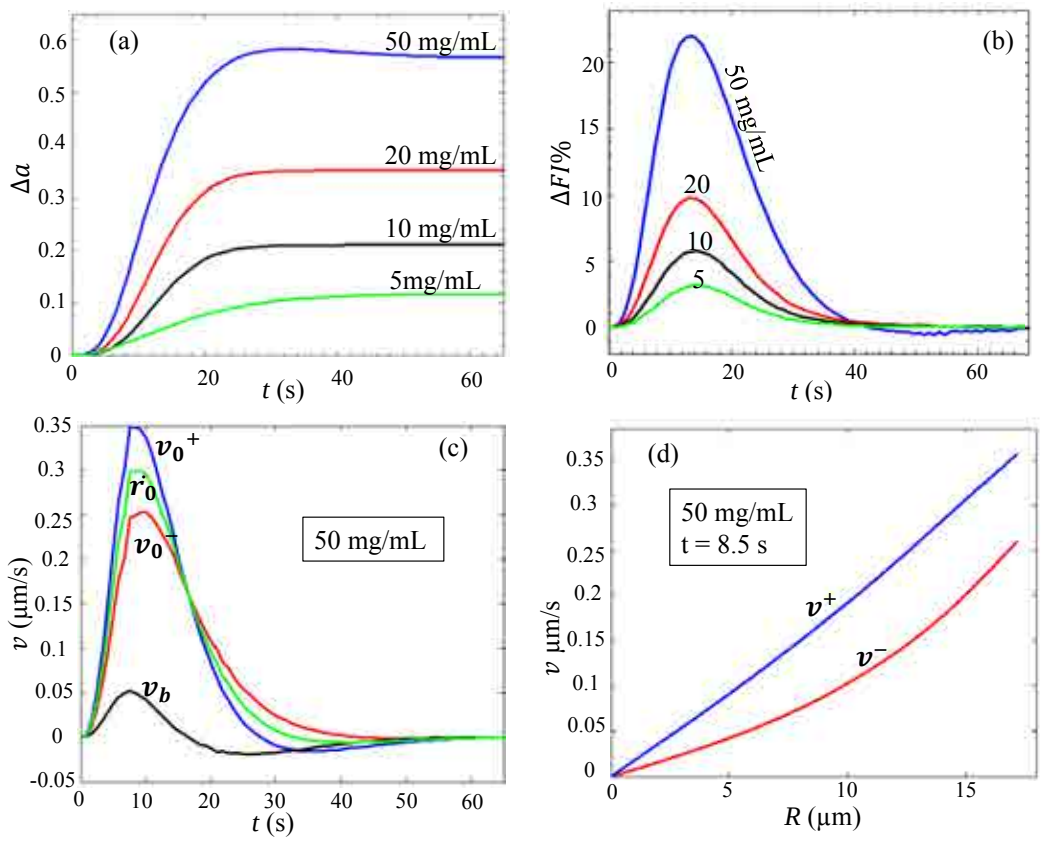

Figure 6.5: Membrane spreading dynamics. (a) Normalized area deviations of SLB patches versus time, exposed to MβCD-Chol of different concentrations. (b) Gradient of Florence Intensity versus time $\Delta FI = FI_{center} - FI_{edge}$. (c) Observable velocity $\dot{r}_0$, outer and inner leaflet velocities on the edge $v_0^{\pm}$, and the velocity of the flow from the outer leaflet to inner one on the boundary v_b (see Fig. 6.3) are computed versus time for a SLB exposed to 50 mg/mL Chol solution. (d) Velocity profile of the bilayer for outer, and inner monolayers at t=8.5 s.

6.2.4 Experimental observations: continuous SLB

We turn now to continuous SLB, where as shown in Fig. 6.7a, tubular and spherical protrusions nucleate and evolve upon exposure to MβCD-Chol solution. We interpret these observations in the light of previous chapter, where we found that laterally compressed SLB develop such protrusions, and that their morphology can be reversibly controlled by the amount of excess area and by the enclosed volume between the membrane and substrate, regulated osmotically. Here, the excess area is provided by

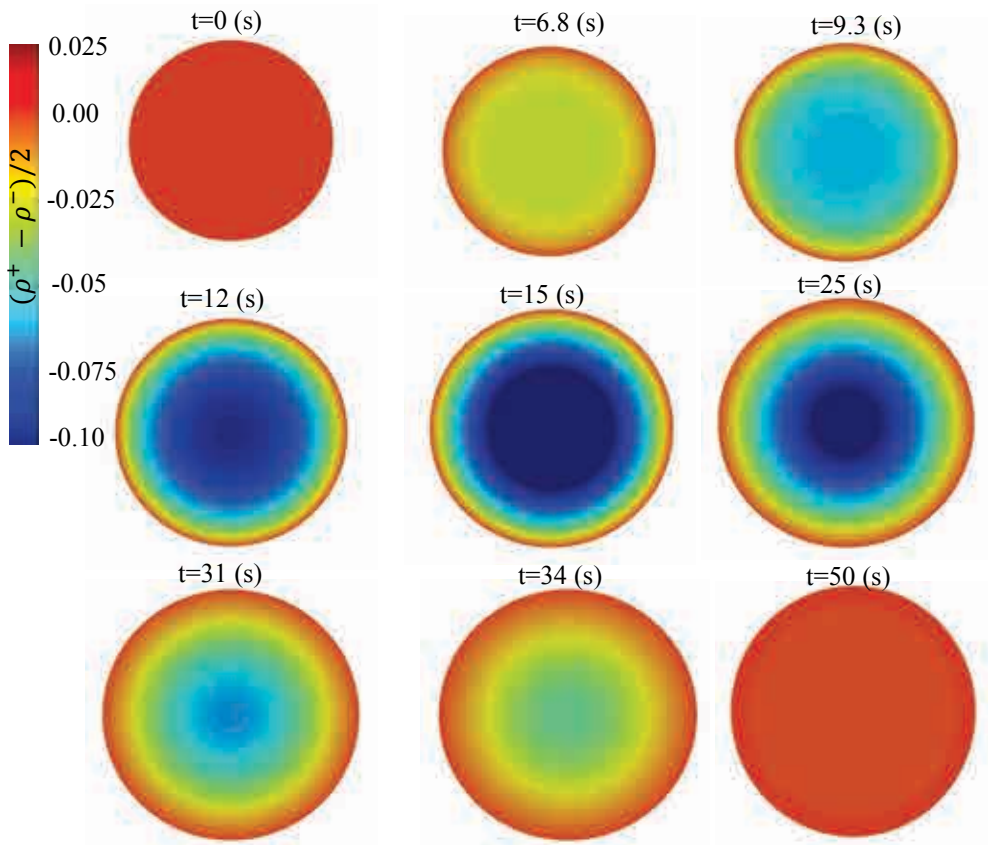

Figure 6.6: Relaxation dynamics of an SLB patch exposed to 50 mg/mL Cholesterol solution. Color map shows the density difference $(\rho^+ - \rho^-)/2$.

the cholesterol intake, and we keep the chamber osmolarity constant.

The formation and evolution of protrusions depicted in Fig. 6.7a is quantified by plotting the projected area of the protrusions in Fig. 6.7b, where we also plot for reference the normalized excess area of an isolated patch under the same conditions. Note that for tubular and spherical protrusions, the projected area is not exactly the bilayer area. However, we can estimate the excess area contained in the protrusions in the initial stages of the experiment from the FI of the bilayer in an adhered region, shown in Fig. 6.7c. Indeed, an uptake of cholesterol will dilute the labeled lipids in the bilayer, and assuming the area fraction of cholesterol is uniformly distributed and that the bilayer is inextensible, we can estimate the excess area as $\Delta a \approx FI_0/FI - 1$. From the initial drop of FI, we estimate the excess area due to cholesterol adsorption

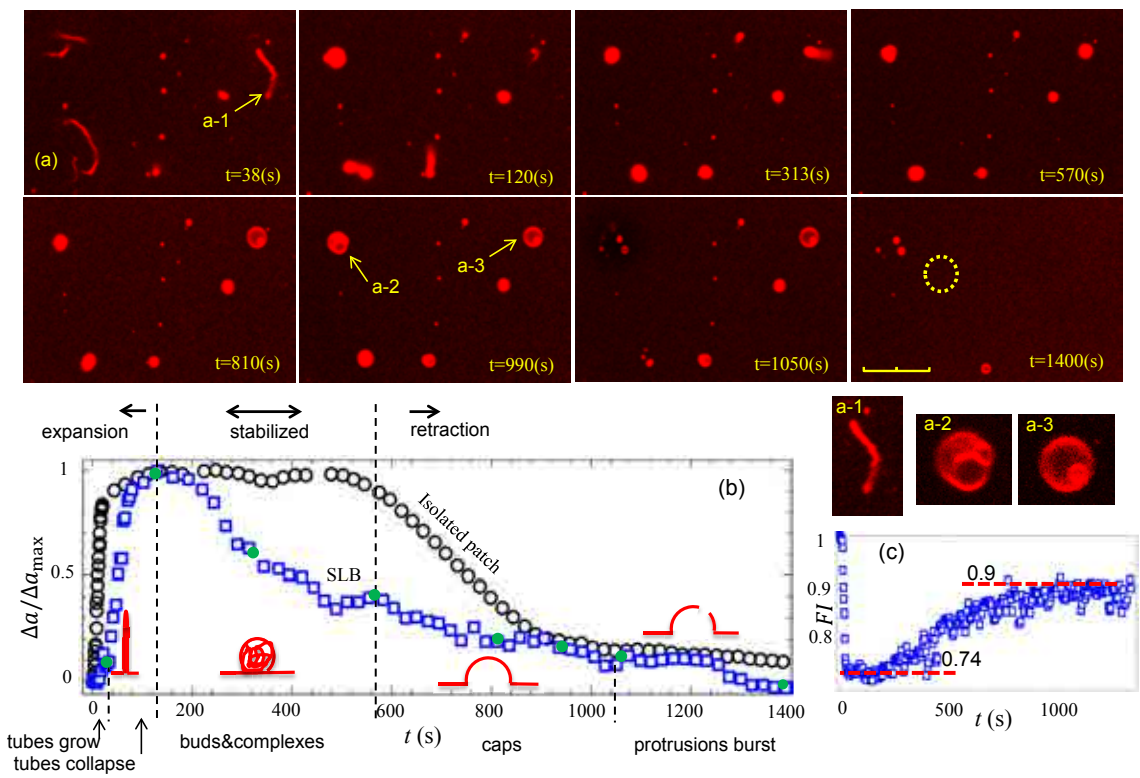

Figure 6.7: (a) Microscope snapshots of a continuous SLB, washed with a 10 mg/mL solution of MβCD-Chol. Tubes nucleate and grow (0-40 s), and then start thickening and snapping to spherical complexes and vesicle aggregates, while they are still growing in size (40-120 s). After that, spherical protrusions are relatively stable, only slightly decreasing in size (120-570 s). Decreasing their area to enclosed volume ratio, spherical protrusions then transform into shallow caps (570-1050 s), which lyse and reorganize into small vesicles (1050 s to the end). Scale-bar: 10 µm. (b) Normalized projected area of the protrusions out of the adhered membrane $\Delta a_{\mathrm{p}}/\Delta a_{\mathrm{p,max}}$ (squares). To compare the continuous SLB reorganization with the expansion/retraction mechanisms of isolated patches, the normalized area deviation of an isolated patch washed with the same solution is plotted (circles). Solid green circles indicate the snapshots in (a). (c) Average FI of an adhered region of the bilayer (the circular region shown in the last snapshot). We attribute the initial drop in intensity to the formation of protrusions, and the subsequent recovery to the condensing effect of cholesterol. The intensity does not recover completely due to loss of phospholipids, either during the reorganization of the protrusions or by DOPC uptake by free MβCD.

as $\Delta a = 0.35$, in agreement with the measured area expansion of an SLB patch, around 30% (see 6.2c for 10 mg/mL MβCD-Chol).

Upon the membrane exposure to the cholesterol solution, the tubes nucleate, rapidly grow, and suddenly collapse to spherical protrusions under a very high negative pressure (larger in the chamber than in the interstitial space). From our previous study on continuous SLBs (chapter 5), we expect that under such a large and fast compressive strain (above 30%) and isosmotic conditions, the system will produce long and very thin tubular protrusions, under a very high negative pressure (larger in the chamber than in the interstitial space), which are prone to brutal collapse into complexes of different topology. Consistently with these previous observations, here the thin tubes either inflate (possibly through holes in the supported bilayer) and collapse into vesicle aggregates, or collapse and the resulting complexes inflate. At a longer time, the excess area gradually contracts. Therefore, the excess area to enclosed volume ratio decreases, and consequently the protrusions transform into shallow caps, in agreement with observations in previous chapter. As the area to volume ratio further decreases, the spherical protrusions become significantly tense, lyse, expel part of their volume, and reorganize into smaller vesicles.

As for isolated patches, we attribute the contraction of the excess area to membrane condensing induced by cholesterol, and to the tendency of free cyclodextrin to deplete the membrane. Additionally, lipids may leave the SLB during the various reorganizations reported above. Fig. 6.7c shows that after the expansion stage, the FI partially recovers by about 16%, reflecting the retraction of DOPC molecules to the adhered bilayer due to the membrane condensation. The final lost in FI (about 10%) results from phospholipid depletion, including the effect of free cyclodextrin.

6.2.5 Confined giant vesicles

We perform further experiments to investigate the effects of cholesterol delivery to GUVs. We choose a highly flaccid GUV, to facilitate its stabilization on the substrate by providing a high adhered area. Compared to the planar adhered bilayers, a GUV

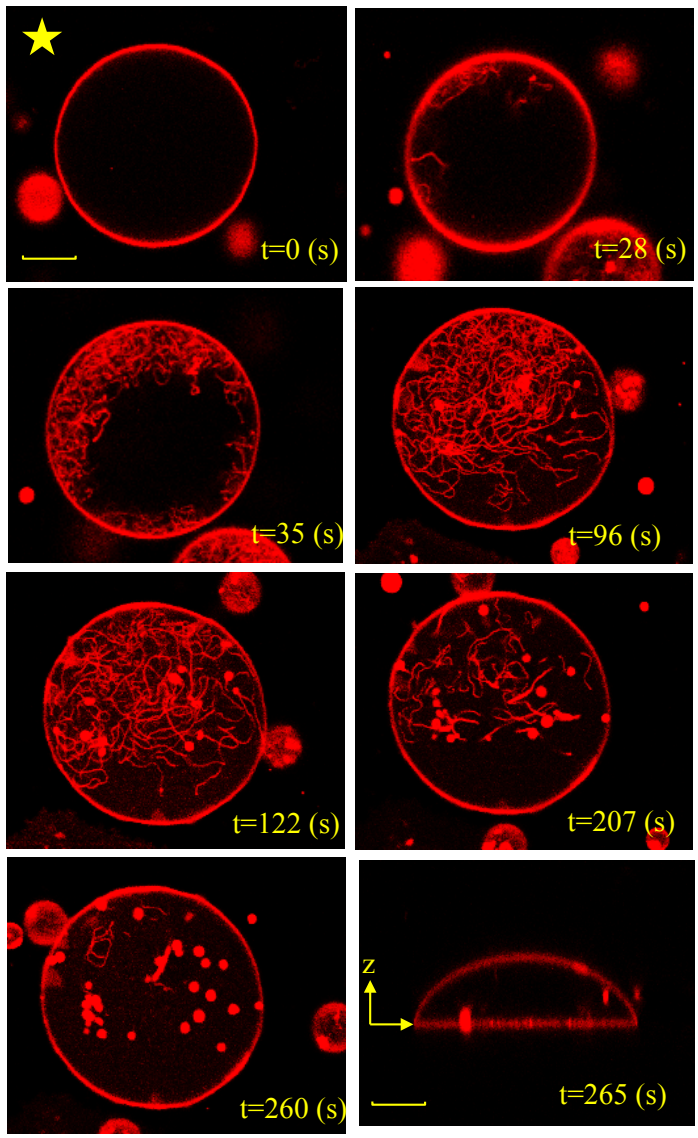

Figure 6.8: Shape transformations of a GUV upon the elevation of the membrane cholesterol. 4 µL of 50 mg/mL solution of MβCD-Cho is injected by a syringe in the vicinity of the GUV (syringe tip location is shown by the star symbol). The tubes nucleate and grow from the non-adhered part and then from the adhered part of the membrane by a few seconds delay. After $\approx$ 100 s the tubes start thickening and retracting to small vesicles. The last microscope snapshot is representing a vertical cross section of the GUV, presenting its adhesion to the substrate. Some vesicles are detached from the membrane and aggregate on the top of the GUV. Scale-bar: 15 µm.

siting on the substrate mimics the cell geometry and size, in addition to the cell confinement and adhesion. We note that in these experiments, the adhesion energy γ is significantly lower, which prevents adhesion from bursting the GUVs. We inject about 4 µL of 50 mg/mL MβCD-Chol solution in the vicinity of the GUV. As shown in Fig. 6.8, upon the cholesterol delivery to the membrane, we observe the formation and growth of inward tubes, stable for a few minutes. We find that such invaginations retract or collapse to spherical aggregates. These shape transformations resemble those observed in continuous SLBs. However, here the tubes are thicker and they stay stable for longer times.

A number of related vesicle systems have been shown to form in or outward tubular protrusions, such as tube formations after the polymer solution inside the vesicles separates into two aqueous phases [Dimova and Lipowsky, 2012], or upon the adsorption of anchored amphiphilic molecules [Tsafrir et al., 2003]. Let us discuss first why the tubes are inwards. From elementary tube mechanics, the total elastic energy of a tube is given by

$$\Pi = \frac{2\pi r L \kappa}{2}\left(\frac{1}{r} - C_0\right)^2 + 2\pi r L\sigma - \pi r^2 L p + fL,$$

where p is the difference of the pressure inside and outside of the tube ($p_{in} - p_{out}$), σ is the surface tension, and C_0 is the possibly cholesterol-induced spontaneous curvature. Minimizing the above relation respect to r, and L, the equilibrium state can be expressed as

$$p = -\frac{\kappa}{2r_0^3} + \frac{2\sigma + \kappa C_0^2}{2r_0},$$

and

$$f = -\frac{\kappa}{2r_0} - \left(\sigma + \frac{\kappa}{2}C_0^2\right) + \frac{pr^2}{2} + \kappa C_0.$$

For a freestanding tube we set $f = 0$, and combining the the above equations, the pressure jump reads

$$p = \frac{2\kappa}{r^2}\left(C_0 - \frac{1}{r}\right).$$

As expected, the above equation shows that for $C_0 < 1/r$, freestanding tubes are stable

under negative pressure (larger in the outside of the tube). Here, the flaccid GUVs are strongly adhered to the substrate, making them tense and pressurized [Bernard et al., 2000]. Consequently, inward tubes satisfy the negative pressure requirement, in contrast with an unsupported flaccid vesicle, for which we expect outward tubes [Lipowsky, 2013]. At longer times, due to the added area, the vesicle has the tendency to further spread, relaxing part of its pressure. This explains the slow thickening and retraction of the tubes. We also observe that some spherical protrusions detach from the GUV and aggregate on the top of the vesicle, reminiscent of the aggregation of lipid droplets in foam cells.

6.3 Summary

We conclude that cholesterol has a high tendency to be incorporated into lipid bilayers, leading to the membrane spreading. In agreement with in-vivo experiments, we also show that the membrane confinement and adhesion are essential to observe membrane protrusions. The membrane confinement coupled with a significant area expansion, results in severe morphological and topological changes in membrane, including the formation of vesicular/tubular protrusions, vesicle aggregates and their transformations. We believe that dynamical membrane reorganizations observed in our experiments can help us to increase our knowledge in similar cellular processes, due to the cholesterol elevation. We also show in this work that SLB patches are very simple model systems, which allow us to study the chemical and mechanical response of membranes to adsorbing molecules and surfactants.

Chapter 7

Thermal fluctuations of highly curved membranes

Biomembranes are highly flexible structures, which exhibit noticeable thermal undulations in common conditions. The analysis of fluctuations provides a means of measuring equilibrium mechanical parameters such as the bending stiffness, the membrane tension, or the spontaneous curvature, for instance by coupling phase contrast video microscopy with theoretical continuum models of membrane undulations, in what is known as flickering spectroscopy [Milner and Safran, 1987, Duwe et al., 1990, Döbereiner et al., 2003]. The dynamics of biomembranes can also be studied using these optical methods, or other techniques such as Neutron Spin Echo (NSE) [Arriaga et al., 2010], probing much smaller length and time scales, which have revealed the role of inter-monolayer friction in the relaxation dynamics of fluctuations [Seifert and Langer, 1993, Pott and Meleard, 2002, Rodríguez-García et al., 2009], as well as the role of membrane viscosity for fluctuations of nanometric wavelengths [Watson and Brown, 2010]. Besides their utility in measurements of equilibrium and dynamical properties of bilayers, fluctuations are thought to mediate in biological processes, e.g. in the way cells probe their environment [Pierres et al., 2009], or in the mobility of proteins on membranes [Brown, 2003].

Predictive continuum models, e.g. [Seifert and Langer, 1993] for planar geometries and recently confirmed by molecular simulations [Shkulipa et al., 2006] or [Yeung and Evans, 1995, Seifert, 1997, Sevšek, 2010] for spherical geometries, are pivotal in such

studies to properly interpret observations, which may be qualified as anomalous if viewed through an incomplete theory [Watson and Brown, 2010, Arriaga et al., 2010].

Mathematical formulations of interfacial flows on general geometries shows that, in the presence of curvature, the membrane (interfacial) viscosity produces a normal drag force, quadratic in the curvature and linear in the normal velocity [Arroyo and DeSimone, 2009]. For small fluctuations about planar configurations, such a normal force vanishes, and the membrane viscosity is coupled only to tangential velocities. This results in a negligible effect on the dynamics, except for very short wavelengths close to the membrane thickness [Seifert and Langer, 1993], only accessible to NSE spectroscopy.

We show in the present chapter that the membrane viscosity can play a crucial role in the fluctuations of vesicular or tubular membranes whose radii are comparable to, or below the Saffman-Delbrück length scale (the ratio between the membrane surface viscosity and the solvent bulk viscosity). We note that the observations of thermal fluctuations of highly curved membranes have remained limited, due to the resolution of available optical measurements. However, experimental techniques can improve, and we further suggest experiments on tubular membranes, where our predictions could be checked with common techniques.

It is also worth noting that highly curved membrane structures are very common in cells. For example, lysosomes and peroxisomes have spherical shapes, mitochondria form a tubular network, the endoplasmic reticulum is an interconnected system of sheets and tubules, and the Golgi apparatus consists of a stack of perforated sheets [Shibata et al., 2009]. In addition, membrane tethers, such as recently observed cell-to-cell communicating tubes [Rustom et al., 2004] are ubiquitous structures in cells. Understanding the physics of the ever-present thermal fluctuations on such structures may have biological implications.

In addition to the potentially important role of membrane viscosity in the undulations of subcellular structures, this often disregarded effect is the dominant dissipative mechanism in polymersomes (with a Saffman-Delbrück length scale around millimeters), which have been recently probed by flickering spectroscopy [Rodríguez-García

et al., 2011]. A correct interpretation of dynamic measurements requires incorporating the effect of membrane viscosity into the theory.

Here, we determine the relaxation dynamics and the shape fluctuations of quasi-spherical vesicles and tubular membranes, by using the continuum formulations presented in chapter 2, and available analytical solutions for hydrodynamics around cylindrical and spherical shapes [Happel and Brenner, 1965]. We examine the effect of the membrane viscosity on dynamical relaxation rates (i.e. eigenvalues of the linearized system) of thermally excited spherical and tubular membranes of different sizes.

7.1 Vesicular membranes

7.1.1 Kinematics

We parametrize the midsurface of the vesicle Γ_t at a given time t, in spherical coordinates,

$$\boldsymbol{x}(\varphi,\theta;t) = R(\varphi,\theta;t)\hat{\boldsymbol{e}}_r = R(\varphi,\theta;t)\{\sin\varphi\cos\theta, (\varphi,\theta;t)\sin\varphi\sin\theta, (\varphi,\theta;t)\cos\varphi\},$$

where $\varphi \in [0,\pi)$, $\theta \in [0,2\pi)$, and $\hat{\boldsymbol{e}}_r = (\partial\boldsymbol{x}/\partial R)/|\partial\boldsymbol{x}/\partial R|$, $\hat{\boldsymbol{e}}_\theta = (\partial\boldsymbol{x}/\partial\theta)/|\partial\boldsymbol{x}/\partial\theta|$, $\hat{\boldsymbol{e}}_\varphi = (\partial\boldsymbol{x}/\partial\varphi)/|\partial\boldsymbol{x}/\partial\varphi|$ are basis unit vectors in spherical coordinates. Given that, we calculate the metric tensor $g_{ij} = \boldsymbol{x}_i \cdot \boldsymbol{x}_j$, and the normal vector $\boldsymbol{n} = \boldsymbol{x}_i \times \boldsymbol{x}_j/|\boldsymbol{x}_i \times \boldsymbol{x}_j|$, (where $\boldsymbol{x}_i = \partial_i\boldsymbol{x}$, $i = \varphi,\theta$), as

$$\boldsymbol{g} = \begin{bmatrix} R_\varphi^2 + R^2 & R_\varphi R_\theta \\ R_\varphi R_\theta & {R_\theta}^2 + R^2\sin^2\varphi \end{bmatrix},$$

$$\boldsymbol{n} = \frac{R\sin\varphi\ \hat{\boldsymbol{e}}_r - R_\varphi\sin\varphi\ \hat{\boldsymbol{e}}_\varphi - R_\theta\ \hat{\boldsymbol{e}}_\theta}{\sqrt{\left({R_\varphi}^2 + R^2\right)\sin^2\varphi + {R_\theta}^2}}.$$

We note that the surface element can be expressed as $dA = Jd\varphi d\theta$, where the Jacobian is given by $J = \sqrt{\det(g)} = R^2 \sin\varphi \sqrt{1 + |\boldsymbol{\nabla}_s R|^2}$, where $\boldsymbol{\nabla}_s$ denotes the surface gradient. Also introducing the curvature tensor, $h_{ij} = (\partial_i \partial_j \boldsymbol{x}) \cdot \boldsymbol{n}$, one can write twice of the mean curvature as $2H = -h^i_i$, and the Gaussian curvature $K = \det(h^i_j)$, where $h^i_j = g^{ik} h_{kj}$ and g^{ij} are the components of $\boldsymbol{g}^{-1}$. In addition, the surface Laplacian, surface gradient and its norm in spherical coordinates are given by

$$\boldsymbol{\nabla}_s^2 R = \frac{1}{R^2 \sin^2\varphi} \left(R_{\theta\theta} + R_\varphi \sin\varphi \cos\varphi + R_{\varphi\varphi} \sin^2\varphi \right),$$

$$\boldsymbol{\nabla}_s R = \frac{1}{R \sin\varphi} \left(R_\theta \hat{\boldsymbol{e}}_\theta + R_\varphi \sin\varphi \hat{\boldsymbol{e}}_\varphi \right),$$

and

$$|\boldsymbol{\nabla}_s R|^2 = \frac{1}{R^2 \sin^2\varphi} \left(R_\theta^2 + R_\varphi^2 \sin^2\varphi \right).$$

Here, we consider a quasi spherical fluctuating vesicle, i.e. a vesicle whose radius, and density deviates about those of a spherical equilibrium state

$$\begin{aligned} R(\varphi,\theta) &= R_0 + h(\varphi,\theta), \\ \rho(\varphi,\theta) &= \rho_0 + \delta\rho(\varphi,\theta), \\ \bar{\rho}(\varphi,\theta) &= \bar{\rho}_0 + \delta\bar{\rho}(\varphi,\theta), \end{aligned} \tag{7.1}$$

where $\rho = (\rho^+ - \rho^-)/2\rho_0$, $\bar{\rho} = (\rho^+ + \rho^-)/2\rho_0$, and by $\rho^\pm$ we denote the density field of each monolayer, projected on the bilayer midsurface. We express the radial deviation h, as well as the density deviations $\delta\rho$, $\delta\bar{\rho}$, using scalar spherical harmonics (SSH)

[MacRobert, 1928] as

$$\begin{aligned} h(t,\varphi,\theta) &= \sum_{n,m} h_{nm}(t) Y_{nm}(\varphi,\theta), \\ \delta\rho(t,\varphi,\theta) &= \sum_{n,m} \rho_{nm}(t) Y_{nm}(\varphi,\theta), \\ \delta\bar{\rho}(t,\varphi,\theta) &= \sum_{n,m} \bar{\rho}_{nm}(t) Y_{nm}(\varphi,\theta), \end{aligned}$$

where

$$\sum_{n,m} = \sum_{n=0}^{n_{max}} \sum_{m=-n}^{n},$$

and, Y_{nm} is called a spherical harmonic function of degree n and order m, an *associated Legendre polynomial*. We note that in general the amplitudes of the SSHs are complex numbers.

7.1.2 Elastic energy

We rewrite the total elastic energy of a bilayer membrane, including the bending energy and the stretching energy together with work of pressure and tension

$$\begin{aligned} \Pi &= \frac{\tilde{\kappa}}{2}\int_\Omega 2H^2 \,\mathrm{d}A + K_s \int_\Omega \bar{\rho}^2 \,\mathrm{d}A + K_s \int_\Omega \rho^2 \,\mathrm{d}A - 4dK_s \int_\Omega \rho H \,\mathrm{d}A \\ &\quad + \gamma^{\pm}\left[\int_\Omega (\bar{\rho} \pm \rho + 1) \,\mathrm{d}A - A_0^{\pm}\right] - p\left(\int_\Omega \mathrm{d}V - V_0\right), \end{aligned} \tag{7.2}$$

where $\tilde{\kappa} = \kappa + 2d^2K_s$, and $A_0^{\pm}$ denotes the equilibrium area of each monolayer containing a given number of lipids, and V_0 denotes the enclosed volume. Note that the spontaneous curvature is neglected and the last two terms can be either interpreted as lipid and volume constraints, i.e. $\gamma^{\pm}$ and p are Lagrange multipliers, or as the work of tension and pressure. The signs are such that a positive surface tension $\gamma^{\pm}$ tends to expand the surface area, and $p = p_{\text{int}} - p_{\text{out}}$.

Now, we express the total elastic energy of a fluctuating quasi spherical vesicle, by

linearizing the elastic energy about a spherical equilibrium state. To find this initial equilibrium state, we rewrite equation 7.2 for a sphere of radius R_0, density average $\bar{\rho} = \bar{\rho}_0$, and density deviation $\rho = \rho_0$,

$$\Pi = 8\pi\tilde{\kappa}R_0^2 + 4\pi R_0^2\left[K_s\bar{\rho}_0^2 + K_s\rho_0^2 + \bar{\gamma}\left(\bar{\rho}_0 + 1\right) + \gamma\rho_0\right] - 16dK_s\pi R_0\rho_0 - \frac{4\pi R_0^3}{3}p,$$

where $\bar{\gamma} = \gamma^+ + \gamma^-$, and $\gamma = \gamma^+ - \gamma^-$. Making Π stationary to find equilibria, we have

$$\begin{aligned}
0 &= \frac{\partial\Pi}{\partial\rho_0} = 4\pi R_0^2\left(\gamma - 4dK_s/R + 2K_s\rho_0\right)\\
0 &= \frac{\partial\Pi}{\partial\bar{\rho}_0} = 4\pi R_0^2\left(\bar{\gamma} + 2K_s\bar{\rho}_0\right)\\
0 &= \frac{\partial\Pi}{\partial R_0} = 8\pi R_0\left[K_s\bar{\rho}_0^2 + K_s\rho_0^2 + \bar{\gamma}\left(\bar{\rho}_0 + 1\right) + \gamma\rho_0\right] - 16dK_s\pi\rho_0 - 4\pi R_0^2 p
\end{aligned}$$

The first and the second equations result in membrane tensions $\gamma = -2K_s\rho_0 + 4dK_s/R_0$, and $\bar{\gamma} = -2K_s\bar{\rho}_0$. From the third equation we derive the pressure jump required for such a prescribed sphere,

$$p = \frac{2}{R_0}\left(-K_s\bar{\rho}_0^2 - K_s\rho_0^2 - 2K_s\bar{\rho}_0 + \frac{2dK_s\rho_0}{R}\right).$$

We note that for general choices of R_0, $\bar{\rho}_0$, ρ_0 (or $A_0^{\pm}$, and V_0) this equilibrium state is not necessarily stable, particularly if $\bar{\rho}_0$ is positive, i.e. a deflated vesicle. In the following, we fix $\bar{\rho}_0 = 0$, $\rho_0 = 2d/R_0$, which results in $\gamma = \bar{\gamma} = p = 0$.

Using the expressions in appendix D.1, we express the total elastic energy by retaining up to second order terms as

$$\Pi = \sum_{n,m}\pi_{nm},$$

where

$$\pi_{nm} = \frac{1}{2}\mathbf{y}_{nm}^T \underbrace{\begin{pmatrix} K_{11} & K_{12} & K_{13} \\ K_{12} & K_{22} & 0 \\ K_{13} & 0 & K_{22} \end{pmatrix}}_{\mathbf{E}_{nm}} \mathbf{y}_{nm}^* \tag{7.3}$$

where

$$\begin{aligned} K_{11} &= \tilde{\kappa}\left(\xi_n^2 - 2\xi_n\right)/R_0^2 + K_s\hat{\rho}_0(\xi_n + 2) - 4dK_s\rho_0\xi_n/R_0 + pR_0, \\ K_{12} &= 2R_0\left(2K_s\bar{\rho}_0 + \bar{\gamma}\right), \\ K_{13} &= 2R_0\left(2K_s\rho_0 + \gamma\right) - 2dK_s\left(\xi_n + 2\right), \\ K_{22} &= 2K_sR_0^2, \\ \mathbf{y}_{nm} &= \begin{pmatrix} h_{nm} & \bar{\rho}_{nm} & \rho_{nm} \end{pmatrix}^T, \\ \xi_n &= n\left(n+1\right), \end{aligned}$$

and by $*$ we denote the complex transpose of a vector or matrix. For the equilibrium state given by $\bar{\rho}_0 = 0$, $\rho_0 = 2d/R_0$, and $\gamma = \bar{\gamma} = p = 0$, the above relations can be simplified as

$$K_{11} = \tilde{\kappa}\left(\xi_n^2 - 2\xi_n\right)/R_0^2 + 4d^2K_s(2 - \xi_n)/R_0^2, \quad K_{12} = 0, \quad K_{13} = 2dK_s(2 - \xi_n).$$

Using the equipartition theorem, we have

$$\langle \mathbf{y}_{nm}\mathbf{y}_{nm}^* \rangle = K_bT\mathbf{E}_{nm}^{-1}, \tag{7.4}$$

where by $\langle\rangle$ we denote the ensemble average, or time average under the assumption of ergodicity. We note that this relation provides a connection between the theory and spectra measurable in experiments, and allows us to estimate the bending stiffness or the membrane tension. We also calculate the rate of the change of the elastic work in

the following form, which will be used later in governing equations,

$$\dot{\Pi} = \sum \mathbf{y}_{nm}^{T} \mathbf{E}_{nm} \dot{\mathbf{y}}_{\mathbf{nm}}^{*} \tag{7.5}$$

7.1.3 Dissipation

Shape transformations of lipid bilayers are dragged by various dissipative mechanisms, being the bulk fluid dissipation, interfacial membrane dissipation and the dissipation due to interlayer friction, the most important ones.

Interfacial viscous dissipation

The interfacial viscous dissipation potential for one monolayer is expressed in Eq. (2.13) and can be written in the following form, which is useful for further calculations (see [Arroyo et al., 2012] for the derivation of W_{μ_s}) ,

$$\begin{aligned} W_{\mu_s}[\boldsymbol{v}, v_n] = \quad & \int_\Gamma \mu_s \Bigg[\frac{1}{2} |\boldsymbol{\nabla}_s \times \boldsymbol{v}|^2 + (\boldsymbol{\nabla}_s \cdot \boldsymbol{v})^2 - K|\boldsymbol{v}|^2 \\ & + (4H^2 - 2K) v_n^2 + 2(\boldsymbol{\nabla}_s \boldsymbol{v} : \boldsymbol{h}) v_n \Bigg] \mathrm{d}S, \end{aligned} \tag{7.6}$$

$$W_{\lambda_s}[\boldsymbol{v}, v_n] = \int_\Gamma \frac{\lambda_s}{2} \left[(\boldsymbol{\nabla}_s \cdot \boldsymbol{v})^2 + 4H^2 v_n^2 - 4H (\boldsymbol{\nabla}_s \cdot \boldsymbol{v}) v_n \right] \mathrm{d}S. \tag{7.7}$$

Note that around a planar state [Seifert and Langer, 1993], or for a fixed geometry [Henle and Levine, 2010], the second line in Eq. (7.6) vanishes, as often considered. We need to calculate the dissipation potential for spherical shapes, where we express the membrane velocity as

$$\boldsymbol{V}(\varphi, \theta; t) = v_r \hat{\boldsymbol{e}}_r + v_\varphi \hat{\boldsymbol{e}}_\varphi + v_\theta \hat{\boldsymbol{e}}_\theta, \tag{7.8}$$

For small membrane deformations, we have $\boldsymbol{n} \approx \hat{\boldsymbol{e}}_r$, which results in $v_n = v_r = \dot{h}$, and tangential velocity $\boldsymbol{v} = v_\varphi \hat{\boldsymbol{e}}_\varphi + v_\theta \hat{\boldsymbol{e}}_\theta$.

We use vector spherical harmonics (VSHs) to express the velocity field on the membrane [MacRobert, 1928, Barrera et al., 2000]

$$\boldsymbol{V}(\varphi,\theta;t)=\sum_{n,m}\left(v_{nm}^{r}\boldsymbol{Y}_{nm}+v_{nm}^{(1)}\boldsymbol{\Psi}_{nm}+v_{nm}^{(2)}\boldsymbol{\Phi}_{nm}\right). \tag{7.9}$$

where $\boldsymbol{Y}_{nm}=Y_{nm}\hat{\boldsymbol{e}}_r$, $\boldsymbol{\Psi}_{nm}=R_0\boldsymbol{\nabla}_s Y_{nm}$, and $\boldsymbol{\Phi}_{nm}=\hat{\boldsymbol{e}}_r\times\boldsymbol{\Psi}_{nm}$. The tangential velocity can be written as

$$\boldsymbol{v}=\sum_{n,m}\boldsymbol{v}_{nm}=\sum_{n,m}v_{nm}^{(1)}\boldsymbol{\Psi}_{nm}+v_{nm}^{(2)}\boldsymbol{\Phi}_{nm}.$$

Taking the advantage of the VSH orthogonality (see appendix D.2), and recalling the expressions given in appendix D.2, we can write the interfacial viscous dissipation functional as

$$W_{\mu_s}^{\pm}+W_{\lambda_s}^{\pm}=\frac{1}{2}\sum {\boldsymbol{V}_{nm}^{\pm}}^{*}\begin{pmatrix}D_{rr}&D_{r1}&0\\D_{r1}&D_{11}&0\\0&0&D_{22}\end{pmatrix}\boldsymbol{V}_{nm}^{\pm},$$

where ${\boldsymbol{V}_{nm}^{\pm}}^{T}=\begin{pmatrix}v_{nm}^{r}&v_{nm}^{(1)\pm}&v_{nm}^{(2)\pm}\end{pmatrix}$, and $D_{rr}=4\mu_s+2\lambda_s$, $D_{r1}=-2\xi_n\mu_s+\xi_n\lambda_s$, $D_{11}=2\xi_n(\xi_n-1)\mu_s+\xi_n^2\lambda_s$, $D_{22}=\xi_n(\xi_n-2)\mu_s$. Interestingly, we observe that the interfacial viscosity dissipation potential does depend on the normal velocities through the term D_{rr}, contrary to the usual assumption derived from the linearization about a planar state.

Interlayer friction

We also express the Rayleigh dissipation potential for interlayer friction using VSHs as

$$\begin{aligned} W_{bm}[\boldsymbol{v}^{\pm}] &= \frac{b_m}{2}\int_{\Omega}\|\boldsymbol{v}^{+}-\boldsymbol{v}^{-}\|^2\,\mathrm{d}S \\ &= \frac{b_m}{2}\sum\left((v_{nm}^{(1)+}-v_{nm}^{(1)-})^2+(v_{nm}^{(2)+}-v_{nm}^{(2)-})^2\right)\xi_n, \end{aligned} \tag{7.10}$$

Bulk fluid dissipation

In this section, we follow [Happel and Brenner, 1965] to account for the effect of a surrounding Newtonian fluid and solve the Stokes equations in the inner and outer domains delimited by a sphere. Denoting by μ_b the bulk fluid shear viscosity, the equation of balance of linear momentum for an incompressible Newtonian fluid is

$$\boldsymbol{\nabla}^2\boldsymbol{V}^b=\frac{1}{\mu_b}\boldsymbol{\nabla}p \tag{7.11}$$

where V^b denotes the bulk fluid velocity field, and p denotes the pressure field. Taking the divergence of the above equation and recalling the continuity equation ($\boldsymbol{\nabla}\cdot V^b=0$), we obtain the Laplace equation for pressure

$$\boldsymbol{\nabla}^2 p=0.$$

This suggests expanding the pressure field in a series of solid spherical harmonics

$$p=\sum_{n=-\infty}^{\infty}p_n,$$

where p_n is a solid spherical harmonic of order n ($R^n Y_{nm}$). From this expansion, one can find Lamb's general solution

$$\boldsymbol{V}^b(R,\varphi,\theta) = \sum_{n=-\infty}^{\infty} \Bigg[\boldsymbol{\nabla} \times (\chi_n R\hat{\boldsymbol{e}}_r) + \boldsymbol{\nabla}\Phi_n \;+\; \frac{n+3}{2\mu_b(n+1)(2n+3)} R^2 \boldsymbol{\nabla} p_n \\ -\; \frac{n}{\mu_b(n+1)(2n+3)} p_n R\hat{\boldsymbol{e}}_r \Bigg]$$

where χ_n and Φ_n are each solid spherical harmonics given below.

Interior of the sphere: The condition that the velocity should remain finite at the origin of the sphere implies that for $n \leq 0$, $p_n = \Phi_n = \chi_n = 0$. For $n \geq 1$ we have [Happel and Brenner, 1965],

$$\begin{aligned} p_n &= \frac{\mu_b(2n+3)}{n} \frac{1}{R_0} \left(\frac{R}{R_0}\right)^n [\Upsilon_n - (n-1)\Theta_n] \\ \Phi_n &= \frac{1}{2n} R_0 \left(\frac{R}{R_0}\right)^n [(n+1)\Theta_n - \Upsilon_n] \\ \chi_n &= \frac{1}{n(n+1)} \left(\frac{R}{R_0}\right)^n Z_n \end{aligned} \tag{7.12}$$

where $\Theta_n(\varphi,\theta)$, $\Upsilon(\varphi,\theta)$, $Z_n(\varphi,\theta)$ are SSHs defined on the surface, known from the prescribed velocity field on the inner surface of the sphere $\boldsymbol{V}^-$ as

$$\begin{aligned} \sum_{n=1}^{\infty} \Theta_n &= \hat{\boldsymbol{e}}_r \cdot \boldsymbol{V}^- \quad &\Rightarrow\quad \Theta_n &= \sum_{m=-n}^{n} v_{nm}^r Y_{nm} \\ \sum_{n=1}^{\infty} \Upsilon_n &= -R\boldsymbol{\nabla} \cdot \boldsymbol{V}^- \quad &\Rightarrow\quad \Upsilon_n &= \sum_{m=-n}^{n} \left(-2v_{nm}^r + n(n+1)v_{nm}^{(1)-}\right) Y_{nm} \\ \sum_{n=1}^{\infty} Z_n &= R\hat{\boldsymbol{e}}_r \cdot \boldsymbol{\nabla} \times \boldsymbol{V}^- \quad &\Rightarrow\quad Z_n &= \sum_{m=-n}^{n} -n(n+1)v_{nm}^{(2)-} Y_{nm} \end{aligned} \tag{7.13}$$

Exterior of the sphere: Now the velocity is required to vanish at infinity, which restricts the expansion to the solid spherical harmonics with negative order ($R^{-n-1}Y_{nm}$).

Thus n is replaced by $-(n+1)$. With the prescribed boundary conditions, we ultimately obtain the solution

$$\begin{aligned} p_{-(n+1)} &= \frac{\mu_b(2n-1)}{n+1}\frac{1}{R_0}\left(\frac{R_0}{R}\right)^{n+1}[\Upsilon_n + (n+2)\Theta_n] \\ \Phi_{-(n+1)} &= \frac{1}{2(n+1)}R_0\left(\frac{R_0}{R}\right)^{n+1}[n\Theta_n + \Upsilon_n] \\ \chi_{-(n+1)} &= \frac{1}{n(n+1)}\left(\frac{R_0}{R}\right)^{n+1} Z_n \end{aligned} \tag{7.14}$$

The functions $\Theta_n(\varphi,\theta)$, $\Upsilon(\varphi,\theta)$, $Z_n(\varphi,\theta)$ are determined as above.

Bulk fluid traction on the sphere: The traction exerted by the internal and external bulk Newtonian fluids onto the spherical membrane can be computed as

$$\boldsymbol{t}^{b\pm} = \pm\hat{\boldsymbol{e}}_r \cdot \boldsymbol{\sigma}^{b\pm} = \pm\left[-p\hat{\boldsymbol{e}}_r + \mu_b\left(\frac{\partial \boldsymbol{V}^b}{\partial R} - \frac{\boldsymbol{V}^b}{R}\right) + \frac{\mu_b}{R}\boldsymbol{\nabla}(R\hat{\boldsymbol{e}}_r \cdot \boldsymbol{V}^b)\right]^{\pm}$$

where $\boldsymbol{\sigma}^{b\pm}$ denotes the stress tensor of the bulk internal and external fluids evaluated at the membrane. The inner fluid exerts the following traction on the inner monolayer,

$$\begin{aligned} \boldsymbol{t}^{b-} = \quad & -\frac{\mu_b}{R}\sum_{n=1}^{\infty}\Bigg[(n-1)\boldsymbol{\nabla}\times(\chi_n R\hat{\boldsymbol{e}}_r) + 2(n-1)\boldsymbol{\nabla}\Phi_n \\ & -\frac{2n^2+4n+3}{\mu_b(n+1)(2n+3)}p_n R\hat{\boldsymbol{e}}_r + \frac{n(n+2)}{\mu_b(n+1)(2n+3)}R^2\boldsymbol{\nabla}p_n\Bigg] \end{aligned} \tag{7.15}$$

while for the outer fluid we have,

$$\begin{aligned}\boldsymbol{t}^{b+} = \quad & \frac{\mu_b}{R}\sum_{n=1}^{\infty}\Big[(n-1)\boldsymbol{\nabla}\times(\chi_n R\hat{\boldsymbol{e}}_r) \\ & +2(n-1)\boldsymbol{\nabla}\Phi_n - \frac{2n^2+4n+3}{\mu_b(n+1)(2n+3)}p_n R\hat{\boldsymbol{e}}_r \\ & +\frac{n(n+2)}{\mu_b(n+1)(2n+3)}R^2\boldsymbol{\nabla}p_n\Big]_{n=-(n+1)}\end{aligned} \tag{7.16}$$

Inserting equations 7.12-7.14 into the above relation, we obtain

$$\boldsymbol{t}^{b\pm} = \mu_b\sum_{n,m}\left[\begin{array}{ccc}\boldsymbol{Y}_{nm} & \boldsymbol{\Psi}_{nm} & \boldsymbol{\Phi}_{nm}\end{array}\right]\mathbf{T}^{\pm}\boldsymbol{V}^{\pm}_{nm}$$

where

$$\mathbf{T}^{+} = \begin{bmatrix} -(2n^2+3n+4)/[(n+1)R_0] & 3n/R_0 & 0 \\ 3/[(n+1)R_0] & -(2n+1)/R_0 & 0 \\ 0 & 0 & -(n+2)/R_0 \end{bmatrix}$$

and

$$\mathbf{T}^{-} = -\begin{bmatrix} (2n^2+n+3)/(nR_0) & -3(n+1)/R_0 & 0 \\ -3/(nR_0) & (2n+1)/R_0 & 0 \\ 0 & 0 & (n-1)/R_0 \end{bmatrix}.$$

Bulk fluid dissipation potential: Collecting the results above, we find

$$W_{\mu_b} = -\frac{1}{2}\int_{\Gamma}\boldsymbol{t}^{b\pm}\cdot\boldsymbol{V}^{\pm}\,\mathrm{d}S = \frac{1}{2}\sum{\boldsymbol{V}^{\pm}_{nm}}^{*}\underbrace{\begin{pmatrix} D^b_{rr} & D^b_{r1} & 0 \\ D^b_{r1} & D^b_{11} & 0 \\ 0 & 0 & D^b_{22}\end{pmatrix}^{\pm}}_{\mathbf{D}^{\mathrm{bulk}\pm}}\boldsymbol{V}^{\pm}_{nm},$$

where

$$\mathbf{D}^{\text{bulk}+} = \mu_b \begin{bmatrix} (2n^2+3n+4)/[(n+1)R_0] & -3n/R_0 & 0 \\ -3n/R_0 & n(2n+1)(n+1)/R_0 & 0 \\ 0 & 0 & n(n+1)(n+2)/R_0 \end{bmatrix}$$

and

$$\mathbf{D}^{\text{bulk}-} = \mu_b \begin{bmatrix} (2n^2+n+3)/(nR_0) & -3(n+1)/R_0 & 0 \\ -3(n+1)/R_0 & n(2n+1)(n+1)/R_0 & 0 \\ 0 & 0 & n(n-1)(n+1)/R_0 \end{bmatrix}.$$

7.1.4 Governing equations

Continuity equation

The continuity equation presented in Eq. (6.6), can be approximated for small density deviations as

$$\frac{1}{\rho_0}\frac{\partial \rho^{\pm}}{\partial t} \approx -\boldsymbol{\nabla}_s \cdot \boldsymbol{v}^{\pm} - v_n H \tag{7.17}$$

Substituting each variable by the SSH expressions and employing Eq. (D.3) we have

$$\underbrace{\begin{pmatrix} \dot{h}_{nm} \\ \dot{\bar{\rho}}_{nm} \\ \dot{\rho}_{nm} \end{pmatrix}}_{\dot{\mathbf{y}}_{nm}} = \underbrace{\begin{pmatrix} 1 & 0 & 0 \\ -2/R_0 & \xi_n/2R_0 & \xi_n/2R_0 \\ 0 & \xi_n/2R_0 & -\xi_n/2R_0 \end{pmatrix}}_{\mathbf{C}_{nm}} \underbrace{\begin{pmatrix} v^r_{nm} \\ v^{(1)+}_{nm} \\ v^{(1)-}_{nm} \end{pmatrix}}_{\boldsymbol{V}_{nm}} \tag{7.18}$$

or

$$\begin{pmatrix} v^r_{nm} \\ v^{(1)+}_{nm} \\ v^{(1)-}_{nm} \end{pmatrix} = \underbrace{\begin{pmatrix} 1 & 0 & 0 \\ 2/\xi_n & R_0/\xi_n & R_0/\xi_n \\ 2/\xi_n & R_0/\xi_n & -R_0/\xi_n \end{pmatrix}}_{\mathbf{C}^{-1}_{nm}} \begin{pmatrix} \dot{h}_{nm} \\ \dot{\bar{\rho}}_{nm} \\ \dot{\rho}_{nm} \end{pmatrix} \tag{7.19}$$

Interestingly, we show that the rate of the radial and density deviations is independent of the second component of the surface velocity $v_{nm}^{(2)}$. Recalling Eq. (7.5), the relations above allow us to express $\dot{\Pi}$ as a function of $\boldsymbol{V}_{nm}$ instead of $\dot{\mathbf{y}}_{nm}$.

Relaxation dynamics

The dynamics of the system can be obtained by minimizing the Rayleigh dissipation potential plus the rate of change of the elastic energy $W^{\text{tot}}[\boldsymbol{V}_{nm}^{\pm}] + \dot{\Pi}[\boldsymbol{V}_{nm}^{\pm}]$ with respect to the variables expressing the rate of change of the system [Goldstein et al., 2001]. The stationarity condition results in

$$\frac{\partial W_{\text{tot}}}{\partial \boldsymbol{V}_{nm}^{*}} = -\frac{\partial \dot{\Pi}}{\partial \boldsymbol{V}_{nm}^{*}},$$

where $W_{\text{tot}} = W_{\mu_b} + W_{\mu_s} + W_{\lambda_s} + W_{b_m}$, and

$$\frac{\partial \dot{\Pi}}{\partial \boldsymbol{V}_{nm}^{*}} = \frac{\partial \dot{\Pi}}{\partial \dot{\mathbf{y}}_{nm}^{*}} \frac{\partial \dot{\mathbf{y}}_{nm}^{*}}{\partial \boldsymbol{V}_{nm}^{*}} = \mathbf{C}_{nm}^{T} \mathbf{E}_{nm} \mathbf{y}_{nm}. \tag{7.20}$$

Therefore the dynamical governing equation can be written as

$$\left(\mathbf{C}_{nm}^{-T} \mathbf{D}_{nm}^{\text{tot}} \mathbf{C}_{nm}^{-1}\right) \dot{\mathbf{y}}_{nm} = -\mathbf{E}_{nm} \mathbf{y}_{nm}.$$

Introducing $\mathbf{M}_{nm} = \mathbf{C}_{nm} \mathbf{D}_{nm}^{\text{tot}\,-1} \mathbf{C}_{nm}^{T} \mathbf{E}_{nm}$, the linearized dynamics becomes

$$\dot{\mathbf{y}}_{nm} = -\mathbf{M}_{nm} \mathbf{y}_{nm} \tag{7.21}$$

We note that $\mathbf{D}^{\text{tot}}_{nm}$ collects all the dissipative components introduced before,

$$\mathbf{D}^{\text{tot}}_{nm} = \begin{pmatrix} 2D_{rr} & D_{r1} & D_{r1} \\ D_{1r} & D_{11} & 0 \\ D_{1r} & 0 & D_{11} \end{pmatrix} + \begin{pmatrix} \left(D^{b-}_{rr} - D^{b+}_{rr}\right) & -D^{b+}_{r1} & D^{b-}_{r1} \\ -D^{b+}_{1r} & -D^{b+}_{11} & 0 \\ D^{b-}_{1r} & 0 & D^{b-}_{11} \end{pmatrix} + \begin{pmatrix} 0 & 0 & 0 \\ 0 & b_m\xi_n & -b_m\xi_n \\ 0 & -b_m\xi_n & b_m\xi_n \end{pmatrix}$$

With the Onsager regression hypothesis, we compute the autocorrelations of membrane fluctuations respect to the initial state,

$$\langle \mathbf{y}_{nm}(t)\mathbf{y}^*_{nm}(0)\rangle = e^{-\mathbf{M}_{nm}t}\langle \mathbf{y}_{nm}(0)\mathbf{y}^*_{nm}(0)\rangle.$$

The diagonal components of the above relation can be written as,

$$\langle \alpha_{nm}(t)\alpha^*_{nm}(0)\rangle = \langle \alpha_{nm}(0)\alpha^*_{nm}(0)\rangle \left(A^\alpha_1 e^{-\gamma_1 t} + A^\alpha_2 e^{-\gamma_2 t} + A^\alpha_3 e^{-\gamma_3 t}\right)$$

where $\alpha = \{h, \bar{\rho}, \rho\}$, γ_i are relaxation rates, and A^α_i are the normalized eigenvectors of $\mathbf{M}_{nm}$ [Seifert, 1997]. The dependence of γ_i and A^α_i on nm is dropped in the above expressions. Note that for every mode nm, there are three relaxation rates and three corresponding relaxation modes, the slowest rate γ_1 corresponding to the dominant mode. A^α_1 expresses the physical nature of the slowest relaxation mode. For instance, a purely bending mode will be of the form $[1, 0, 0]$, while a pure density difference mode will be of the form $[0, 0, 1]$.

7.1.5 Results

Table 7.1: Material properties

Dissipative parameters	μ_b	10^{-3} Js/m^3
	μ_s	2.5×10^{-9} Js/m^2 [Jönsson et al., 2009]
	λ_s	0
	b_m	1×10^{9} Js/m^4 [Merkel et al., 1989]
Elastic modulus	κ	10^{-19} J [Jönsson et al., 2009]
	K_s	0.1 J/m^2 [Dimova et al., 2006]

As discussed before, the main goal of this chapter is to show the effect of the membrane viscosity on the dynamical relaxations of highly curved membranes. We examine dynamical relaxation by analyzing the spectrum of the dynamical matrix $\mathbf{M}_{nm}$ in Eq. (7.21). As shown in the previous section, the elastic energy and the total dissipation are independent of the order m of spherical harmonic functions. Therefore the eigenvalues and eigenvectors are not functions of m. We normalize the sphere's radius with respect to the Saffman-Delbrück length scale $l_0 = \mu_s/\mu_b$. We set the material parameters as presented in table. 7.1, resulting in $l_0 = 2.5$ µm. The dilatational viscosity λ_s is not reported in the literature to the best of our knowledge, and should not be confused with the dilatational viscosity reported in [Dimova et al., 2006], based on experiments of pore expansion by [Brochard-Wyart et al., 2000]. Based on physical grounds, we expect this parameter, notoriously difficult to measure, to be much smaller than μ_s, and set $\lambda_s = 0$ in all our calculations.

Figure 7.1 shows the relaxation rates and normalized eigenvectors for vesicles of radii R_0/l_0 =10, 1, 0.1. In this figure, solid line shows the calculations ignoring the membrane interfacial viscosity, and dash line presents the calculations considering μ_s. We observe that for vesicles of radii $>> l_0$, the membrane viscosity has a negligible effect and the predictions are very similar to those for planar membranes (see [Seifert and Langer, 1993] setting $q = n/R_0$), and membrane viscosity plays a role for very short wavelengths. However, we show that for vesicles of radii $\leq l_0$, the membrane viscosity changes the relaxation rates significantly For instance, for vesicles of radius

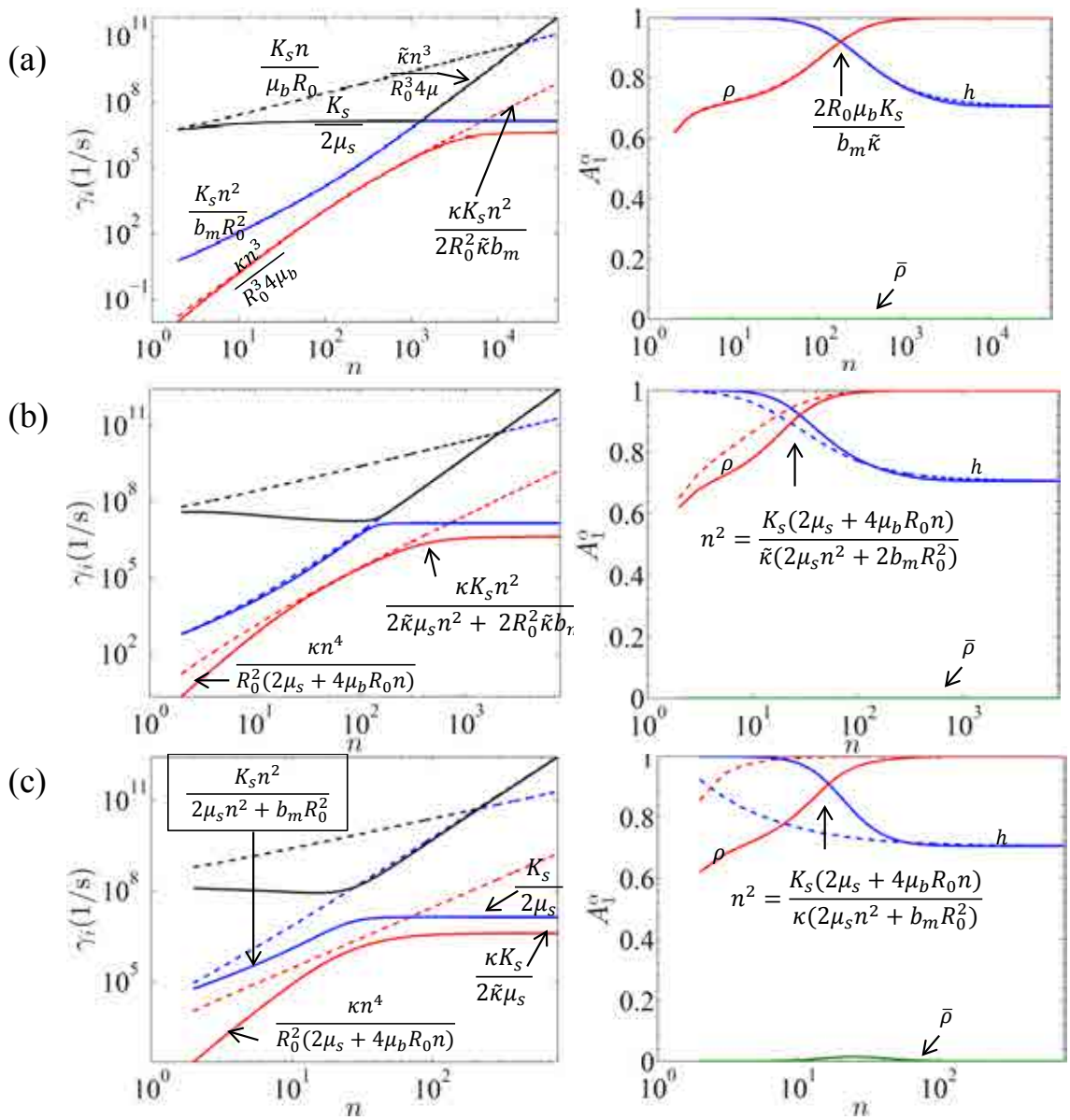

Figure 7.1: Eigenvalues and normalized eigenvectors for the dynamical relaxation of spherical vesicles, (a) $R_0/l_0 = 10$, (b) $R_0/l_0 = 1$, (c) $R_0/l_0 = 0.1$, dash line: neglecting the membrane viscosity, solid line: accounting for the membrane viscosity. The crossover mode number, at which the nature of the nature of the slow mode changes, can be appreciated in the right panels. The asymptotic estimations for the relaxation rates and the crossover mode numbers are presented for different regimes and vesicles of different sizes.

$R_0 = 0.1l_0$, the slowest relaxation rates (corresponding to the most observable fluctuations) are slowed down by more than one order of magnitude in the presence of the membrane viscosity. This can be understood by examining Eq. (7.22) below. The crossover mode number, at which the physical nature of the slow mode changes, is postponed to higher frequencies (shorter wavelengths), due to the presence of μ_s. We estimate the asymptotic behavior of relaxation rates for the model with membrane viscosity. We find that for low frequencies the slowest rates can be expressed as

$$\gamma_1 = \frac{\kappa n^4}{R_0^2\,(2\mu_s + 4\mu_b R_0 n)}, \tag{7.22}$$

while for intermediate frequencies, we have

$$\gamma_1 = \frac{\kappa K_s n^2}{2\tilde{\kappa}\mu_s n^2 + 2R_0^2\tilde{\kappa}b_m}.$$

For very short wavelengths, we have $\gamma_1 = \kappa K_s/2\bar{\kappa}\mu_s$ as for planar membranes. An estimate of the crossover mode number is indicated in the right panels of this figure, which further highlights the role of the curvature and membrane viscosity. In general, λ_s and μ_s appear in all these asymptotic expressions on an equal footing. Therefore, if we took λ_s to be the dilatational viscosity reported in [Dimova et al., 2006], which is two orders of magnitude larger than μ_s, the membrane dilatational viscosity would dominate all the other dissipative mechanism even for vesicles of radii $>> l_0$. The figure provides a complete physical identification of all the asymptotic regimes, present in the relaxation dynamics.

Figure 7.2 shows the slowest relaxation rate γ_1 as a function of the vesicle radius and for modes $n = 2,\ 10,\ 20$. We observe that for low modes (e.g. n=2, the softest mode), the slowest and the most important eigenvalue deviates significantly from the estimations neglecting the membrane viscosity. For $R_0/l_0 \approx 0.01$, the relaxation rate is slowed down about two orders of magnitude in the presence of the membrane viscosity. However, for larger vesicles (e.g., $R_0/l_0 \approx 100$) we observe that the membrane viscosity can be safely neglected in the calculations.

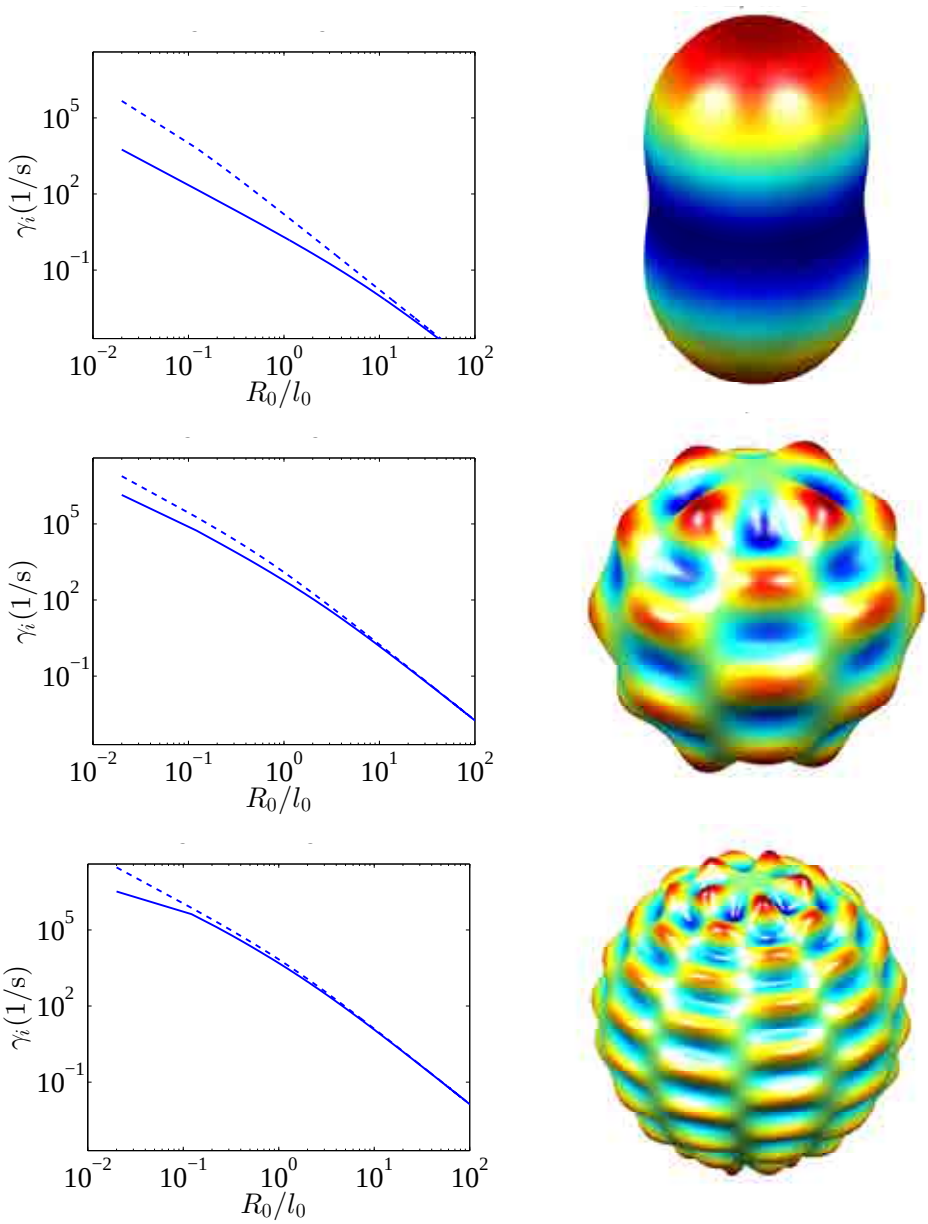

Figure 7.2: Slowest eigenvalue of the most observable fluctuating mode ($n = 2$, top row), and higher modes ($n = 10, 20$, middle and bottom rows) as a function of the vesicle's radius R_0, solid line: without the membrane viscosity, dash line: with the membrane viscosity. For each mode number n, an eigenmode is presented for an arbitrary m ($m = 0, 4, 5$ respectively).

We note that for polymersomes bilayer vesicles made out of amphiphilic polymers, the membrane viscosity is orders of magnitude larger than that of lipid bilayers. Consequently, for typical polymer vesicles or radii ≈ 40 µm [Dimova et al., 2002, Discher and Eisenberg, 2002], $R_0/l_0 \approx 0.02$. For the polymersomes analyzed in [Rodríguez-García et al., 2011] with flickering spectroscopy, we have $R_0/l_0 \approx 0.01$, showing that the present theory should be used in interpreting such measurements.

7.2 Tubular membranes

7.2.1 Kinematics

We parametrize the midsurface of a membrane tube Γ_t at a given time t, in cylindrical coordinates,

$$\boldsymbol{x}(\theta, z; t) = r(\theta, z; t)\boldsymbol{e}_r + z(\theta, z; t)\boldsymbol{e}_z = \{r(\theta, z; t)\cos\theta, r(\theta, z; t)\sin\theta, z(\theta, z; t)\}$$

where $\theta \in [0, 2\pi]$, $z \in [0, L]$, and $\boldsymbol{e}_r$, $\boldsymbol{e}_\theta$, $\boldsymbol{e}_z$ are unit basis vectors. We express the metric tensor, the normal vector, as well the surface and the volume Jacobians as

$$\begin{aligned}
\boldsymbol{g}_i &= \partial_i \boldsymbol{x}, \quad [g_{ij}] = \boldsymbol{g}_i \cdot \boldsymbol{g}_j, \quad i = r, \theta, z \\
\boldsymbol{n} &= \frac{\boldsymbol{g}_\theta \times \boldsymbol{g}_z}{|\boldsymbol{g}_\theta \times \boldsymbol{g}_z|}, \\
\mathrm{d}A &= J\ \mathrm{d}\theta\mathrm{d}z = |\boldsymbol{g}_\theta \times \boldsymbol{g}_z|\ \mathrm{d}\theta\mathrm{d}z, \\
\mathrm{d}V &= \frac{r^2}{2}\ \mathrm{d}\theta\mathrm{d}z\mathrm{d}r.
\end{aligned}$$

We consider a tubular membrane, fluctuating about a cylindrical shape in equilibrium, i.e. $r(\theta, z) = r_0 + u(\theta, z)$, $\bar{\rho}(\theta, z) = \bar{\rho}_0 + \delta\bar{\rho}(\theta, z)$, $\rho(\theta, z) = \rho_0 + \delta\rho(\theta, z)$, where the equilibrium state $r_0, \bar{\rho}_0, \rho_0$ is calculated in the next section. We express the radial, and density deviations using the Fourier functions [Bukman et al., 1996],

$$\begin{aligned}
u(\theta, z) &= \sum_{n,m} u_{nm} e^{i(m\theta + k_n z)}, \\
\delta\bar{\rho}(\theta, z) &= \sum_{n,m} \bar{\rho}_{nm} e^{i(m\theta + k_n z)}, \\
\delta\rho(\theta, z) &= \sum_{n,m} \rho_{nm} e^{i(m\theta + k_n z)},
\end{aligned} \tag{7.23}$$

where $k_n = 2n\pi/L$, and m, n are integers, which run from $-\infty$ to ∞.

7.2.2 Elastic energy

Membrane tubes form under different mechanical conditions, as exemplified in chapters 4, 5, and 6. If the tube delimits two different fluid containers, the pressure work can be expressed as $p\ \delta V$. Here, we rewrite the elastic energy given in Eq. (7.2) for a tube of length L_0, radius $r = r_0$, density average $\bar{\rho} = \bar{\rho}_0$, and density deviation $\rho = \rho_0$,

$$\Pi \;=\; \frac{\tilde{\kappa}\pi L_0}{r_0} + 2\pi r_0 L_0 \left[K_s\bar{\rho}_0^2 + K_s\rho_0^2 + \bar{\gamma}\left(\bar{\rho}_0 + 1\right) + \gamma\rho_0\right] - 4dK_s\pi L_0\rho - p\pi r_0^2 L_0,$$

where $\bar{\gamma} = \gamma^+ + \gamma^-$, and $\gamma = \gamma^+ - \gamma^-$. To obtain an equilibrium state, we minimize the total elastic energy, by setting its variations to zero

$$\begin{aligned}
0 \;&=\; \frac{\partial\Pi}{\partial\rho_0} = 2\pi r_0 L_0\left(\gamma - 2dK_s/r_0 + 2K_s\rho_0\right),\\
0 \;&=\; \frac{\partial\Pi}{\partial\bar{\rho}_0} = 2\pi r_0 L_0\left(\bar{\gamma} + 2K_s\bar{\rho}_0\right),\\
0 \;&=\; \frac{\partial\Pi}{\partial r_0} = -\frac{\tilde{\kappa}\pi L_0}{r_0^2} + 2\pi L_0\left[K_s\bar{\rho}_0^2 + K_s\rho_0^2 + \bar{\gamma}\left(\bar{\rho}_0 + 1\right) + \gamma\rho_0\right] - 2p\pi r_0 L_0.
\end{aligned}$$

From the first and the second equations we obtain the tensions $\gamma = -2K_s\rho_0 + 2dK_s/r_0$, and $\bar{\gamma} = -2K_s\bar{\rho}_0$. Note that amongst the variables $\{\bar{\rho}_0, \rho_0, p, r_0\}$, three of them are independent. For instance, we can calculate p as a function of r_0, $\bar{\rho}_0$, and ρ_0 from the third equation,

$$p \;=\; -\frac{\tilde{\kappa}}{2r_0^3} + \frac{\bar{\sigma}}{r_0} \tag{7.24}$$

where

$$\bar{\sigma} = K_s\bar{\rho}_0^2 + K_s\rho_0^2 + \bar{\gamma}\left(\bar{\rho}_0 + 1\right) + \gamma\rho_0. \tag{7.25}$$

We consider tubes at their optimal area difference ($\gamma = 0$), and otherwise allow for tubes under different pressure conditions. Note that, having fixed $\gamma = 0$, there is still

one parameter family of mechanical states exhibiting a given tube radius. As we propose in the discussion, such tubes can be obtained experimentally by pulling opposing sides of a vesicle and deflating it simultaneously. The reaction force, conjugate to the tube length can then be written as

$$f/\pi = \frac{\tilde{\kappa}}{r_0} - pr_0^2 + 2\bar{\sigma}r_0 - 4dK_s\rho_0.$$

By neglecting the first order terms, using expression given in appendix D.4, and retaining up to second order terms, the elastic energy takes the form,

$$\Pi \;=\; \frac{1}{2}\sum_{n,m} \mathbf{y}^*_{nm}\mathbf{E}_{nm}\mathbf{y}_{nm},$$

where $\mathbf{y}_{nm} = [u_{nm}, \bar{\rho}_{nm}, \rho_{nm}]^T$,

$$\mathbf{E}_{nm} = 2\pi L \begin{pmatrix} [\tilde{\kappa}q_{nm}/r_0^3 - p + \bar{\sigma}\lambda_{nm}/r_0 - 4dK_s\rho_0 k_n^2] & 0 & -2dK_s(\lambda_{nm}-1)/r_0 \\ 0 & 2K_s r_0 & 0 \\ -2dK_s(\lambda_{nm}-1)/r_0 & 0 & 2K_s r_0 \end{pmatrix},$$

$\lambda_{nm} = r_0^2 k_n^2 + m^2$, and $q_{nm} = -\lambda_{nm}/2 + \lambda_{nm}^2 - m^2 + 1$.

We insist again that for general values of r_0, $\bar{\rho}_0$ and ρ_0, this equilibrium state is not necessarily stable. To examine the stability of a given state, the stiffness matrix $\mathbf{E}_{nm}$, introduced above should be always positive-definite.

7.2.3 Dissipation

We describe the surface velocity field by vector cylindrical harmonics

$$\boldsymbol{V}^{\pm} = \sum_{n,m} \boldsymbol{V}_{nm} = \sum_{nm} \big(v_{nm}^{r\pm}\boldsymbol{Y}_{nm} + \underbrace{v_{nm}^{(1)\pm}\boldsymbol{\Psi}_{nm} + v_{nm}^{(2)\pm}\boldsymbol{\Phi}_{nm}}_{\boldsymbol{v}_{nm}} \big), \tag{7.26}$$

where $\boldsymbol{Y}_{nm}(\theta,z) = e^{i(m\theta+k_n z)}\hat{\boldsymbol{e}}_r$, $\boldsymbol{\Psi}_{nm}(\theta,z) = r_0\boldsymbol{\nabla}_s\left[e^{i(m\theta+k_n z)}\right]$, and $\boldsymbol{\Phi}_{nm} = \hat{\boldsymbol{e}}_r \times \boldsymbol{\Psi}_{nm}$. Some mathematical properties of vector cylindrical harmonics are given in appendix D.5.

Membrane dissipation

Employing Eqs. (7.6) and taking the advantage of the expressions in appendix D.5, we express the membrane dissipation including the interfacial viscosity as

$$W_{\mu_s} + W_{\lambda_s} = \frac{1}{2}\sum_{n,m} \boldsymbol{V}_{nm}^{\pm *}\mathbf{D}_{nm}^{\mathrm{mem}\pm}\boldsymbol{V}_{nm}^{\pm}, \tag{7.27}$$

and the interlayer friction as

$$\begin{aligned} W_{b_m}[\boldsymbol{v}^{\pm}] &= \frac{b_m}{2}\int_{\Omega} \|\boldsymbol{v}^{+} - \boldsymbol{v}^{-}\|^2 \,\mathrm{d}S \\ &= \frac{b_m}{2}\left(2\pi r_0 L_0\right)\sum_{nm}\left((v_{nm}^{(1)+} - v_{nm}^{(1)-})^2 + (v_{nm}^{(2)+} - v_{nm}^{(2)-})^2\right)\lambda_{nm}, \end{aligned} \tag{7.28}$$

where

$$\mathbf{D}_{nm}^{\mathrm{mem}\pm} = (2\pi r_0 L_0)\begin{bmatrix} (2\mu_s+\lambda_s)/r_0^2 & (2m^2\mu_s+\lambda_{nm}\lambda_s)/r_0^2 & 2k_n m\mu_s/r_0 \\ (2m^2\mu_s+\lambda_{nm}\lambda_s)/r_0^2 & \lambda_{nm}^2(2\mu_s+\lambda_s)/r_0^2 & 0 \\ 2k_n m\mu_s/r_0 & 0 & \lambda_{nm}^2 2\mu_s/r_0^2 \end{bmatrix}.$$

Again, we observe that the interfacial viscosity dissipation potential does depend on the normal velocities through the term $(2\mu_s+\lambda_s)/r_0^2$.

Bulk fluid dissipation

In this section, we calculate the dissipation ,due to the bulk fluid surrounding the membrane tube. A general solution to the 3D Stokes equations in cylindrical coordi-

nates is given by [Happel and Brenner, 1965, Henle and Levine, 2010],

$$\begin{aligned} \boldsymbol{V}^{b\pm}(r,\theta,z) = \quad & \boldsymbol{\nabla} f^{\pm}(r,\theta,z) + \boldsymbol{\nabla} \times \left[g^{\pm}(r,\theta,z)\hat{\boldsymbol{e}}_z \right] \\ & + r\partial_r \left[\boldsymbol{\nabla} h^{\pm}(r,\theta,z) \right] + \partial_z h^{\pm}(r,\theta,z)\hat{\boldsymbol{e}}_z, \\ p^{\pm}(r,\theta,z) = \quad & -2\mu_b \partial_z^2 h^{\pm}(r,\theta,z), \end{aligned} \tag{7.29}$$

where $f^{\pm}(r,\theta,z)$, $g^{\pm}(r,\theta,z)$, $h^{\pm}(r,\theta,z)$ are cylindrical harmonic functions

$$\left\{ \begin{array}{c} f^{\pm}(r,\theta,z) \\ g^{\pm}(r,\theta,z) \\ h^{\pm}(r,\theta,z) \end{array} \right\} = \sum_{n,m} \left\{ \begin{array}{c} F^{\pm}_{nm} \\ G^{\pm}_{nm} \\ H^{\pm}_{nm} \end{array} \right\} P^{\pm}_m(k_n, r) e^{i(m\theta + k_n z)}.$$

Here by $P^{\pm}_m(k_n, r)$, we denote modified Bessel functions of the second and first kind, i.e. $P^{+}_m = K_m(|k_n|r)$ and $P^{-}_m = I_m(|k_n|r)$, respectively. Since $\lim_{x\to 0} K_m(x) = \lim_{x\to\infty} I_m(x) = \infty$, the modified Bessel functions of the first and second kind are appropriate solutions for the exterior and interior bulk fluid, respectively. We can calculate the coefficients of the harmonic functions (F, G, and H) by imposing the non-slip boundary conditions on the surface. Expressing the bulk fluid velocities on the cylindrical surface. As $\boldsymbol{V}^{b\pm} = V^b_r \hat{\boldsymbol{e}}_r + V^{b\pm}_\theta \hat{\boldsymbol{e}}_\theta + V^{b\pm}_z \hat{\boldsymbol{e}}_z$, and recalling Eqs. (7.29), we have

$$\begin{aligned} V^b_r &= \partial_r f^{\pm} + \frac{1}{r}\partial_\theta g^{\pm} + r\partial^2_{rr} h^{\pm}, \\ V^{b\pm}_\theta &= \frac{1}{r}\partial_\theta f^{\pm} - \partial_r g^{\pm} - \frac{1}{r}\partial_\theta h^{\pm} + \partial^2_{\theta r} h^{\pm}, \\ V^{b\pm}_z &= \partial_z f^{\pm} + r\partial^2_{zr} h^{\pm} + \partial_z h^{\pm}. \end{aligned} \tag{7.30}$$

On the other hand, we expand the surface velocity field with scalar Fourier modes (different from the expansion with vector cylindrical modes in Eq. (7.26))

$$\boldsymbol{V}^{\pm} = \sum_{n,m} \left(w^{r\pm}_{nm} \hat{\boldsymbol{e}}_r + w^{\theta\pm}_{nm} \hat{\boldsymbol{e}}_\theta + w^{z\pm}_{nm} \hat{\boldsymbol{e}}_z \right) e^{i(m\theta + k_n z)}, \tag{7.31}$$

Combining Eqs. (7.30) and (7.31), the coefficient of the harmonic functions can be computed in terms of the surface velocity as

$$\left\{ \begin{array}{c} w_{nm}^{r\pm} \\ w_{nm}^{\theta\pm} \\ w_{nm}^{z\pm} \end{array} \right\} = 1/r_0 \mathbf{T}^{\pm *} \left\{ \begin{array}{c} F_{nm}^{\pm} \\ G_{nm}^{\pm} \\ H_{nm}^{\pm} \end{array} \right\}, \tag{7.32}$$

or,

$$\left\{ \begin{array}{c} F_{nm}^{\pm} \\ G_{nm}^{\pm} \\ H_{nm}^{\pm} \end{array} \right\} = r_0 \left(\mathbf{T}^{\pm *} \mathbf{T}^{\pm} \right)^{-1} \mathbf{T}^{\pm *} \left\{ \begin{array}{c} w_{nm}^{r\pm} \\ w_{nm}^{\theta\pm} \\ w_{nm}^{z\pm} \end{array} \right\}, \tag{7.33}$$

where, $\mathbf{T}^{\pm} = \left(\mathbf{T}_{\mathrm{Re}}^{\pm} - i\mathbf{T}_{\mathrm{Im}}^{\pm} \right)$, and

$$\mathbf{T}_{\mathrm{Re}}^{\pm} = \left\{ \begin{array}{ccc} \left[\mp |k_n| r_0 P_{m+1}^{\pm} + m P_m^{\pm} \right] & 0 & \left[(\lambda_{nm} - m) P_m^{\pm} \pm |k_n| r_0 P_{m+1}^{\pm} \right] \\ 0 & \left[\pm |k_n| r_0 P_{m+1}^{\pm} - m P_m^{\pm} \right] & 0 \\ 0 & 0 & 0 \end{array} \right\},$$

$$\mathbf{T}_{\mathrm{Im}}^{\pm} = \left\{ \begin{array}{ccc} 0 & m P_m^{\pm} & 0 \\ m P_m^{\pm} & 0 & \left[(m^2 - m) P_m^{\pm} \mp m |k_n| r_0 P_{m+1}^{\pm} \right] \\ k_n r_0 P_m^{\pm} & 0 & k_n r_0 \left[(m+1) P_m^{\pm} \mp k_n r_0 P_{m+1}^{\pm} \right] \end{array} \right\}.$$

We note that in these expressions $P_m^{\pm} = P_m^{\pm}(K_n r_0)$ are scalars that depend on n and m alone, since the radius is fixed on the cylinder.

The traction vector acting across the surface of a tube in cylindrical coordinates for an incompressible Newtonian fluid is [Happel and Brenner, 1965],

$$\boldsymbol{t}^{b\pm} = \pm \hat{\boldsymbol{e}}_r \cdot \boldsymbol{\sigma}^{b\pm} = \pm \left[\begin{array}{c} -p^{\pm} + 2\mu_b \partial_r V_r \\ \mu_b r \partial_r \left(V_\theta / r \right) + \mu_b \partial_\theta V_r / r \\ \mu_b \left(\partial_z V_r + \partial_r V_z \right) \end{array} \right].$$

Replacing Eqs. (7.33),(7.30) into the above relation, we find

$$\begin{aligned}\boldsymbol{t}^{b\pm} &= \pm\mu_b \sum_{nm} e^{i(m\theta+k_n z)} \left(\mathbf{D}^{\pm}_{\mathrm{Re}} + i\mathbf{D}^{\pm}_{\mathrm{Im}}\right) \begin{Bmatrix} F^{\pm}_{mn} \\ G^{\pm}_{mn} \\ H^{\pm}_{mn} \end{Bmatrix} \\ &= \pm\sum_{nm} e^{i(m\theta+k_n z)} \underbrace{\left(\mathbf{D}^{\pm}_{\mathrm{Re}} + i\mathbf{D}^{\pm}_{\mathrm{Im}}\right) r_0 \left(\mathbf{T}^{\pm *}\mathbf{T}^{\pm}\right)^{-1} \mathbf{T}^{\pm *}}_{\mathbf{S}^{\pm}{}_{nm}} \begin{Bmatrix} w^{r\pm}_{mn} \\ w^{\theta\pm}_{mn} \\ w^{z\pm}_{mn} \end{Bmatrix}, \end{aligned} \tag{7.34}$$

where the nonzero components of $\mathbf{D}^{\pm}_{\mathrm{Re}}$, and $\mathbf{D}^{\pm}_{\mathrm{Im}}$ are given in appendix D.6. Finally, mapping the surface velocity from a cylindrical Fourier representation to its coefficients in vector cylindrical harmonics (Eq. (7.26)),

$$\begin{Bmatrix} w^{r\pm}_{nm} \\ w^{\theta\pm}_{nm} \\ w^{z\pm}_{nm} \end{Bmatrix} = \underbrace{\begin{Bmatrix} 1 & 0 & 0 \\ 0 & im & -ik_n r_0 \\ 0 & ik_n r_0 & im \end{Bmatrix}}_{\mathbf{B_{nm}}} \underbrace{\begin{Bmatrix} v^{(r)\pm}_{nm} \\ v^{(1)\pm}_{nm} \\ v^{(2)\pm}_{nm} \end{Bmatrix}}_{\boldsymbol{v}_{nm}}.$$

we can write the dissipation potential for the bulk fluid as

$$W_{\mu_b} = -\frac{1}{2}\int_{\Gamma} \boldsymbol{t}^{b\pm *} \cdot \boldsymbol{v}^{\pm}\, \mathrm{d}S = \frac{\mu_b}{2}\left(2\pi r_0 L_0\right) \sum_{nm} \boldsymbol{v}^{\pm *}{}_{nm} \mathbf{D}^{\mathrm{bulk}\pm}_{nm} \boldsymbol{v}^{\pm}{}_{nm}.$$

where $\mathbf{D}^{\mathrm{bulk}\pm}_{nm} = \mp\left(\mathbf{B}^{*}_{\mathbf{nm}}\mathbf{S}^{\pm}_{nm}\mathbf{B}_{\mathbf{nm}}\right)$.

Continuity equation and governing equations

The continuity equation (Eq. (7.17)) now takes the form

$$\underbrace{\begin{pmatrix} \dot{u}_{nm} \\ \dot{\bar{\rho}}_{nm} \\ \dot{\rho}_{nm} \end{pmatrix}}_{\dot{\mathbf{y}}_{nm}} = \underbrace{\begin{pmatrix} 1 & 0 & 0 \\ -1/r_0 & \lambda_{nm}/2r_0 & \lambda_{nm}/2r_0 \\ 0 & \lambda_{nm}/2r_0 & -\lambda_{nm}/2r_0 \end{pmatrix}}_{\mathbf{C}_{nm}} \underbrace{\begin{pmatrix} v_{nm}^{(r)} \\ v_{nm}^{(1)+} \\ v_{nm}^{(1)-} \end{pmatrix}}_{\boldsymbol{V}_{nm}}. \tag{7.35}$$

Analogously to section 7.1.4, we drive the governing equations for relaxation dynamics of tubular membranes, as

$$\dot{\mathbf{y}}_{nm} = -\mathbf{M}_{nm}\mathbf{y}_{nm}. \tag{7.36}$$

where $\mathbf{M}_{nm} = \mathbf{C}_{nm}{\mathbf{D}_{nm}^{\text{tot}}}^{-1}\mathbf{C}_{nm}^{T}\mathbf{E}_{nm}$.

7.2.4 Results

We first illustrate a selection of cylindrical harmonics in Fig. 7.3. The modes $m = \pm 1$, and $n = 0$ correspond to rigid body modes, giving no contribution to the elastic energy. The modes $m = \pm 1$, and $n \neq 0$ (longitudinal wave modes with circular cross section of uniform radius), are known as Goldstone modes, and have been shown to be extremely soft for very thin tubes without pressure jump [Fournier and Galatola, 2007]. In contrast, modes with deformations of the circular cross section, particularly for thin tubes, are very stiff, and may exhibit very fast relaxation rates. Note that modes $m = 0$ and $n \neq 0$, are the only axisymmetric fluctuating shapes.

We first investigate the time-averaged amplitudes of the thermal undulations resorting to the equipartition theorem (given in Eq. (7.4)). Figure 7.4 shows the normalized thermal undulation amplitudes $\bar{h}_{nm} = \sqrt{\langle u_{nm} u_{nm}^{*} \rangle}/r_0$ for tubes of different radii ($r_0 = \{0.02 l_0,\ 0.2\ l_0,\ l_0\} = \{50$ nm, 500 nm, 2.5 µm$\}$), for $m = 0, 1$, and choosing n to be the corresponding softest mode (that with the largest amplitude). We plot these

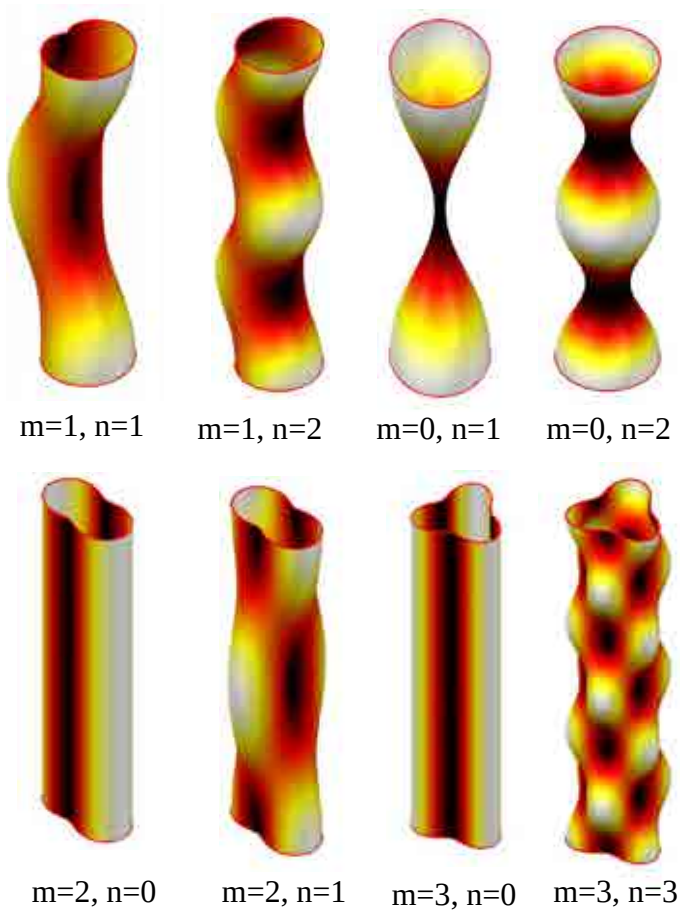

Figure 7.3: Selection of cylindrical harmonics. $m = \pm 1$, and $n = 0$ are related the rigid body motion. $m = 0$ and $n \neq 0$ presents the axisymmetric mode shapes. $m = \pm 1$, and $n \neq 0$ are longitudinal wave modes with circular cross section, known as Goldstone modes.

amplitudes as a function of the average surface tension $\bar{\sigma}/\sigma_0$ (see Eq. (7.25)), where $\sigma_0 = \bar{\kappa}/2r_0^2$ is surface tension experienced by a tube of radius r_0 in the absence of a pressure difference (see Eq. (7.24)). We fix the tube length $L_0/l_0 = 10$ ($L_0 = 25$ µm), in all the calculations. This figure shows that the amplitudes of the thermal undulations strongly depend on the equilibrium state. For instance, equilibrium states close to an instability exhibit fluctuations of very large amplitude. Interestingly, for $m = 0$ the tubes exhibit a Plateau-like instability previously reported by [Bar-Ziv and Moses, 1994] for high positive surface tensions, which can be triggered by applying a

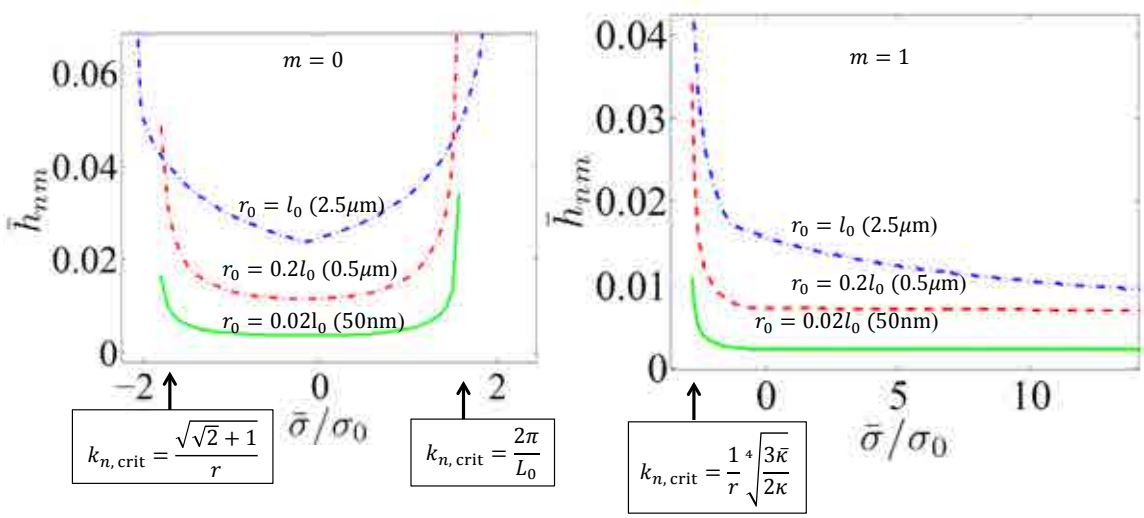

Figure 7.4: Maximum thermal undulation amplitudes (the softest mode n) for tubes of radii $r_0 = 50$ nm, 500 nm, 2.5 µm) and $m = 0, 1$ as functions of the average surface tension.

high pulling force. On the other hand, for highly negative surface tension and pressure difference, we also observe a pearling instability. We observe that thinner tubes exhibit a sharper instability. We note that the maximum amplitude presented here is not necessarily associated to $n = 1$, except for the Plateau-like ($m = 0$, positive surface tension), which always occurs at $n = 1$ or $k_{n,\mathrm{crit}} = 2\pi/L_0$. For the Plateau-like instability, we always have $n = 1$ ($k_{n,\mathrm{crit}} = 2\pi/L_0$), i.e. the softest mode is that with the longest possible wavelength. However, the instability at negative tension and pressure occurs at a finite wavelength, proportional (and close to) the tube radius, i.e. for $m = 0$, $k_{n,\mathrm{crit}} = \sqrt{\sqrt{2}+1}/r_0$, while for $m = 1$, $k_{n,\mathrm{crit}} = \sqrt[4]{3\bar{\kappa}/2\kappa r_0^4}$.

So far, there has been no reports on the thermal undulations of tubular membranes, possibly due to their small fluctuation amplitudes for tethers pulled out of a vesicle with a constant tension. It has been recently suggested that the tubular membrane fluctuations can be correlated to the pulling force (applied by the optical tweezer), whose fluctuations are detectable [Fournier and Galatola, 2007]. However, such tethers experience negligible pressure difference, restricting the equilibria to $\bar{\sigma} = \sigma_0$. We suggest to pull out a vesicle from opposing sides by two optical tweezers [Lee et al.,

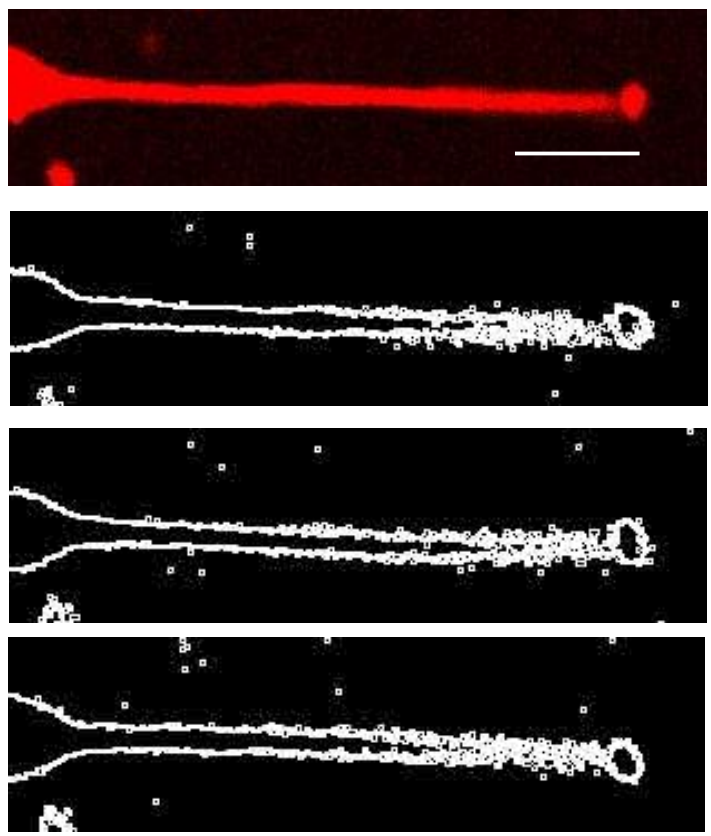

Figure 7.5: The confocal images of an undulating tube of radius≈ 0.5 µm. Top image shows a florescent image. The image segmentations in three different time instances are shown. Scale bar: 5 µm.

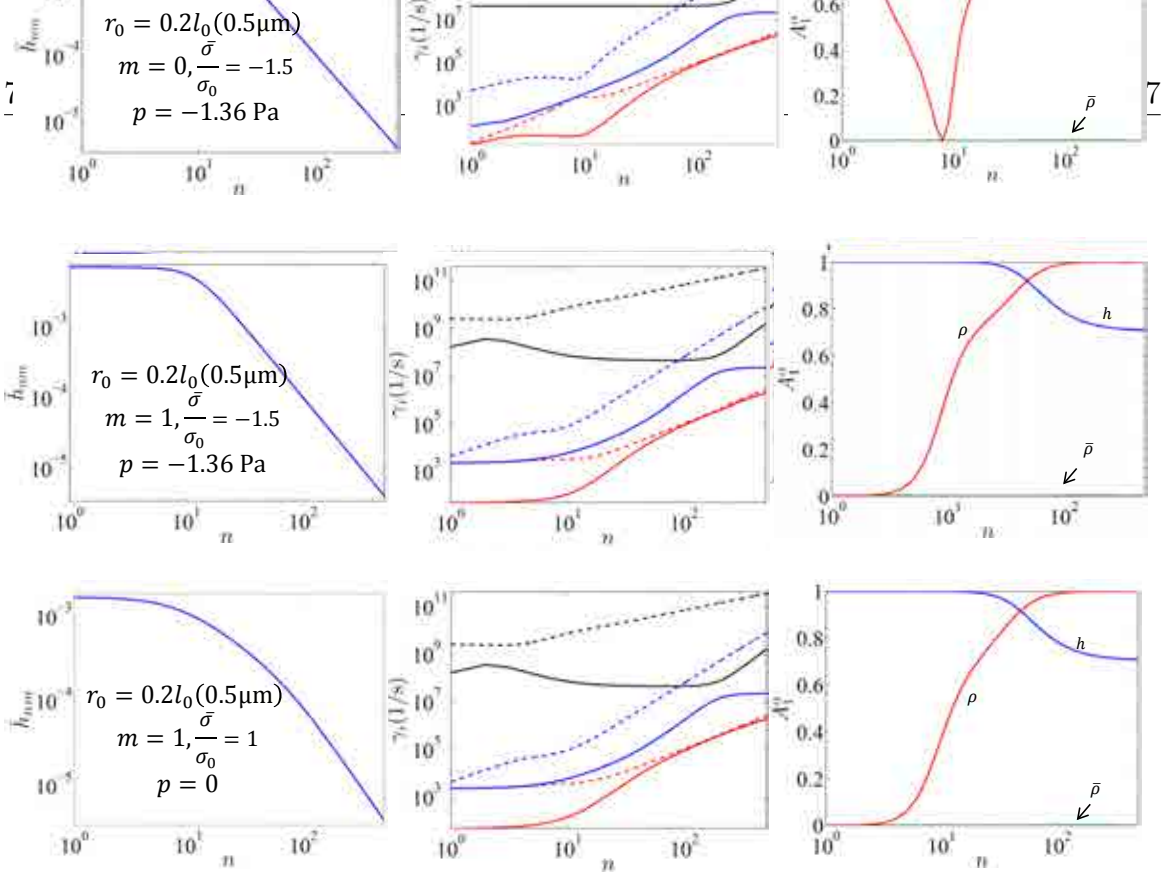

Figure 7.6: Thermal undulations and dynamical rates as well as the normalized eigenvectors (corresponding to the slowest mode) of a tube of radius $r_0 = 0.2l_0 = 500$ nm, for $m = 0$, two top row, and $m = 1$: two bottom rows ($\bar{\sigma} = \sigma_0$). The relaxation rates are plotted neglecting the membrane viscosity (dash-lines).

2008], and to deflate it simultaneously, forming a thick tube with a desired surface tension. In such a system, it is in principle possible to specify r_0, and $\bar{\sigma}$, by controlling the osmolarity and the pulling force. Figure 7.5 shows the confocal images of a fluctuating tube, obtained by serendipity in the experiments of chapter 6

Figure 7.6 shows the thermal undulations, relaxation rates and normalized eigenvectors of a tubular membrane of radius $r_0 = 0.2\ l_0$, for modes $m = 0,\ 1$, and for $\bar{\sigma} = \sigma_0$. We also calculate the relaxation rates neglecting the membrane viscosity (dash-lines), indicating that for tubes of radius close to l_0, and for $m = 0$ its effects are negligible, while for $m = 1$ it plays an important role.

Figure 7.7 shows the thermal and dynamical rates of tubular membranes of radius $r_0 = 0.02\ l_0$ (50nm) and for modes $m = 0,\ 1$. Here, we consider only tubes under a negative surface tension close to the instability. Again the effect of the membrane

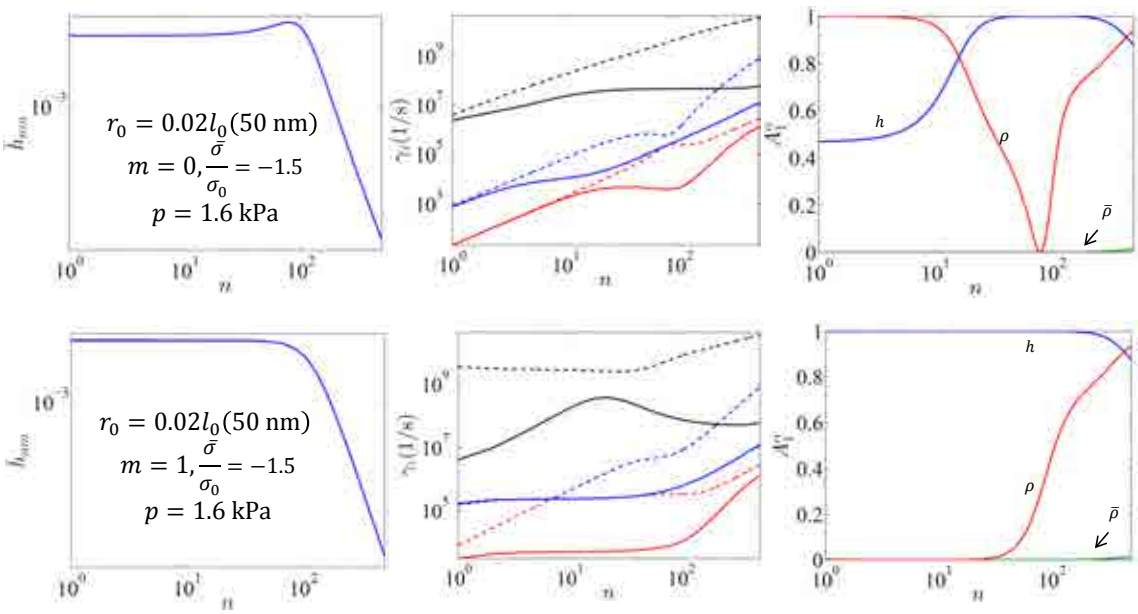

Figure 7.7: Thermal undulations and dynamical rates as well as the normalized eigenvectors (corresponding to the slowest mode) of a tube of radius $r_0 = 0.02l_0 = 50$ nm, for $m = 0$, top row and $m = 1$ bottom row ($\bar{\sigma} = -1.5\sigma_0$). The relaxation rates are plotted neglecting the membrane viscosity (dash-lines).

shear viscosity is highlighted by comparing the full theory (solid line) with that neglecting the membrane viscosity (dashed line). The role of the membrane viscosity is significantly stronger for $m = 1$. The effect of pearling instability can be appreciated for $m = 0$, and $\bar{\sigma} = -1.5\sigma_0$, with a peak of amplitude and a significantly slower relaxation for a mode of finite wavelength (n_{crit}).

7.3 Summary

We have investigated the dynamical relaxation of highly curved membranes by accounting for main dissipative mechanisms, including the bulk fluid and the membrane interfacial viscosities, as well as the interlayer slippage. We have studied the thermal undulations of spherical and cylindrical membranes, in different equilibrium states, interms of geometry and stress, with a particular focus on the membrane viscosity. Our

calculations show that when the membrane curvature is below the Saffman-Delbrück length scale, the membrane viscosity plays a very important role in the relaxation dynamics. Such effects can be experimentally observed in the thermal undulations of either polymersomes (made of highly viscous amphiphilic bilayers), or highly curved lipid bilayer structures using high resolution techniques. The thermal undulations of membrane tubes has never been experimentally reported possibly due to their small amplitudes, and the very small radius of the tethers usually manipulated in experiments under an optical microscope. We have proposed a setup, based on stretching and simultaneously deflating vesicles, which can produce tubes of larger diameter, where fluctuations may be recorded. Furthermore, by triggering instabilities in tubes, it is possible to measure equilibrium properties.

Chapter 8

Concluding remarks and future directions

8.1 Conclusions

In this thesis, we have studied dynamical shape transformations, triggered mechanically or chemically, and the stabilization of lipid bilayers in complex geometries and mechanical states. Towards this goal, we have developed the theory, performed simulations, and experiments. Here, we summarize the main achievements of this study.

- We have developed a comprehensive dynamical continuum model for lipid bilayers to investigate out-of-equilibrium phenomena, and implemented it numerically. This model, restricted to axisymmetry, is to our knowledge the first to consider general and finite shape and lipid density changes. This model allows us to study very complex, biologically relevant, dynamical events, without resorting to simplifying assumptions on the magnitude of the disturbances, the kinds of shapes the bilayer can adopt, or the relative importance of the different phenomena.

- Our simulations show that acknowledging the bilayer architecture, rather than a simple Helfrich bending model, is crucial to explain the dynamics and shaping of highly curved structures. The presented examples show that some usual assumptions can oversimplify the response of bilayers to various stimuli, and

illustrate a wide diversity of dynamical regimes. For instance, in the relaxation of a localized density asymmetry in vesicles, we found different shape transformations, such budding, tubulating, and transient pearling, in contrast with previous study [Sens, 2004], restricted to only spherical budding.

- The transient budding, pearling and tubulation due to the localized density asymmetry takes place in a time scale given by stretching elasticity and intermonolayer friction, while a seemingly related process of bud absorption by a planar bilayer relaxes at a time-scale given by the bending elasticity and the membrane shear viscosity. Our results can explain many biophysical experiments, which have been so far understood insufficiently such as the adsorption of a bud to a planar membrane, the lipid transport between the vesicles via the membrane nanotubes, or tube formations and pearling instabilities as a consequence of local density disturbances (by a local gradient of PH [Khalifat et al., 2008, Fournier et al., 2009], or the adsorption of polymers [Tsafrir et al., 2003]).

- We have studied experimentally and theoretically the mechanics of confined membranes, including the influence of adhesion, strain and osmotic pressure. We have shown that supported bilayers form a variety of protrusions, whose shapes can be experimentally controlled and quantitatively understood in terms of the bilayer-substrate mechanics. This study proposes new mechanisms for shaping highly curved structures, which have been attributed so far to the bilayer asymmetry, or protein induced spontaneous curvature [McMahon and Gallop, 2005, Li et al., 2011]. The theoretical framework together with experimental observations provide a mechanistic interpretation of the initiation and growth of blebs [Charras et al., 2005, Norman et al., 2010], tubular invaginations [Morris and Homann, 179], and micro-vesicles in cells [Sens and Gov, 2007].

- We have also studied experimentally and theoretically the dynamical shape transformations of model membranes, upon the adsorption of cholesterol, in different physical conditions, including supported lipid bilayers (continuous or isolated patches), and confined giant vesicles. We found that cholesterol molecules,

delivered though cyclodextrine cages, has a high tendency to be incorporated into lipid bilayers, leading to the membrane spreading, or protrusions if laterally confined. The dynamical membrane reorganizations, observed in our experiments, can help us better understand similar cellular processes involved in a number of important medical disorders.

- Our experimental observations and theoretical quantification of the formation of protrusions from SLBs could also help engineer drug delivery systems by particle coating or in designing biosensors to detect mechanochemical responses.

- We have investigated the equilibrium and dynamics of fluctuations in highly curved membranes with a particular focus on the membrane viscosity. We show that depending on the size of the vesicle/tube, even for infinitesimal shape deformations, the membrane viscosity can significantly change the dynamical rates of thermally excited spherical/tubular membranes.

- The proposed theory should be used to analyze the dynamics of highly viscous membranes, such as polymersomes, and can provide the background for new flickering spectroscopy techniques involving fluctuating tubes.

8.2 Future directions

We applied our model to a variety of physical examples, which are representative of only a few processes in cells. We suggest next further applications where our model, or extensions of it, can help understand complex dynamical phenomena.

- Fusion dynamics:

  The process of membrane fusion is essential for the functionality of cells, e.g in vesicular trafficking, secretion of proteins, hormones and neurotransmitters, and cell communications. However, despite the ubiquity of membrane fusion, many aspects of this process have remained rather controversial [Fischer et al., 2002, Noireaux and Libchaber, 2004]. Recently, the fusion of giant lipid vesicles

has been monitored with a temporal resolution of tens of µs, showing rich neck opening dynamics involving multiple time-scales [Haluska et al., 2006]. Similar to the bud absorption, simulated in chapter 4, such fast shape transformations incorporate all the internal dissipative mechanisms, as well as the stretching and bending elasticity. Therefore by including the bulk fluid dissipation to the model and selecting an appropriate initial profile for the neck, we expect that our model can bring quantitative insight about this phenomenon.

- Fission induced by inserting proteins:

  The mechanism of fission has been explained in terms of the spontaneous curvature induced by either hydrophobic insertion of amphipathic proteins into the lipid bilayers, or by surface coating proteins, which are intrinsically curved and relatively rigid [McMahon and Gallop, 2005, Shibata et al., 2009]. However, the expansion of the head group region with respect to the bilayer midplane induced by inserting proteins has been shown to change the Gaussian curvature modulus [Schwarz and Gompper, 1999] and possibly favors its fission [Boucrot et al., 2012]. Using our theory, this hypothesis can be examined by introducing a field of spontaneous curvature, and a field of Gaussian curvature modulus as a function of the spontaneous curvature. We note that so far in all our simulations, the Gaussian curvature energy has not been considered.

- Curvature/density sensing proteins:

  Proteins, in particular the BAR domain family, participate in membrane sculpting processes in vivo and change also in vitro the curvature of tubes and vesicles [Chernomordik et al., 2006, Sorre et al., 2012, Campelo et al., 2008]. Interestingly the adsorption of Bar domain proteins is shown to be dependent on the local curvature of the membrane [Sorre et al., 2012] and may also depend on the local lipid density for proteins with shallow insertions [Antonny, 2011]. We suggest that their adsorption mechanism can be coupled with our model by introducing a curvature and density dependence adsorption kinetics (see chapter 6). Such a model would enable us to examine the interaction of proteins and

bilayers (e.g. curvature/density sensing, curvature sculpting), particularly with regards to dynamics and out-of-equilibrium phenomena [Reynwar et al., 2007].

- Cholesterol adsorption to other lipid compositions:

  In model membranes, the number of saturated hydrocarbon chains in the lipids affects the membrane thickness and membrane bending modulus. The cholesterol is shown to have much stronger interaction with lipids with two saturated chains. For instance, the elastic moduli of DMPC, or DPPC lipids, as well as their dynamical properties (such as the lateral diffusion) have been shown to depend significantly on its cholesterol content [Pan et al., 2009, Khatibzadeh et al., 2012]. We have in mind a protocol to load labeled cholesterol into MβCD. This would allow us to probe experimentally the density of the cholesterol inside the membrane. Then using the experimental setup introduced in chapter 6, we hypothesize that cholesterol can be sorted, both statically (in the protrusions) and dynamically, in membranes of double chain saturated lipids [Jiang and Powers, 2008]. Theoretically, we plan to model the system by introducing fields of elastic and kinetic moduli dependent on the cholesterol area fraction.

The discrete system, even under axisymmetry, can be very challenging to deal with numerically. The numerical stiffness of the equations, and physical phenomena spanning huge ranges of spaces and mostly time scales, pose serious challenges to the efficient time-integration of the equations. The computational cost is further challenged when considering the effect of the bulk fluid. Targeted numerical techniques, including time-stepping algorithms based on time-incremental pseudo-potentials [Peco et al., 2012], can significantly improve the efficiency and robustness of the simulations. Although many important membrane structures adopt axisymmetric shapes, other subcellular structures do not. Thus, implementing the proposed theory in three dimensions can further expand its capabilities.

Bibliography

M. Alwarawrah, J. Dai, and J. Huang. A molecular view of the cholesterol condensing effect in dopc lipid bilayers. *The Journal of Physical Chemistry B*, 114(22):7516–7523, 2010.

M.I. Angelova and D.S. Dimitrov. Liposome electroformation. *Faraday Discuss. Chem. Soc.*, 81:303–311, 1986.

B. Antonny. Mechanisms of membrane curvature sensing. *Annu. Rev. Biochem.*, 80: 101–123, 2011.

LR Arriaga, R. Rodríguez-García, I. López-Montero, B. Farago, T. Hellweg, and F. Monroy. Dissipative curvature fluctuations in bilayer vesicles: Coexistence of pure-bending and hybrid curvature-compression modes. *The European Physical Journal E: Soft Matter and Biological Physics*, 31(1):105–113, 2010.

M. Arroyo and A. DeSimone. Relaxation dynamics of fluid membranes. *Phys. Rev. E*, 79:031915, 2009.

M. Arroyo, A. Desimone, and L. Heltai. Interfacial hydrodynamics in relaxing vesicles in a viscous fluid. under review, 2012.

R. Bar-Ziv and E. Moses. Instability and" pearling" states produced in tubular membranes by competition of curvature and tension. *Physical review letters*, 73(10): 1392–1395, 1994.

RG Barrera, GA Estevez, and J. Giraldo. Vector spherical harmonics and their application to magnetostatics. *European Journal of Physics*, 6(4):287, 2000.

Pavel V. Bashkirov, Sergey A. Akimov, Alexey I. Evseev, Sandra L. Schmid, Joshua Zimmerberg, and Vadim A. Frolov. GTPase cycle of dynamin is coupled to membrane squeeze and release, leading to spontaneous fission. *Cell*, 135:1276 – 1286, 2008.

T. Belytschko, WK Liu, and B. Moran. *Nonlinear finite elements for continua and structures*, volume 36. Wiley, 2000.

W.F.D. Bennett, J.L. MacCallum, M.J. Hinner, S.J. Marrink, and D.P. Tieleman. Molecular view of cholesterol flip-flop and chemical potential in different membrane environments. *Journal of the American Chemical Society*, 131(35):12714–12720, 2009.

A.L. Bernard, M.A. Guedeau-Boudeville, L. Jullien, and J.M. Di Meglio. Strong adhesion of giant vesicles on surfaces: dynamics and permeability. *Langmuir*, 16 (17):6809–6820, 2000.

E. Boucrot, A. Pick, G. Çamdere, N. Liska, E. Evergren, H.T. McMahon, and M.M. Kozlov. Membrane fission is promoted by insertion of amphipathic helices and is restricted by crescent bar domains. *Cell*, 149(1):124–136, 2012.

C.E. Brennen. *Fundamentals of multiphase flow*. Cambridge University Press, 2005.

F. Brochard-Wyart, P.G. de Gennes, and O. Sandre. Transient pores in stretched vesicles: role of leak-out. *Physica a*, 278:32–51, 2000.

F.L.H. Brown. Regulation of protein mobility via thermal membrane undulations. *Biophysical journal*, 84(2):842–853, 2003.

D.J. Bukman, J.H. Yao, and M. Wortis. Stability of cylindrical vesicles under axial tension. *Physical Review E*, 54(5):5463, 1996.

F. Campelo and A. Hernandez-Machado. Polymer-induced tubulation in lipid vesicles rid c-8852-2009. *Phys. Rev. Lett.*, 100:158103, 2008.

F. Campelo, H.T. McMahon, and M.M. Kozlov. The hydrophobic insertion mechanism of membrane curvature generation by proteins. *Biophysical journal*, 95(5): 2325–2339, 2008.

R Capovilla and J Guven. Stresses in lipid membranes. *J. Phys, A-Math. Gen.*, 35: 6233, 2002.

G Charras and E Paluch. Blebs lead the way: how to migrate without lamellipodia. *Nat. Rev. Mol. Cell Bio.*, 9(730-736), 2008.

G. T. Charras, J. C. Yarrow, M. A. Horton, L. Mahadevan, and Mitchison T. J. Non-equilibration of hydrostatic pressure in blebbing cells. *Nature*, 435:365–369, 2005.

L.V. Chernomordik, J. Zimmerberg, and M.M. Kozlov. Membranes of the world unite! *The Journal of cell biology*, 175(2):201–207, 2006.

AE Christian, MP Haynes, MC Phillips, and GH Rothblat. Use of cyclodextrins for manipulating cellular cholesterol content. *Journal of lipid research*, 38(11):2264–2272, 1997.

I R Cooke, K. Kremer, and M. Deserno. Tunable generic model for fluid bilayer membranes. *Phys. Rev. E*, 72:011506, 2005.

I Derényi, F. Julicher, and J. Prost. Formation and interaction of membrane tubes. *Phys. Rev. Lett.*, 88:238101, 2002.

I Derényi, G Koster, M van Duijn, A Czovek, M Dogterom, and J Prost. Membrane nanotubes. *Lect. Notes Phys*, 711:141–159, 2007.

P.F. Devaux. Is lipid translocation involved during endo- and exocytosis? *Biochimie*, 82:497–509, 2000.

K.A. Dill. *Molecular Driving Forces: Statistical Thermodynamics in Chemistry & Biology*. Routledge, 2002.

R. Dimova and R. Lipowsky. Lipid membranes in contact with aqueous phases of polymer solutions. *Soft Matter*, 2012.

R. Dimova, U. Seifert, B. Pouligny, S. Forster, and H.G. Dobereiner. Hyperviscous diblock copolymer vesicles. *Eur. Phys. J. E*, 7:241–250, 2002.

R. Dimova, S. Aranda, N. Bezlyepkina, V. Nikolov, K. A. Riske, and R. Lipowsky. A practical guide to giant vesicles. probing the membrane nanoregime via optical microscopy. *J. Phys-Condens. Mat.*, 18:S1151–S1176, 2006.

D.E. Discher and A. Eisenberg. Polymer vesicles. *Science*, 297(5583):967–973, 2002.

H.G. Döbereiner, G. Gompper, C.K. Haluska, D.M. Kroll, P.G. Petrov, and K.A. Riske. Advanced flicker spectroscopy of fluid membranes. *Physical review letters*, 91(4):48301, 2003.

Y.A. Domanov and P.K.J. Kinnunen. Antimicrobial peptides temporins b and l induce formation of tubular lipid protrusions from supported phospholipid bilayers. *Biophysical journal*, 91(12):4427–4439, 2006.

J. Donea and A. Huerta. *Finite Element Methods for Flow Problems*. Wiley Online Library, 2003.

G.P. Dubey and S. Ben-Yehuda. Intercellular nanotubes mediate bacterial communication. *Cell*, 144(4):590–600, 2011.

HP Duwe, J. Kaes, and E. Sackmann. Bending elastic moduli of lipid bilayers: modulation by solutes. *Journal de Physique*, 51(10):945–961, 1990.

O. Edholm and J.F. Nagle. Areas of molecules in membranes consisting of mixtures. *Biophysical journal*, 89(3):1827–1832, 2005.

E. Evans and A. Yeung. Hidden dynamics in rapid changes of bilayer shape. *Chem. Phys. Lipids*, 73:39–56, 1994.

A. Fischer, A. Franco, and T. Oberholzer. Giant vesicles as microreactors for enzymatic mrna synthesis. *ChemBioChem*, 3(5):409–417, 2002.

J B Fournier, N Khalifat, N Puff, and M I Angelova. Chemically triggered ejection of membrane tubules controlled by intermonolayer friction. *Phys. Rev. Lett.*, 102: 018102, 2009.

J.B. Fournier and P. Galatola. Critical fluctuations of tense fluid membrane tubules. *Physical review letters*, 98(1):18103, 2007.

H.H. Gerdes and R.N. Carvalho. Intercellular transfer mediated by tunneling nanotubes. *Curr. Opin Cell Biol.*, 20(4):470–475, 2008.

K. Giger, E.R. Lamberson, and J.S. Hovis. Formation of complex three-dimensional structures in supported lipid bilayers. *Langmuir*, 25(1):71–74, 2008.

H. Goldstein, C.P. Poole, and J.L. Safko. *Classical Mechanics*. Addison-Wesley, 2001.

I. Grosheva, A.S. Haka, C. Qin, L.M. Pierini, and F.R. Maxfield. Aggregated ldl in contact with macrophages induces local increases in free cholesterol levels that regulate local actin polymerization. *Arteriosclerosis, thrombosis, and vascular biology*, 29(10):1615–1621, 2009.

C.K. Haluska, K.A. Riske, V. Marchi-Artzner, J.M. Lehn, R. Lipowsky, and R. Dimova. Time scales of membrane fusion revealed by direct imaging of vesicle fusion with high temporal resolution. *Proceedings of the National Academy of Sciences*, 103(43):15841–15846, 2006.

J. Happel and H. Brenner. *Low Reynolds number hydrodynamics: with special applications to particulate media*, volume 1. Springer, 1965.

M.L. Henle and A.J. Levine. Hydrodynamics in curved membranes: The effect of geometry on particulate mobility. *Physical Review E*, 81(1):011905, 2010.

J.S. Hovis and S.G. Boxer. Patterning and composition arrays of supported lipid bilayers by microcontact printing. *Langmuir*, 17(11):3400–3405, 2001.

J.E.Marsden and T.J.R. Hughes. *The mathematical foundations of elasticity*. Prentice-Hall, 1983.

H. Jiang and T.R. Powers. Curvature-driven lipid sorting in a membrane tubule. *Physical review letters*, 101(1):18103, 2008.

P. Jönsson, J.P. Beech, J.O. Tegenfeldt, and F. Höök. Mechanical behavior of a supported lipid bilayer under external shear forces. *Langmuir*, 25(11):6279–6286, 2009.

P. Jonsson, J.P. Beech, J.O. Tegenfeldt, and F. Hook. Mechanical behavior of a supported lipid bilayer under external shear forces. *Langmuir*, 25:6279–6286, 2009.

F. Julicher and R. Lipowsky. Domain-induced budding of vesicles. *Phys. Rev. Lett.*, 70:2964–2967, 1993.

R. Karlsson, M. Karlsson, A. Karlsson, A.S. Cans, J. Bergenholtz, B. Akerman, A.G. Ewing, M. Voinova, and O. Orwar. Moving-wall-driven flows in nanofluidic systems. *Langmuir*, 18:4186–4190, 2002.

Nada Khalifat, Nicolas Puff, Stephanie Bonneau, Jean-Baptiste Fournier, and Miglena I. Angelova. Membrane deformation under local ph gradient: Mimicking mitochondrial cristae dynamics. *Biophys. J.*, 95(10):4924–4933, 2008.

N. Khatibzadeh, S. Gupta, B. Farrell, W.E. Brownell, and B. Anvari. Effects of cholesterol on nano-mechanical properties of the living cell plasma membrane. *Soft Matter*, 2012.

M.L. Klein and W. Shinoda. Large-scale molecular dynamics simulations of self-assembling systems. *Science*, 321(5890):798–800, 2008.

J. Kwik, S. Boyle, D. Fooksman, L. Margolis, M.P. Sheetz, and M. Edidin. Membrane cholesterol, lateral mobility, and the phosphatidylinositol 4, 5-bisphosphate-dependent organization of cell actin. *Proceedings of the National Academy of Sciences*, 100(24):13964–13969, 2003.

Heun Jin Lee, Eric L. Peterson, Rob Phillips, William S. Klug, and Paul A. Wiggins. Membrane shape as a reporter for applied forces. *Proc. Natl. Acad. Sci. U.S.A.*, 105(49):9253–19257, 2008.

Y. Li, R. Lipowsky, and R. Dimova. Membrane nanotubes induced by aqueous phase separation and stabilized by spontaneous curvature. *Proc. Natl. Acad. Sci. U.S.A.*, 108:4731–4736, 2011.

Zhiwei Li, Bahman Anvari, Masayoshi Takashima, Peter Brecht, Jorge H. Torres, and William E. Brownell. Membrane tether formation from outer hair cells with optical tweezers. *Biophys. J.*, 82:1386 – 1395, 2002.

R. Lipowsky. Spontaneous tubulation of membranes and vesicles reveals membrane tension generated by spontaneous curvature. *Faraday Discussions*, 2013.

TM MacRobert. Spherical harmonics. an elementary treatise on harmonic functions. *Bull. Amer. Math. Soc. 34 (1928), 779-780. DOI: 10.1090/S0002-9904-1928-04648-7 PII: S*, 2(9904):04648–7, 1928.

D. Marsh. Lateral pressure profile, spontaneous curvature frustration, and the incorporation and conformation of proteins in membranes. *Biophysical journal*, 93(11): 3884–3899, 2007.

J.C. Mathai, S. Tristram-Nagle, J.F. Nagle, and M.L. Zeidel. Structural determinants of water permeability through the lipid membrane. *J. Gen. Physiol.*, 131:69, 2008.

F.R. Maxfield and I. Tabas. Role of cholesterol and lipid organization in disease. *Nature*, 438(7068):612–621, 2005.

H.T. McMahon and J.L. Gallop. Membrane curvature and mechanisms of dynamic cell membrane remodelling. *Nature*, 438(7068):590–596, 2005.

R. Merkel, E. Sackmann, and E. Evans. Molecular friction and epitactic coupling between monolayers in supported bilayers. *J. Phys-Paris*, 50:1535–1555, 1989.

Ling Miao, Udo Seifert, Michael Wortis, and Hans-Günther Döbereiner. Budding transitions of fluid-bilayer vesicles: The effect of area-difference elasticity. *Phys. Rev. E*, 49:5389–5407, 1994.

S.T. Milner and SA Safran. Dynamical fluctuations of droplet microemulsions and vesicles. *Physical Review A*, 36(9):4371, 1987.

E Morris and U Homann. Cell surface area regulation and membrane tension. *J. Membr. Biol.*, (79-102), 179.

Martin Michael Müller. *Theoretical studies of fluid membrane mechanics*. PhD thesis, Johannes Gutenberg-Universitat in Mainz, 2007.

V. Noireaux and A. Libchaber. A vesicle bioreactor as a step toward an artificial cell assembly. *Proceedings of the National Academy of Sciences of the United States of America*, 101(51):17669–17674, 2004.

L.L. Norman, R.J. Oetama, M. Dembo, F. Byfield, D.A. Hammer, I. Levitan, and H. Aranda-Espinoza. Modification of cellular cholesterol content affects traction force, adhesion and cell spreading. *Cellular and molecular bioengineering*, 3(2): 151–162, 2010.

K. Olbrich, W. Rawicz, D. Needham, and E. Evans. Water permeability and mechanical strength of polyunsaturated lipid bilayers. *Biophys. J.*, 79:321–327, 2000.

J. Pan, S. Tristram-Nagle, and J.F. Nagle. Effect of cholesterol on structural and mechanical properties of membranes depends on lipid chain saturation. *Physical Review E*, 80(2):021931, 2009.

A. Papadopulos, S. Vehring, I. Lopez-Montero, L. Kutschenko, M. Stoeckl, P.F. Devaux, M. Kozlov, T. Pomorski, and A. Herrmann. Flippase activity detected with unlabeled lipids by shape changes of giant unilamellar vesicles. *J. Biol. Chem.*, 282: 15559–15568, 2007.

C. Peco, A. Rosolen, and M. Arroyo. An adaptive meshfree method for phase-field models of biomembranes, part ii: a lagrangian approach for membranes in viscous fluids. in preparation, 2012.

L. Piegl and W. Tiller. *The NURBS book*. Springer Verlag, 1997.

A. Pierres, V. Monnet-Corti, A.M. Benoliel, and P. Bongrand. Do membrane undulations help cells probe the world? *Trends in cell biology*, 19(9):428–433, 2009.

T. Pott and P. Meleard. The dynamics of vesicle thermal fluctuations is controlled by intermonolayer friction. *Europhys. Lett.*, 59:87–93, 2002.

T R Powers, G. Huber, and R E Goldstein. Fluid-membrane tethers: Minimal surfaces and elastic boundary layers. *Phys. Rev. E*, 65:041901, 2002.

C. Qin, T. Nagao, I. Grosheva, F.R. Maxfield, and L.M. Pierini. Elevated plasma membrane cholesterol content alters macrophage signaling and function. *Arteriosclerosis, thrombosis, and vascular biology*, 26(2):372–378, 2006.

M. Rahimi and M. Arroyo. Shape dynamics, lipid hydrodynamics, and the complex viscoelasticity of bilayer membranes. *Physical Review E*, 86(1):011932, 2012.

C Revenu, R Athman, S. Robine, and D. Louvard. The co-workers of actin filaments: from cell structures to signals. *Nat. Rev. Mol. Cell Biol.*, 5(635-646), 2004.

I. Reviakine and A Brisson. Formation of supported phospholipid bilayers from unilamellar vesicles investigated by atomic force microscopy. *Langmuir*, 16:1806–1815, 2000.

B.J. Reynwar, G. Illya, V.A. Harmandaris, M.M. Müller, K. Kremer, and M. Deserno. Aggregation and vesiculation of membrane proteins by curvature-mediated interactions rid b-2958-2009 rid b-3677-2009. *Nature*, 447:461–464, 2007.

R. Rodríguez-García, LR Arriaga, M. Mell, LH Moleiro, I. López-Montero, and F. Monroy. Bimodal spectrum for the curvature fluctuations of bilayer vesicles: pure bending plus hybrid curvature-dilation modes. *Physical review letters*, 102 (12):128101, 2009.

R. Rodríguez-García, M. Mell, I. López-Montero, J. Netzel, T. Hellweg, and F. Monroy. Polymersomes: smart vesicles of tunable rigidity and permeability. *Soft Matter*, 7(4):1532–1542, 2011.

O. Rossier, D. Cuvelier, N. Borghi, P.H. Puech, I. Derenyi, A. Buguin, P. Nassoy, and F. Brochard-Wyart. Giant vesicles under flows: Extrusion and retraction of tubes. *Langmuir*, 19:575–584, 2003.

A. Rustom, R. Saffrich, I. Markovic, P. Walther, and H.H. Gerdes. Nanotubular highways for intercellular organelle transport. *Science*, 303:1007–1010, 2004.

P. G. Saffman and M. Delbrück. Brownian motion in biological membranes. *Proc. Natl. Acad. Sci. U.S.A.*, 72(8):3111–3113, 1975.

Q. Saleem, B. Liu, C.C. Gradinaru, and P.M. Macdonald. Lipogels: Single-lipid-bilayer-enclosed hydrogel spheres. *Biomacromolecules*, 12(6):2364–2374, 2011.

H. Schönherr, J.M. Johnson, P. Lenz, C.W. Frank, and S.G. Boxer. Vesicle adsorption and lipid bilayer formation on glass studied by atomic force microscopy. *Langmuir*, 20(26):11600–11606, 2004. doi: 10.1021/la049302v.

US Schwarz and G. Gompper. Systematic approach to bicontinuous cubic phases in ternary amphiphilic systems. *Physical Review E*, 59(5):5528, 1999.

L.E. Scriven. Dynamics of a fluid interface: equations of motion for newtonian surface fluids. *Chem. Eng. Sci.*, 12:98–108, 1960.

U. Seifert. Configurations of fluid membranes and vesicles. *Advances in Physics*, 46: 13–137, 1997.

U. Seifert and S. A. Langer, S. A. Viscous modes of fluid bilayer membranes. *Europhys. Lett.*, 23(1):71–76, 1993.

U. Seifert and R. Lipowsky. *Handbook of Biological Physics*, volume 1, chapter Morphology of Vesicles. Elsevier Science B.V., 1995.

P. Sens. Dynamics of nonequilibrium membrane bud formation. *Phys. Rev. Lett.*, 93: 108103, 2004.

Pierre Sens and Nir Gov. Force balance and membrane shedding at the red-blood-cell surface. *Phys. Rev. Lett.*, 98:018102, Jan 2007.

F. Sevšek. Membrane elasticity from shape fluctuations of phospholipid vesicles. *Advances in Planar Lipid Bilayers and Liposomes*, 12:1, 2010.

L.F. Shampine, M.W. Reichelt, and J.A. Kierzenka. Solving index-i daes in matlab and simulink. *Siam Rev.*, pages 538–552, 1999.

Y. Shibata, J. Hu, M. M. Kozlov, and Tom A. Rapoport. Mechanisms shaping the membranes of cellular organelles. *Annu. Rev. Cell Dev. Bi.*, 25:329–354, 2009.

S.A. Shkulipa, W.K. den Otter, and W.J. Briels. Thermal undulations of lipid bilayers relax by intermonolayer friction at submicrometer length scales. *Phys. Rev. Lett.*, 96:178302, 2006.

K. Simons and W.L.C. Vaz. Model systems, lipid rafts, and cell membranes 1. *Annu. Rev. Biophys. Biomol. Struct.*, 33:269–295, 2004.

B. Sorre, A. Callan-Jones, J. Manzi, B. Goud, J. Prost, P. Bassereau, and A. Roux. Nature of curvature coupling of amphiphysin with membranes depends on its bound density. *Proceedings of the National Academy of Sciences*, 109(1):173–178, 2012.

S. Sowinski, C. Jolly, O. Berninghausen, M.A. Purbhoo, A. Chauveau, K. Kohler, S. Oddos, P. Eissmann, F.M. Brodsky, C. Hopkins, et al. Membrane nanotubes physically connect t cells over long distances presenting a novel route for hiv-1 transmission. *Nat. Cell Biol.*, 10:211–219, 2008.

H. Sprong, P. van der Sluijs, and G. van Meer. How proteins move lipids and lipids move proteins. *Nat. Rev. Mol. Cell. Bio.*, 2:504–513, 2001.

M. Staykova, D.P. Holmes, C. Read, and H.A. Stone. Mechanics of surface area regulation in cells examined with confined lipid membranes. *Proc. Natl. Acad. Sci. U.S.A.*, 108:9084–9088, 2011.

M. Staykova, M. Arroyo, M. Rahimi, and H.A. Stone. Confined bilayers passively regulate shape and stress. *Physical Review Letters*, 110(2):028101, 2013.

H.A. Stone and A. Ajdari. Hydrodynamics of particles embedded in a flat surfactant layer overlying a subphase of finite depth. *Journal of Fluid Mechanics*, 369:151–174, 1998.

S. Svetina. Vesicle budding and the origin of cellular life. *Chem. Phys. Chem.*, 10: 2769–2776, 2009.

P.S. Swain and D. Andelman. Supported membranes on chemically structured and rough surfaces. *Phys. Rev. E*, 63:051911, 2001.

I. Tabas. Cholesterol and phospholipid metabolism in macrophages. *Biochimica et Biophysica Acta (BBA)-Molecular and Cell Biology of Lipids*, 1529(1):164–174, 2000.

D. Thid, J.J. Benkoski, S. Svedhem, B. Kasemo, and J. Gold. Dha-induced changes of supported lipid membrane morphology. *Langmuir*, 23(11):5878–5881, 2007.

I. Tsafrir, Y. Caspi, M A Guedeau-Boudeville, T. Arzi, and J. Stavans. Budding and tubulation in highly oblate vesicles by anchored amphiphilic molecules. *Phys. Rev. Lett.*, 91:138102, 2003.

T. Ursell, A. Agrawal, and R. Phillips. Lipid bilayer mechanics in a pipette with glass-bilayer adhesion. *Biophysical journal*, 101(8):1913–1920, 2011.

M.C. Watson and F.L.H. Brown. Interpreting membrane scattering experiments at the mesoscale: The contribution of dissipation within the bilayer. *Biophysical journal*, 98(6):L9–L11, 2010.

R.E. Waugh. Surface viscosity measurements from large bilayer vesicle tether formation .2. experiments. *Biophys. J.*, 38:29–37, 1982.

A. Yeung and E. Evans. Unexpected dynamics in shape fluctuations of bilayer vesicles. *Journal de Physique II*, 5(10):1501–1523, 1995.

R. Zidovetzki and I. Levitan. Use of cyclodextrins to manipulate plasma membrane cholesterol content: evidence, misconceptions and control strategies. *Biochimica et Biophysica Acta (BBA)-Biomembranes*, 1768(6):1311–1324, 2007.

Appendix A

General calculations of the continuum model

A.1 Surface stress tensor

To determine the Cauchy surface stress tensor, we follow the method presented in Capovilla and Guven [2002] based on the principle of virtual work, see also Müller [2007]. Suppose that the free energy of the bilayer is given by

$$\Pi = \int_{\Gamma} f(\boldsymbol{g}, \boldsymbol{k})\, dS,$$

where $f(\boldsymbol{g}, \boldsymbol{k})$ is the free energy per unit area. Then, the general expression for the elastic surface stress tensor is

$$\sigma^{ab} = \underbrace{\mathscr{T}^{ab} + \mathscr{H}^{ac} k_c^b}_{\sigma_{\parallel}^{ab}} - \underbrace{\nabla_c \mathscr{H}^{ac} n^b}_{\sigma_{\perp}^{ab}}, \tag{A.1}$$

where

$$\begin{aligned} \mathscr{T}^{ab} &= \frac{2}{\sqrt{g}} \frac{\partial \left(\sqrt{g} f\right)}{\partial g_{ab}}, \\ \mathscr{H}^{ab} &= \frac{\partial f}{\partial k_{ab}}, \end{aligned}$$

and g is the determinant of the metric tensor. We have changed the sign in the definition of this stress tensor as compared to the references above to be consistent with the Doyle-Ericksen formula J.E.Marsden and Hughes [1983] and the usual convention, by which positive tractions are tensile. Note also our different sign convention in defining the second fundamental form. When dotted with a unit tangential vector to the surface and normal to a curve on it $\boldsymbol{l}$, this tensor provides the tractions along this curve $l^c g_{ca}\sigma_{\parallel}^{ab}$ and $l^c g_{ca}\sigma_{\perp}^{ab}$, tangential and normal to the surface Müller [2007].

We have

$$\begin{aligned} \frac{\partial\sqrt{g}}{\partial g_{ab}} &= \frac{1}{2}\sqrt{g}g^{ab}, \quad 2\frac{\partial H}{\partial g_{ab}} = -k^{ab}, \\ 2\frac{\partial H}{\partial k_{ab}} &= g^{ab}, \quad \frac{\partial \rho^{\pm}}{\partial g_{ab}} = -\frac{1}{2}\rho^{\pm}g^{ab}. \end{aligned}$$

where the last equation comes from differentiating the following statement of balance of mass $\rho^{\pm}\sqrt{g} = \text{cst}$. In the present case,

$$f = \kappa\left(2H - C_0\right)^2/2 + K_s\left(\rho^{\pm}/\rho_0 \mp 2dH - 1\right)^2/2,$$

leading to

$$\begin{aligned} \sigma_{\parallel}^{ab} &= f g^{ab} - \kappa(2H - C_0)k^{ab} \\ &\quad -K_s\left(\frac{\rho^{\pm}}{\rho_0} - 1 \mp 2dH\right)\left(\frac{\rho^{\pm}}{\rho_0}g^{ab} \pm dk^{ab}\right) \end{aligned} \tag{A.2}$$

which is symmetric as expected, and to

$$\sigma_{\perp}^{ab} = -2\kappa\nabla^a H n^b \pm dK_s\nabla^a\left(\frac{\rho^{\pm}}{\rho_0} \mp 2dH\right)n^b. \tag{A.3}$$

In both expressions, there is an implied summation on the two monolayers contributions. The stretching term usually dominates the in-plane stress tensor. For moderate

density variations and bilayer curvature, this results in the familiar expression

$$\boldsymbol{\sigma}_{\parallel} \approx -K_s \left(\frac{\hat{\rho}^{\pm}}{\rho_0} - 1 \right) \boldsymbol{g}.$$

Also note that for uniform bilayers, e.g. spheres or tubes with uniform lipid density, $\boldsymbol{\sigma}_{\perp} = 0$.

A.2 General variations of the mean curvature and the element of area

The Willmore (Helfrich) energy depends exclusively on the shape of the surface, hence the only relevant variations are those normal to the surface as the tangential variations do not change the shape. This reparameterization invariance is systematically exploited when computing the Euler-Lagrange equations for this energy. In the present setting, we need to consider general variations of the extensional energy, where the mean curvature and the element of area appear. This energy is not invariant with respect to tangential variations, hence to compute its variations we need to develop formulas for the general variations of the area element and the mean curvature. Our surface is parameterized by $\boldsymbol{x}(u^i)$. The natural basis of the tangent to the manifold are $\boldsymbol{x}_{,i}$ and the unit normal is denoted by $\boldsymbol{n}$. The subindex preceded by a comma $,i$ means partial differentiation with respect to u^i, while ∇_i denotes covariant differentiation. The components of the metric tensor on the surface can be computed as $g_{ij} = \langle \boldsymbol{x}_{,i}, \boldsymbol{x}_{,j} \rangle$. We recall the Gauss equations

$$\boldsymbol{x}_{,ij} = \Gamma^k_{ij} \boldsymbol{x}_{,k} + h_{ij} \boldsymbol{n}$$

where Γ^k_{ij} are the symbols of the Riemannian connection, and $h_{ij} = -\langle \boldsymbol{n}_{,i}, \boldsymbol{x}_{,j} \rangle = \langle \boldsymbol{n}, \boldsymbol{x}_{,ij} \rangle$ are the components of the second fundamental form. We recall that for a scalar field, $\nabla_i f = f_{,i}$ and for a vector field $\nabla_i a^j = a^j_{,i} + a^k \Gamma^j_{ki}$. The Laplace-Beltrami

operator can be computed as $\Delta a = g^{ij}\nabla_i\nabla_j a$. For convenience, we replace variations by rates, and the dot is a time-derivative or variation for fixed values of u^i. A general variation of the shape can be written as

$$\dot{\boldsymbol{x}} = v_n\boldsymbol{n} + \boldsymbol{t},$$

where v_n and $\boldsymbol{t}$ are scalar and vector fields on the surface. We represent the tangential variation as $\boldsymbol{t} = t^i\boldsymbol{x}_{,i}$.

As for the element of area, it is classical that

$$\dot{dS} = (\mathrm{d}iv\ \boldsymbol{t} - v_n H)\ dS,$$

where $H = h_{ij}g^{ij}$ is the mean curvature.

Let us move now to the variations of the mean curvature. We have

$$\dot{\boldsymbol{x}}_{,i} = (v_n)_{,i}\boldsymbol{n} + v_n\boldsymbol{n}_{,i} + \boldsymbol{t}_{,i},$$

where

$$\boldsymbol{t}_{,j} = t^i\boldsymbol{x}_{,ij} + t^i_{,j}\boldsymbol{x}_{,i}.$$

Therefore, recalling that $\langle\boldsymbol{x}_{,i},\boldsymbol{n}\rangle = 0$ and $\langle\boldsymbol{n}_{,i},\boldsymbol{n}\rangle = 0$, we have

$$\begin{aligned}
\dot{g}_{ij} &= \langle\dot{\boldsymbol{x}}_{,i},\boldsymbol{x}_{,j}\rangle + \langle\boldsymbol{x}_{,i},\dot{\boldsymbol{x}}_{,j}\rangle = v_n\langle\boldsymbol{n}_{,i},\boldsymbol{x}_{,j}\rangle + v_n\langle\boldsymbol{x}_{,i},\boldsymbol{n}_{,j}\rangle + \langle\boldsymbol{x}_{,i},\boldsymbol{t}_{,j}\rangle + \langle\boldsymbol{x}_{,j},\boldsymbol{t}_{,i}\rangle \\
&= -2v_n h_{ij} + \langle\boldsymbol{x}_{,i},\boldsymbol{t}_{,j}\rangle + \langle\boldsymbol{x}_{,j},\boldsymbol{t}_{,i}\rangle \\
&= -2v_n h_{ij} + g_{ik}\nabla_j t^k + g_{jk}\nabla_i t^k.
\end{aligned}$$

The last step follows from the fact that the covariant derivative is the tangent pro-

jection of the partial derivative, and can be checked directly

$$\begin{aligned}\langle \boldsymbol{x}_{,i}, \boldsymbol{t}_{,j}\rangle &= \langle \boldsymbol{x}_{,i}, t^k \boldsymbol{x}_{,kj}\rangle + \langle \boldsymbol{x}_{,i}, t^k_{,j}\boldsymbol{x}_{,k}\rangle = t^k\langle \boldsymbol{x}_{,i}, \Gamma^l_{kj}\boldsymbol{x}_{,l} + h_{kj}\boldsymbol{n}\rangle + t^k_{,j}g_{ik}\\ &= g_{ik}(t^k_{,j} + \Gamma^k_{lj}t^l) = g_{ik}\nabla_j t^k.\end{aligned}$$

Since $g_{ij}g^{jk} = \delta^k_i$, we have $\dot{g}^{lk} = -g^{li}\dot{g}_{ij}g^{jk}$ and consequently

$$\dot{g}^{ij} = 2v_n h^{ij} - g^{ik}\nabla_k t^j - g^{jk}\nabla_k t^i.$$

Now, since $\langle \boldsymbol{n}, \boldsymbol{x}_{,i}\rangle = 0$, it follows that $\langle \dot{\boldsymbol{n}}, \boldsymbol{x}_{,i}\rangle + \langle \boldsymbol{n}, \dot{\boldsymbol{x}}_{,i}\rangle = 0$, hence

$$\begin{aligned}\langle \dot{\boldsymbol{n}}, \boldsymbol{x}_{,i}\rangle &= -\langle \boldsymbol{n}, (v_n)_{,i}\boldsymbol{n} + v_n\boldsymbol{n}_{,i} + t^j\boldsymbol{x}_{,ij} + t^j_{,i}\boldsymbol{x}_{,j}\rangle\\ &= -(v_n)_{,i} - t^j\langle \boldsymbol{n}, \boldsymbol{x}_{,ij}\rangle = -(v_n)_{,i} - t^j h_{ij}.\end{aligned}$$

Also, since the normal is a unit vector, we have $\langle \dot{\boldsymbol{n}}, \boldsymbol{n}\rangle = 0$. Now, recalling the Gauss equations, we have

$$\langle \dot{\boldsymbol{n}}, \boldsymbol{x}_{,ij}\rangle = \langle \dot{\boldsymbol{n}}, \Gamma^k_{ij}\boldsymbol{x}_{,k} + h_{ij}\boldsymbol{n}\rangle = \Gamma^k_{ij}[-(v_n)_{,k} - t^l h_{kl}].$$

A direct calculation shows that

$$\dot{\boldsymbol{x}}_{,ij} = (v_n)_{,ij}\boldsymbol{n} + (v_n)_{,i}\boldsymbol{n}_{,j} + (v_n)_{,j}\boldsymbol{n}_{,i} + +(v_n)\boldsymbol{n}_{,ij} + t^k_{,j}\boldsymbol{x}_{,ki} + t^k_{,i}\boldsymbol{x}_{,kj} + t^k_{,ij}\boldsymbol{x}_{,k} + t^k\boldsymbol{x}_{,kij}.$$

Hence,

$$\begin{aligned}\langle \dot{\boldsymbol{x}}_{,ij}, \boldsymbol{n}\rangle &= (v_n)_{,ij} + v_n\langle \boldsymbol{n}, \boldsymbol{n}_{,ij}\rangle + t^k_{,j}\langle \boldsymbol{n}, \boldsymbol{x}_{,ki}\rangle + t^k_{,i}\langle \boldsymbol{n}, \boldsymbol{x}_{,kj}\rangle + t^k\langle \boldsymbol{n}, \boldsymbol{x}_{,kij}\rangle\\ &= (v_n)_{,ij} - v_n h_{ik}h^k_j + t^k_{,j}h_{ki} + t^k_{,i}h_{kj} + t^k(\nabla_k h_{ij} + \Gamma^l_{ki}h_{jl} + \Gamma^l_{kj}h_{li} + \Gamma^l_{ij}h_{lk}),\end{aligned}$$

where we have used the fact that,

$$\langle \boldsymbol{n}, \boldsymbol{x}_{,kij} \rangle = \nabla_k h_{ij} + \Gamma^l_{ki} h_{jl} + \Gamma^l_{kj} h_{li} + \Gamma^l_{ij} h_{lk},$$

which follows from the definition of $\nabla_j h_{ki}$, differentiating twice the relation $\langle \boldsymbol{n}, \boldsymbol{x}_i \rangle = 0$, the Gauss equation, and the Codazzi-Mainardi equations $\nabla_j h_{ki} = \nabla_k h_{ij} = \nabla_i h_{jk}$. Thus, we have

$$\begin{aligned}
\dot{h}_{ij} &= \langle \dot{\boldsymbol{n}}, \boldsymbol{x}_{ij} \rangle + \langle \boldsymbol{n}, \dot{\boldsymbol{x}}_{ij} \rangle \\
&= -(v_n)_{,k} \Gamma^k_{ij} - t^l h_{kl} \Gamma^k_{ij} \\
&\quad + (v_n)_{,ij} - v_n h_{ik} h^k_j + t^k_{,j} h_{ki} + t^k_{,i} h_{kj} + t^k (\nabla_k h_{ij} + \Gamma^l_{ki} h_{jl} + \Gamma^l_{kj} h_{li} + \Gamma^l_{ij} h_{lk}) \\
&= \nabla_i \nabla_j v_n - v_n h_{ik} h^k_j + t^k \nabla_k h_{ij} + h_{ki} \nabla_j t^k + h_{kj} \nabla_i t^k.
\end{aligned}$$

Finally, a straightforward calculation shows that

$$\dot{H} = \dot{g}^{ij} h_{ij} + g^{ij} \dot{h}_i j = \Delta v_n + v_n h^{ij} h_{ij} + t^k \nabla_k H = \Delta v_n + v_n (H^2 - 2K) + t^k \nabla_k H.$$

The contribution of the tangential velocity is a purely convective term, which could have been guessed a priori by noting that the tangential variations do not change the geometric surface.

A.3 Membrane dissipation for axisymmetric surfaces

We first compute the following terms of Eq. (2.13) for axisymmetric surfaces, dropping the superindex $\pm$ for simplicity

$$\begin{aligned}
\boldsymbol{d}:\boldsymbol{d} &= \left(\frac{1}{a}v'\right)^2+\left(\frac{r'}{ar}v\right)^2-\frac{2}{a}v_n\left(\frac{b}{a^3}v'+\frac{z'r'}{ar^2}v\right)\\
&\quad +(4H^2-2K)v_n^2\\
&= \frac{1}{a^2}v'^2+\left(\frac{r'}{ar}\right)^2v^2+\frac{2z'b}{a^5}r_{,t}v'+\frac{2z'^2r'}{r^2a^3}r_{,t}v\\
&\quad -\frac{2r'b}{a^5}z_{,t}v'-\frac{2r'^2z'}{r^2a^3}z_{,t}v+\frac{(4H^2-2K)z'^2}{a^2}{r_{,t}}^2\\
&\quad +\frac{(4H^2-2K)r'^2}{a^2}{z_{,t}}^2-\frac{2(4H^2-2K)r'z'}{a^2}r_{,t}z_{,t},
\end{aligned}$$

$$\begin{aligned}
(\mathrm{tr}\ \boldsymbol{d})^2 &= \left(\frac{(rv)'}{ra}-2v_nH\right)^2\\
&= \frac{1}{a^2}v'^2+\left(\frac{r'}{ar}\right)^2v^2+\frac{4z'H}{a^2}r_{,t}v'+\frac{4z'r'H}{ra^2}r_{,t}v\\
&\quad -\frac{4r'H}{a^2}z_{,t}v'-\frac{4r'^2H}{ra^2}z_{,t}v+2\frac{r'}{ra^2}vv'\\
&\quad +\frac{4H^2z'^2}{a^2}{r_{,t}}^2+\frac{4H^2r'^2}{a^2}{z_{,t}}^2-\frac{8H^2r'z'}{a^2}r_{,t}z_{,t}.
\end{aligned}$$

By substituting the above relations into Eq. (2.13), we can identify the nonzero components of the matrix $\mathbf{A}$ as

$$A_{11}=4\mu_s\frac{(4H^2-2K)z'^2}{a^2}+8\lambda_s\frac{H^2z'^2}{a^2}$$

$$A_{12}=-4\mu_s\frac{(4H^2-2K)r'z'}{a^2}-8\lambda_s\frac{H^2r'z'}{a^2}$$

$$A_{13} = A_{14} = 2\mu_s \frac{z'^2 r'}{r^2 a^3} + 2\lambda_s \frac{z' r' H}{r a^2}$$

$$A_{15} = A_{16} = 2\mu_s \frac{z' b}{a^5} + 2\lambda_s \frac{z' H}{a^2}$$

$$A_{22} = 4\mu_s \frac{(4H^2 - 2K) r'^2}{a^2} + 8\lambda_s \frac{H^2 r'^2}{a^2}$$

$$A_{23} = A_{24} = -2\mu_s \frac{r'^2 z'}{r^2 a^3} - 2\lambda_s \frac{r'^2 H}{r a^2}$$

$$A_{33} = A_{44} = (2\mu_s + \lambda_s) \left(\frac{r'}{ar} \right)^2$$

$$A_{25} = A_{26} = -2\mu_s \frac{r' b}{a^5} - 2\lambda_s \frac{r' H}{a^2}$$

$$A_{35} = A_{46} = \lambda_s \frac{r'}{r a^2}$$

$$A_{55} = A_{66} = (2\mu_s + \lambda_s) \frac{1}{a^2}$$

A.4 Variation of elastic energy for axisymmetric surfaces

Recalling definitions and the continuity equation, simple calculations show that

$$\begin{aligned}
H_{,t} &= \frac{\partial H}{\partial r} r_{,t} + \frac{\partial H}{\partial r'} r'_{,t} + \frac{\partial H}{\partial r''} r''_{,t} + \frac{\partial H}{\partial z'} z'_{,t} + \frac{\partial H}{\partial z''} z''_{,t}, \\
a_{,t} &= \frac{r'}{a} r'_{,t} + \frac{z'}{a} z'_{,t}, \\
\rho^{\pm}_{,t} &= -\left(\frac{\rho^{\pm} r'}{ra} + \frac{\rho^{\pm\prime}}{a} \right) v^{\pm} - \frac{\rho^{\pm}}{a} v^{\pm\prime} \\
&\quad + \left(\frac{\rho^{\pm\prime} r'}{a^2} - \frac{2\rho^{\pm} z' H}{a} \right) r_{,t} + \left(\frac{\rho^{\pm\prime} z'}{a^2} + \frac{2\rho^{\pm} r' H}{a} \right) z_{,t}
\end{aligned}$$

and

$$\begin{aligned} 2\frac{\partial H}{\partial r} &= -\frac{z'}{ar^2}, \quad 2\frac{\partial H}{\partial r'} = \frac{z''}{a^3} - \frac{3br'}{a^5}, \quad 2\frac{\partial H}{\partial r''} = -\frac{z'}{a^3}, \\ 2\frac{\partial H}{\partial z'} &= -\frac{r''}{a^3} - \frac{3bz'}{a^5} + \frac{r'^2}{a^3 r}, \quad 2\frac{\partial H}{\partial z''} = \frac{r'}{a^3}. \end{aligned}$$

Appendix B

General calculations for numerical approximation

B.1 Space discretization of the continuity equation

Following a standard SUPG stabilization method, the weight functions for the continuity equation are $(\tilde{B}_I + \tau \boldsymbol{c} \cdot \nabla \tilde{B}_I)$, where $\tau = h/(2\|\boldsymbol{c}\|)$ and h is the grid size. We rewrite the continuity equation in (2.23) as

$$\rho^{\pm}_{,t} + s^{\pm}\rho^{\pm} + c^{\pm}\rho^{\pm\prime} = 0, \tag{B.1}$$

where

$$\begin{aligned} s^{\pm} &= \frac{v^{\pm}r'}{ra} + \frac{v^{\pm\prime}}{a} + \frac{2z'Hr_{,t}}{a} - \frac{2r'Hz_{,t}}{a}, \\ c^{\pm} &= \frac{v^{\pm}}{a} - \frac{r'r_{,t}}{a^2} - \frac{z'z_{,t}}{a^2}. \end{aligned}$$

By replacing Eqs. (3.2,3.3) in the equation above and multiplying by the SUPG weight functions, we obtain for each monolayer the discrete form of the continuity equation

$$(\mathbf{M}^{\pm} + \mathbf{M}^{stb\pm})\dot{\boldsymbol{\rho}}^{\pm} + (\mathbf{L}_1^{\pm} + \mathbf{L}_2^{\pm} + \mathbf{L}_1^{stb\pm} + \mathbf{L}_2^{stb\pm})\boldsymbol{\rho}^{\pm} = 0, \tag{B.2}$$

where

$$M^{\pm}{}_{IJ} = \int_{\Gamma} \tilde{B}_I \tilde{B}_J dS, \quad M^{stb\pm}_{IJ} = \int_{\Gamma} \tau c^{\pm} \tilde{B}'_I \tilde{B}_J dS,$$
$$L^{\pm}_{1\,IJ} = \int_{\Gamma} \tilde{B}_I s^{\pm} \tilde{B}_J dS, \quad L^{\pm}_{2\,IJ} = \int_{\Gamma} \tilde{B}_I c^{\pm} \tilde{B}'_J dS$$
$$L_1^{stb\pm}{}_{IJ} = \int_{\Gamma} \tau c^{\pm} \tilde{B}'_I s^{\pm} \tilde{B}_J dS,$$
$$L_2^{stb\pm}{}_{IJ} = \int_{\Gamma} \tau c^{\pm} \tilde{B}'_I c^{\pm} \tilde{B}'_J dS.$$

Note that the $\mathbf{M}$ and $\mathbf{L}$ matrices depend on $\dot{\mathbf{P}}$ and $\mathbf{V}$.

Appendix C

Protrusions out of confined bilayers upon compression

C.1 Linear stability analysis of the planar state

The planar state is never the absolute minimizer of the free energy in the region $\varepsilon_c > 0, v > 1$. Nevertheless, this state is experimentally observed in samples under compression and hypo-osmotic stress. This fact is explained by the relative stability of the planar configuration below a threshold, with a significant energy barrier to transition from the planar state to the protruded one. We assess now the parameter range where planar configurations are, at least, local minimizers of the free energy. A standard technique to estimate the onset of the instability, or buckling, is the linearized stability analysis. Since real systems are subject to thermal fluctuations and imperfection, the analysis below provides an upper bound of the critical strain (tension) and reduced volume (pressure difference).

We consider an infinite adhered bilayer and analyze the stability of planar harmonic disturbances. The system may be reduced to one dimension, and we adopt a Monge representation $z(x)$ of the bilayer mid surface, where x is parallel to the substrate. We linearize the free energy density of the system in Eq. (5.3) of the main text about the equilibrium state given by Eqs. (5.5,5.8), with the equilibrium membrane tension σ and pressure difference Δp as dead loads (by adding $\sigma - z\Delta p$ to f). We expand the mid surface height as $z = t + \delta z$, and compute the energy disturbance relative to the

equilibrium energy up to second order as

$$\delta f_{planar} \approx \frac{\kappa}{2}(\delta z'')^2 + \frac{U''(t)}{2}\delta z^2 + \frac{\sigma}{2}(\delta z')^2.$$

Expanding the height with a Fourier representation, $\delta z = \int \delta z_q \exp(iqx)dq$, the energy density of the $q-$th mode becomes

$$f_q = \frac{1}{2}\left[\kappa q^4 + U''(t) + \sigma q^2\right]\delta z_q^2.$$

Note that for $q > 0$, the modes leave the enclosed volume unchanged. This mode will go unstable if this energy becomes degenerate, yielding the condition

$$\sigma = -\kappa q^2 - \frac{U''(t)}{q^2}.$$

It is clear from this equation that the bending stiffness has a stabilizing effect, while the compressive tension destabilizes the uniform state. Depending on the separation t, the bilayer-substrate potential has a stabilizing or destabilizing effect. When $U''(t) < 0$, i.e. when $t > t_d$, the adhesion potential is unstable and the analysis predicts that uniform states are unstable irrespective of the membrane tension. When $U''(t) \geq 0$, to find the buckling tension, i.e. the lowest tension for which disturbances can grow, we maximize σ with respect to q since buckling tensions are expected to be negative. We obtain

$$q_{cr} = \sqrt[4]{\frac{U''(t)}{\kappa}} \quad \text{and} \quad \sigma = -2\sqrt{\kappa\ U''(t)}$$

Replacing the expressions for σ and t, we find

$$\frac{K_s\varepsilon_c}{1-\varepsilon_c} = \sqrt{\kappa\ U''\left(\frac{t_0 v}{1+\varepsilon}\right)},$$

which implicitly gives a relation between ε_c and v defining the boundary of the region where the planar state is metastable, when $\varepsilon_c < \varepsilon_{c,cr}(v)$, or conversely when $v <$

$v_{cr}(\varepsilon_c)$. This region is shown in black in the phase diagram (Fig 5.3).

Alternatively, the region of marginal stability of the planar state can be expressed in terms of the membrane tension σ and the pressure difference Δp. Indeed, by computing the separation from the pressure difference, $t = \mathcal{V}'^{-1}(\Delta p)$ (this can be done for $0 < t < t_d$), and plugging this expression into $\sigma = -2\sqrt{\kappa\, U''(t)}$, we obtain an implicit relation between σ and Δp that sets the boundary of the stability region.

The analysis above assumes that, in assessing the energetics of a shape disturbance, the resulting density disturbances have sufficient time to relax by inter-monolayer slippage. This is a reasonable assumption if the disturbances are due to geometric imperfections of the substrate. If the shape disturbances are highly transient, e.g. due to thermal fluctuations, then κ should be replaced by $\bar{\kappa} = \kappa + 2d^2 K_s$ resulting in a higher critical tension by a factor of about 1.8.

Appendix D

Vesicular and tubular membrane fluctuations

D.1 Elastic energy calculations: spherical coordinates

Using Eqs. (7.1), we compute the following expressions, which will be used in the total elastic energy,

$$\begin{aligned}
2H &= \frac{2}{R_0} - \frac{2h}{R_0^2} - \boldsymbol{\nabla}_s^2 h + \frac{2h^2}{R_0^3} + \frac{2h}{R_0}\boldsymbol{\nabla}_s^2 h + \mathscr{O}(h^3), \\
\mathrm{d}A &= \left(R_0^2 + 2R_0 h + h^2 + \frac{R_0^2}{2}|\boldsymbol{\nabla}_s h|^2 + \mathscr{O}(h^3)\right)\sin\varphi\; d\varphi\; d\theta \\
2H\;\mathrm{d}A &= \left(2R_0 + 2h - R_0^2\boldsymbol{\nabla}_s^2 h + R_0|\boldsymbol{\nabla}_s h|^2 + \mathscr{O}(h^3)\right)\sin\varphi\; d\varphi\; d\theta, \\
4H^2\;\mathrm{d}A &= \left(4 - 4R_0\boldsymbol{\nabla}_s^2 h + 4h\boldsymbol{\nabla}_s^2 h + 2|\boldsymbol{\nabla}_s h|^2 + R_0^2\boldsymbol{\nabla}_s^2 h\boldsymbol{\nabla}_s^2 h + \mathscr{O}(h^3)\right)\sin\varphi\; d\varphi\; d\theta.
\end{aligned}$$

where

$$\boldsymbol{\nabla}_s^2 h = \frac{1}{h^2\sin^2\varphi}\left(h_{\theta\theta} + h_\varphi \sin\varphi\cos\varphi + h_{\varphi\varphi}\sin^2\varphi\right),$$

$$\boldsymbol{\nabla}_s h = \frac{1}{h\sin\varphi}\left(h_\theta \hat{\boldsymbol{e}}_\theta + h_\varphi \sin\varphi \hat{\boldsymbol{e}}_\varphi\right),$$

and

$$|\boldsymbol{\nabla}_s h|^2 = \frac{1}{h^2 \sin^2\varphi}\left(h_\theta^2 + h_\varphi^2 \sin^2\varphi\right).$$

Using the above expressions, we rewrite the total elastic energy by considering the first and second order terms

$$\begin{aligned}
\Pi &= pR_0 \sum_{n,m} |h_{nm}|^2 + \frac{\tilde{\kappa}}{2}\left(\sum_{n,m} \frac{\xi_n^2 - 2\xi_n}{R_0^2}|h_{nm}|^2\right) \\
&+ K_s \sum_{n,m}\left(\hat{\rho_0}\frac{\xi_n + 2}{2}|h_{nm}|^2 + R_0^2|\rho_{nm}|^2 + R_0^2|\bar{\rho}_{nm}|^2\right) \\
&- 2dK_s \sum_{n,m}\left(\rho_0 \frac{\xi_n}{R_0}|h_{nm}|^2 + \frac{\xi_n + 2}{2}(\rho_{nm}h_{nm}^* + \rho_{nm}^* h_{nm})\right) \\
&+ \sum_{n,m} R_0\left(2K_s\rho_0 + \gamma\right)(\rho_{nm}h_{nm}^* + \rho_{nm}^* h_{nm}) + R_0\left(2K_s\bar{\rho}_0 + \bar{\gamma}\right)(\bar{\rho}_{nm}h_{nm}^* + \bar{\rho}_{nm}^* h_{nm})
\end{aligned}$$

D.2 Calculations in vector spherical harmonic

Introducing the velocity field on the membrane in the spherical coordinates, $\boldsymbol{V}(\varphi,\theta;t) = v_r\hat{\boldsymbol{e}}_r + v_\varphi\hat{\boldsymbol{e}}_\varphi + v_\theta\hat{\boldsymbol{e}}_\theta$, and rephrased in the vector spherical harmonic (VSH) we have [Barrera et al., 2000]

$$\boldsymbol{V}(\varphi,\theta;t) = \sum_{n,m}\left(v^r{}_{nm}\boldsymbol{Y}_{nm} + v_{nm}^{(1)}\boldsymbol{\Psi}_{nm} + v_{nm}^{(2)}\boldsymbol{\Phi}_{nm}\right) \tag{D.1}$$

where $\boldsymbol{Y}_{nm} = Y_{nm}\hat{\boldsymbol{e}}_r$, $\boldsymbol{\Psi}_{nm} = R_0\boldsymbol{\nabla}_s Y_{nm}$, $\boldsymbol{\Phi}_{nm} = \hat{\boldsymbol{e}}_r \times \boldsymbol{\Psi}_{nm}$, and

$$
\begin{aligned}
v^r &= \sum_{n,m} {v^r}_{nm} Y_{nm}, \\
v_\varphi &= \sum_{n,m} v^{(1)}_{nm} Y_{nm,\varphi} - \sum \frac{v^{(2)}_{nm}}{\sin\varphi} Y_{nm,\theta}, \\
v_\theta &= \sum_{n,m} \frac{v^{(1)}_{nm}}{\sin\varphi} Y_{nm,\theta} + \sum v^{(2)}_{nm} Y_{nm,\varphi}.
\end{aligned} \tag{D.2}
$$

Using the above relations one can easily show

$$
\begin{aligned}
\boldsymbol{\nabla}_s \times \boldsymbol{v}_{nm} &= -\frac{\xi_n}{R_0} v^{(2)}_{nm} \boldsymbol{Y}_{nm}, \\
\boldsymbol{\nabla}_s \cdot \boldsymbol{v}_{nm} &= -\frac{\xi_n}{R_0} v^{(1)}_{nm} Y_{nm}, \\
\boldsymbol{\nabla}_s \boldsymbol{v}_{nm} : \boldsymbol{h} &= \frac{\xi_n}{R_0^2} v^{(1)}_{nm} Y_{nm}.
\end{aligned} \tag{D.3}
$$

The spherical harmonic orthogonality takes the form,

$$
\begin{aligned}
\oint \boldsymbol{Y}_{nm} \cdot \boldsymbol{Y}^*_{nm} \mathrm{d}\Omega &= \delta_{nn'}\delta_{mm'} \\
\oint \boldsymbol{\Psi}_{nm} \cdot \boldsymbol{\Psi}^*_{nm} \mathrm{d}\Omega &= n(n+1)\delta_{nn'}\delta_{mm'} \\
\oint \boldsymbol{\Phi}_{nm} \cdot \boldsymbol{\Phi}^*_{nm} \mathrm{d}\Omega &= n(n+1)\delta_{nn'}\delta_{mm'}
\end{aligned}
$$

The components of $\boldsymbol{\nabla}_s \boldsymbol{v} : \boldsymbol{h}$ in the tensorial form can be written by $v^i{}_{|j} h^i_j$, where $_{|j}$ represents the covariant derivative. Hence for the coordinate expression of the covariant derivative of a vector field $\boldsymbol{v} = v^i \boldsymbol{e}_i$ we have

$$
v^i{}_{|j} = v^i{}_{,j} + v^k \Gamma^i_{kj} \tag{D.4}
$$

where Γ^i_{kj} denotes the Christoffel symbols. Given the covariant derivatives in ap-

pendix D.3 we have

$$\boldsymbol{\nabla}_s \boldsymbol{v} : \boldsymbol{h} = \begin{pmatrix} v_{\varphi,\varphi}/R & v_{\varphi,\theta}/R - \cos\varphi v_\theta/R \\ v_{\theta,\varphi}/(R\sin\varphi) & v_{\theta,\theta}/(R\sin\varphi) + \cot\varphi v_\varphi/R \end{pmatrix} : \begin{pmatrix} -1/R & 0 \\ 0 & -1/R \end{pmatrix},$$

by employing Eqs. (D.2) in the above equation, we have

$$\boldsymbol{\nabla}_s \boldsymbol{v} : \boldsymbol{h} = -\sum \boldsymbol{\nabla}^2 Y_{nm} v^{(1)} = \sum \frac{n(n+1)}{R^2} v^{(1)} Y_{nm}. \tag{D.5}$$

Alternatively, one can obtain the above relation using the fact $h^i_j = -1/R\delta^i_j$, as

$$v^i{}_{|j} h^i_j = -\frac{1}{R} v^i{}_{|j} \delta^i_j = -\frac{1}{R} v^i{}_{|i} = -\frac{1}{R} \boldsymbol{\nabla}_s \cdot \boldsymbol{v} = \sum \frac{n(n+1)}{R^2} v^{(1)} Y_{nm} \tag{D.6}$$

D.3 Covariant derivative

In the spherical coordinates

$$\boldsymbol{e}_1 = \frac{\partial}{\partial\varphi} = R\,(\cos\varphi\cos\theta, \cos\varphi\sin\theta, -\sin\varphi) = R\hat{\boldsymbol{e}}_\varphi$$

$$\boldsymbol{e}_2 = \frac{\partial}{\partial\theta} = R\,(-\sin\varphi\sin\theta, \sin\varphi\cos\theta, 0) = R\sin\varphi\hat{\boldsymbol{e}}_\theta$$

Hence we conclude that $v^1 = v_\varphi/R$ and $v^1 = v_\theta/(R\sin\varphi)$.

$$\Gamma^1 = \begin{pmatrix} 0 & 0 \\ 0 & -\sin\varphi\cos\varphi \end{pmatrix}$$

$$\Gamma^2 = \begin{pmatrix} 0 & \cot\varphi \\ \cot\varphi & 0 \end{pmatrix}$$

which leads to

$$\begin{aligned}\boldsymbol{\nabla}_s \boldsymbol{v} &= \begin{pmatrix} v^1{}_{,1} & v^1{}_{,2} - \cos\varphi \sin\varphi v^2 \\ v^2{}_{,1} + \cot\varphi v^2 & v^2{}_{,2} + \cot\varphi v^1 \end{pmatrix} \\ &= \begin{pmatrix} v_{\varphi,\varphi}/R & v_{\varphi,\theta}/R - \cos\varphi v_\theta/R \\ v_{\theta,\varphi}/(R\sin\varphi) & v_{\theta,\theta}/(R\sin\varphi) + \cot\varphi v_\varphi/R \end{pmatrix}\end{aligned}$$

D.4 Elastic energy calculations: cylindrical coordinates

Using Eqs. (7.23), we compute the following expressions, which will be used in the total elastic energy,

$$\begin{aligned} 4H^2\ \mathrm{d}A &= \frac{1}{r_0}\left[1 - \frac{u}{r_0} + \frac{u^2}{r_0^2} - 2r_0\nabla_s^2 u + r_0^2\left(\nabla_s^2 u\right)^2 - \frac{1}{2}\left(u_{,z}\right)^2 + \frac{3}{2r_0^2}\left(u_{,\theta}\right)^2 + \frac{4uu_{,\theta\theta}}{r_0^2}\right]\ d\theta\ dz \\ 2H\ \mathrm{d}A &= \left(\frac{u_{,\theta}^2 + uu_{,\theta\theta} - r_0 u_{,\theta\theta}}{r_0^2} - r_0 u_{,zz} - uu_{,zz} + 1\right)\ d\theta\ dz \\ \mathrm{d}A &= \frac{1}{2r_0}\left(r_0^2 u_{,z}^2 + 2r_0^2 + 2ur_0 + u_{,\theta}^2\right)\ d\theta\ dz, \end{aligned}$$

where $\nabla_s^2 u = u_{,\theta\theta} + u_{,zz}/r_0^2$.

D.5 Calculations in vector cylindrical harmonic

Using the vecterial form of cylindrical harmonics for the surface velocity feild Eq. (7.26), it is straightforward to write some mathematical properties of vector cylindrical func-

tions by

$$\begin{aligned}
\boldsymbol{\nabla}_s \times \boldsymbol{v}_{nm} &= -\frac{\lambda_{nm}}{r_0} v_{nm}^{(2)} \boldsymbol{Y}_{nm}, \\
\boldsymbol{\nabla}_s \cdot \boldsymbol{v}_{nm} &= -\frac{\lambda_{nm}}{r_0} v_{nm}^{(1)} Y_{nm}, \\
\boldsymbol{\nabla}_s \boldsymbol{v}_{nm} : \boldsymbol{h} &= \frac{1}{r_0^2} \left(-m^2 v_{nm}^{(1)} Y_{nm} + m k_n r_0 v_{nm}^{(2)} Y_{nm} \right).
\end{aligned} \tag{D.7}$$

and their orthogonality by

$$\begin{aligned}
\int_\Gamma \boldsymbol{Y}^*{}_{nm}(\theta, z) \cdot \boldsymbol{Y}_{n'm'}(\theta, z) \, \mathrm{d}S &= 2\pi r_0 l \delta_{nn'} \delta_{mm'} \\
\int_\Gamma \boldsymbol{\Psi}^*{}_{nm}(\theta, z) \cdot \boldsymbol{\Psi}_{n'm'}(\theta, z) \, \mathrm{d}S &= 2\lambda_{nm} \pi r_0 l \delta_{nn'} \delta_{mm'} \\
\int_\Gamma \boldsymbol{\Phi}^*{}_{nm}(\theta, z) \cdot \boldsymbol{\Phi}_{n'm'}(\theta, z) \, \mathrm{d}S &= 2\lambda_{nm} \pi r_0 l \delta_{nn'} \delta_{mm'}.
\end{aligned}$$

D.6 Bulk fluid traction: tubular membranes

In Eq. (7.34), the nonzero components of $\mathbf{D}^{\pm}_{\mathrm{Re}}$, and $\mathbf{D}^{\pm}_{\mathrm{Im}}$ are given by

$$\begin{aligned}
(D^{\pm}_{\mathrm{Re}})_{11} &= 2 \left[\pm |k_n| r_0 P^{\pm}_{m+1} + (\lambda_{nm} - m) P^{\pm}_m \right] / r_0^2 \\
(D^{\pm}_{\mathrm{Re}})_{13} &= 2 \left[\mp |k_n| r_0 (1 + \lambda_{nm}) P^{\pm}_{m+1} + (m-1)(\lambda_{nm} - m) P^{\pm}_m \right] / r_0^2 \\
(D^{\pm}_{\mathrm{Re}})_{22} &= -\left[\pm 2 |k_n| r_0 P^{\pm}_{m+1} + \left(\lambda_{nm} + m^2 - 2m \right) P^{\pm}_m \right] / r_0^2 \\
(D^{\pm}_{\mathrm{Re}})_{32} &= -k_n m P^{\pm}_m / r_0 \\
(D^{\pm}_{\mathrm{Im}})_{12} &= 2m \left[\mp |k_n| r_0 P^{\pm}_{m+1} + (m-1) P^{\pm}_m \right] / r_0^2 \\
(D^{\pm}_{\mathrm{Im}})_{21} &= 2m \left[(m-1) P^{\pm}_m \mp |k_n| r_0 P^{\pm}_{m+1} \right] / r_0^2 \\
(D^{\pm}_{\mathrm{Im}})_{23} &= 2m \left[(\lambda_{nm} + 1 - 2m) P^{\pm}_m \pm 2 |k_n| r_0 P^{\pm}_{m+1} \right] / r_0^2 \\
(D^{\pm}_{\mathrm{Im}})_{31} &= 2k_n \left[m P^{\pm}_m \mp |k_n| r_0 P^{\pm}_{m+1} \right] / r_0 \\
(D^{\pm}_{\mathrm{Im}})_{33} &= 2\lambda_{nm} k_n P^{\pm}_m / r_0.
\end{aligned}$$